FINAL TECHNICAL REPORT

for

NASA GRANT NAGW-68

Studies of Planetary Upper Atmospheres Through Occultations

1 July 1980 through 30 June 1982

(NASA-CR-169189) STUDIES OF PLANETARY UPPER ATMOSPHERES THROUGH OCCULTATIONS Final Technical Report, 1 Jul. 1980- 30 Jun. 1982 (Massachusetts Inst. of Tech.) 292 p
HC A13/MF A01
CSCL 03B G3/91
N82-30209
Unclas
30107

Department of Earth and Planetary Sciences
Massachusetts Institute of Technology
Cambridge, Massachusetts 01239

James L. Elliot

James L. Elliot, Principal Investigator

FINAL TECHNICAL REPORT - NAGW-68

Studies of Planetary Upper Atmospheres Through Occultations

The goal of our research is to understand the structure, composition, dynamics and energy balance of planetary upper atmospheres, through proper interpretation of stellar occultation data. Stellar occultations are sensitive probes of the structure of planetry upper atmosphere, but it has not proven easy to extract definitive results from the observations. The spiky structure of the light curves has been variously interpreted as scintillation due to isotropic turbulence and as evidence for layered atmospheric structure. Correct identification of the physical mechanisms at work will provide essential information for understanding the dynamics and energy balance in the upper atmospheres of Uranus, Neptune, and Jupiter. Our main objects, under this grant, have been:

1. To investigate the wave-optical problem of modelling strong scintillation for arbitrary turbulent atmospheres.
2. To determine whether turbulence dominates the observations.
3. To relate these results to the physical processes in the observed upper atmospheres.

In the appendices, we have included manuscripts which have been submitted for publication, and which contain the detailed results of our investigations. Here, we shall summarize briefly the principal results of our studies.

We began our work with a rigorous investigation of the effects of turbulence on stellar occultation light curves, to learn how the observations could be used to learn the relative importance of turbulence and other dynamical processes in the regions probed. To study these questions, we developed a computer code capable of generating occultation light curves, using wave optics, by specifying the refractive properties of the model atmosphere. We confirmed the analytic weak scintillation theory of Hubbard et al. (1978), but found significant qualitative differences under conditions of strong scintillation. Our key finding was that Kolmogorov turbulence, whether isotropic or anisotropic, can account for neither the details of the spiky structure in the light curves nor the large-amplitude temperature variations found by numerical inversion of the data. This was the first definitive test of Young's (1976) contention that the observations are dominated by the effects of scintillations.

We applied our newly developed analysis techniques to the Uranus occultation of 15 August 1980. Observations separated by many Fresnel scales along the limb of the planet show a high degree of correlation, suggesting that the atmosphere is strongly layered. We confirmed that the derived variations in the thermal profile are not artifacts of Kolmogorov turbulence.

Next, we investigated the energy balance in the Uranus upper atmosphere, and considered mechanisms that might maintain the large observed temperature variations against a host of disruptive processes. We found evidence that the mean temperature of the upper amtosphere has changed significantly over a period of four years, and investigated the associated energetics. We concluded that molecular and eddy diffusion, and atmospheric dynamics, are as important as radiation to the upper atmospheric heat balance.

Finally, we investigated the properties of light curves produced by a wide range of realistic atmospheric models, including fields of inertia-gravity waves in the presence of turbulence, and determined the effects of severe ray crossing on the numerical inversion method of obtaining temperature profiles. We concluded that quasi-global features of atmospheric structure are accurately determined by numerical inversion; horizontally inhomogeneous structures (including turbulence) with length scale $L \ll (2\pi RH)^{1/2}$, where R = planetary radius and H = scale height, are filtered out and have little effect on the derived profiles.

We are now in a position to extend our work to detailed modelling of light curves under the specific conditions appropriate to individual occultation events, with the goal of comparing the upper atmospheric structure of the outer planets.

REFERENCES

Hubbard, W.B., Jokipii, J.R. and Wilking, B.A. (1978). Icarus 34, 374-395.

Young, A.T. (1976). Icarus 27, 335-358.

APPENDIX A

Publications Under NASA Grant NAGW-68

1. *The Upper Atmosphere of Uranus: A Critical Test of Isotropic Turbulence Models*, by French, R.G., J.L. Elliot, B. Sicardy, P. Nicholson, and K. Matthews, Icarus (1982), in press. (Appendix B).

2. *The Thermal Structure and Energy Balance of the Uranian Upper Atmosphere*, by French, R.G., J.L. Elliot, E.W. Dunham, D. Allen, J.H. Elias, J.A. Frogel, and W. Liller. Icarus (1982), submitted and refereed; currently under revision for final submission. (Appendix C).

3. *Strong Turbulence and Atmospheric Waves in Stellar Occultations*, by French, R.G. and R.V.E. Lovelace, Icarus (1982), submitted. (Appendix D).

4. *Turbulence Models and the Atmosphere of Uranus*, by French, R.G. and J.L. Elliot, Bull. Am. Astron. Soc. *12*, 704. Abstract. (Appendix E).

5. *Structure of the Upper Atmosphere of Uranus*, by French, R.G., April, 1981 IAU/RAS Colloquium on Uranus and the Outer Planets. Abstract. (Appendix F).

APPENDIX B

THE UPPER ATMOSPHERE OF URANUS:
A CRITICAL TEST OF ISOTROPIC TURBULENCE MODELS

ORIGINAL PAGE IS
OF POOR QUALITY

ICARUS 51, 000—000 (1982)

The Upper Atmosphere of Uranus: A Critical Test of Isotropic Turbulence Models

RICHARD G. FRENCH

Department of Earth and Planetary Sciences, Massachusetts Institute of Technology, Cambridge, Massachusetts 02139, and Department of Astronomy, Wellesley College, Wellesley, Massachusetts 02181

JAMES L. ELLIOT

Department of Earth and Planetary Sciences and Department of Physics, Massachusetts Institute of Technology, Cambridge, Massachusetts 02139

BRUNO SICARDY

Observatoire de Paris, Meudon, France

PHILIP NICHOLSON

Jet Propulsion Laboratory, California Institute of Technology, Pasadena, California 91109

AND

KEITH MATTHEWS

Division of Physics, Mathematics and Astronomy, California Institute of Technology, Pasadena, California 91125

Received October 5, 1981; revised May 3, 1982

Observations of the 15 August 1980 Uranus occultation of KM 12, obtained from Cerro Tololo InterAmerican Observatory, European Southern Observatory, and Cerro Las Campanas Observatory, are used to compare the atmospheric structure at points separated by ~140 km along the planetary limb. The results reveal striking, but by no means perfect, correlation of the light curves, ruling out isotropic turbulence as the cause of the light curve spikes. The atmosphere is strongly layered, and any acceptable turbulence model must accommodate the axial ratios of $\gtrsim 60$ which are observed. The mean temperature of the atmosphere is 150 ± 15°K for the region near number density 10^{14} cm^{-3}. Derived temperature variations of vertical scale ~130 km and amplitude ±5°K are in agreement for all stations, and correlated spikes correspond to low-amplitude temperature variations with a vertical scale of several kilometers.

I. INTRODUCTION

Observations of planetary upper atmospheres are of interest because they provide information about the radiative and dynamical processes at work in these rarefied regions, and permit tests of models of thermal structure, atmospheric wave propagation, and turbulence. With the advent of high-speed photometry, stellar occultation observations have been made in recent years of the atmospheres of Jupiter, Neptune, Mars, and Uranus [see Elliot (1979) for an extensive review and references]. The occultation light curves almost invariably contain sharp intensity variations, or spikes, indicating that the atmospheres are not isothermal, but there has been no agreement on the nature of the atmospheric refractivity variations responsible for the spikes.

Two approaches to the problem have

0019-1035/82/050000-00$02.00/0

001

been adopted. The first has been to assume that the atmosphere can be approximately characterized by homogeneous layers of large horizontal extent, that geometric optics is applicable, and that ray crossing is not severe. Under these circumstances, a unique mapping exists between the observed light curve and the atmospheric temperature profile. The alternative strategy has been to regard spikes as manifestations of turbulence-induced scintillation. According to this view, in its most extreme form, the assumption of spherical symmetry is not even approximately satisfied, and the detailed temperature structure deduced from numerical inversion of a light curve bears little relation to the true atmospheric basic state.

In the past, there has been no definitive test of these opposing views. Careful studies of the observations of the Jupiter occultation of β Sco reached fundamentally different conclusions about the importance of turbulence and the structure of the Jovian atmosphere (Elliot and Veverka, 1976; Hunten and Veverka, 1976; and Jokipii and Hubbard, 1977). Combes *et al.* (1975) pointed out that the divergences among the inferred temperature profiles are the results of different analysis methods, but there remains a clear difference of opinion about the importance of turbulent scintillation in stellar occultation data. From multiple observations of the Mars occultation of ε Gem, French and Elliot (1979) concluded that the numerical inversion method was valid for Mars, and that the temperature profiles provided evidence for semiglobal waves, similar to those observed by Viking 1 and Viking 2 (Seiff and Kirk, 1977) and predicted by Zurek (1976). However, the Texas–Arizona Occultation Group (1977) and Hubbard (1979) found the observations equally consistent with isotropic turbulence theory. As a final example, large-amplitude fluctuations were observed in the Mariner 5 Venus occultation. These data provide a demonstration of the small effect on temperature profiles of these fluctuations, based on the separate frequency and amplitude inversions of Mariner 5 data which yielded nearly identical profiles (Fjeldbo *et al.*, 1971).

It is important to resolve the dispute. If the occultation temperature profiles are reliable, they provide information about the dynamical state of the upper atmospheres of Mars, Neptune, Jupiter, and Uranus. On the other hand, if the effects of turbulence are dominant, it may be possible to compare the turbulence fields of these planets. "A sensitive test which can in principle determine which hypothesis is correct would be to observe the same occultation from two points on Earth for which the ray paths are separated by ~100 km along the limb. A significant correlation would favor the layering hypothesis, whereas a lack of correlation would favor the turbulence model" (Jokipii and Hubbard, 1977). In this paper we report the results of such a test. On 15 August 1980, Uranus occulted star No. 12 on the list of Klemola and Marsden (1977). High-quality photometric observations at 2.2 μm wavelength were made from several stations, and the results indicate striking, but by no means perfect, correlation of structure in the Uranus atmosphere for distances of ~140 km along the planetary limb. We conclude that the atmosphere is strongly layered, and that the observed spikes are not manifestations of isotropic turbulence, or of any reasonable form of anisotropic turbulence.

II. OBSERVATIONS

In order to test turbulence models, we will compare the occultation light curves obtained from Cerro Tololo InterAmerican Observatory (CTIO), European Southern Observatory (ESO), and Cerro Las Campanas Observatory (CLCO). Several characteristics of the observations are given in Table I. Here we restrict our attention to information provided by a direct comparison of the data. Further analysis and interpretation, and detailed information about each observation, can be found in the re-

TABLE I

OCCULTATION OBSERVATIONS

Observatory	Telescope aperture (m)	Filter	References
CTIO	4.0	K	French *et al.* (1982)
ESO	3.6	K	Sicardy *et al.* (1982)
CLCO	[illegible].5	K	Nicholson *et al.* (1982a)

ports of each group cited in Table I. All of the observations were made in the K band ($\lambda_0 = 2.2$ μm, $\Delta\lambda = 0.4$ μm), where the signal from Uranus is strongly depressed. The three stations sampled regions separated by up to ~140 km along the limb of Uranus. Figure 1 shows the geometry of the event. Immersion occurred at a latitude on Uranus of approximately −26°S and probed the dark limb of the planet; emersion occurred near latitude +18°N and probed the illuminated limb. All stations obtained high-quality photometric data of the immersion event, and 300 sec of the corresponding light curves are shown in Fig. 2. A strong correlation of several of the large intensity fluctuations is immediately apparent, as will be shown quantitatively in the next section.

Each group experienced difficulties during the emersion phase of the occultation: at CTIO, clouds caused variations in signal level; at ESO, problems with guiding caused the star to drift in and out of the aperture; and at CLCO, recording was not begun until mid-emersion. In spite of these problems, convincing correlation of several large spikes in the emersion light curves is also evident (Fig. 3).

For this analysis, the CLCO data were digitized from a copy of the stripchart record of the observations. Nicholson *et al.* (1982a) independently digitized the original record at a higher time resolution for their analysis. Slight differences in the digitizations are responsible for some of the differences between the CLCO results reported here and those given by Nicholson *et al.* The inherent difficulty in the digitization

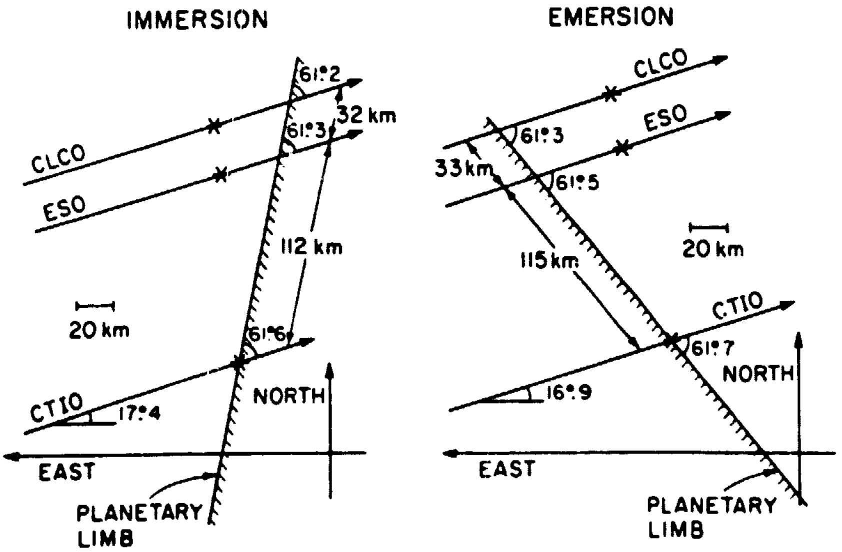

FIG. 1. Occultation geometry. The immersion and emersion tracks of the star relative to the planetary limb are shown for each station. Immersion occurred near latitude −26° and emersion occurred near latitude 18°. The symbols on each track show the apparent stellar location as seen simultaneously from each station at a time prior to immersion and at a time after emersion.

ORIGINAL PAGE IS
OF POOR QUALITY

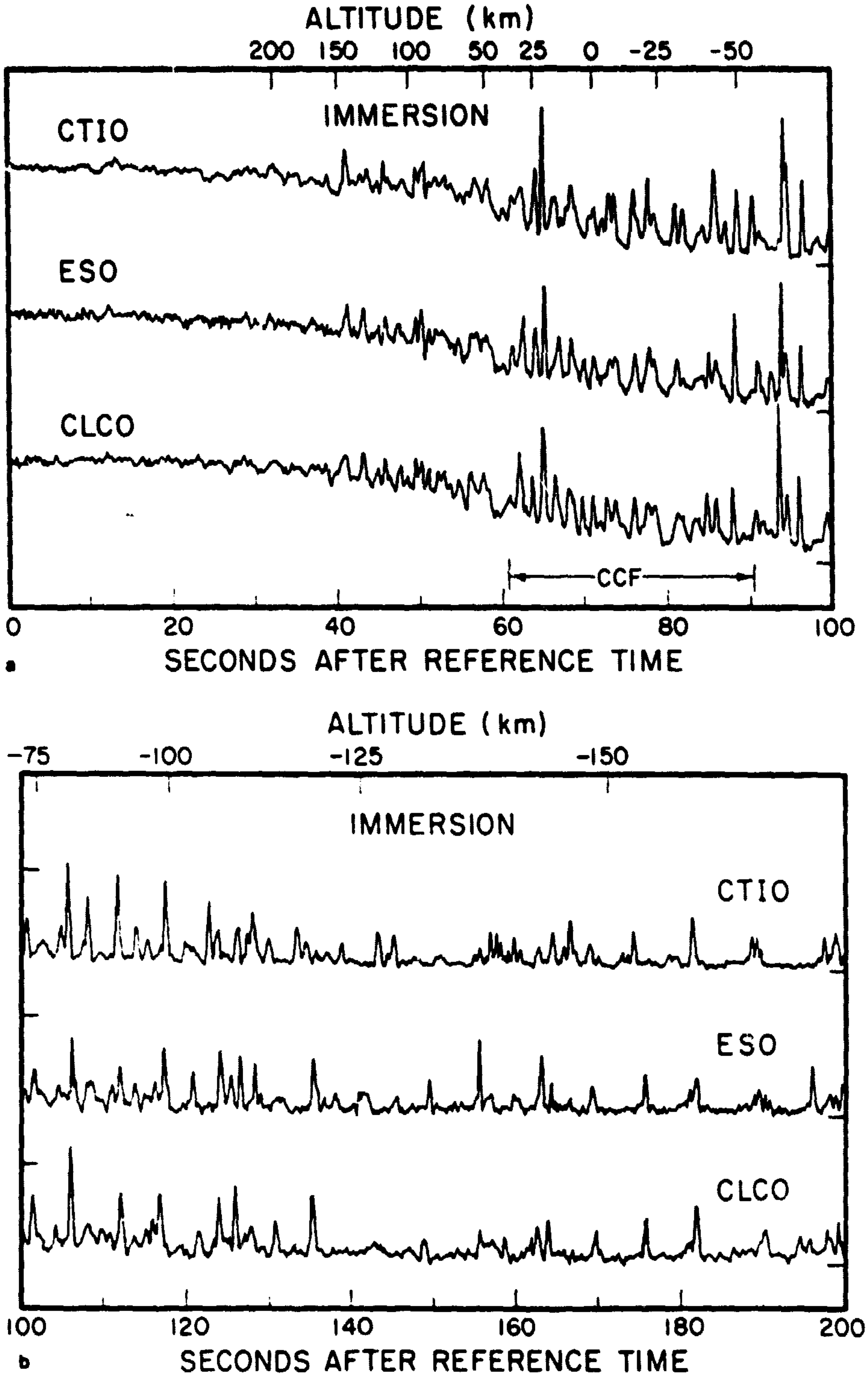

FIG. 2. Immersion occultation light curves. Time is in seconds after the following reference times on 15 Aug 1980 (UT): CTIO, $22^h\ 36^m\ 58^s.01$; ESO, $22^h\ 37^m\ 02^s.40$; CLCO, $22^h\ 37^m\ 03^s.65$. These times were chosen so that the light curves would be in approximate alignment at the astrometric half-light time. The approximate altitude scale in the atmosphere relative to the half-light level is shown. The cross-correlation results shown in Fig. 4 were computed over the interval labeled CCF. Unit stellar intensity levels are shown on the left and zero intensity levels on the right.

004

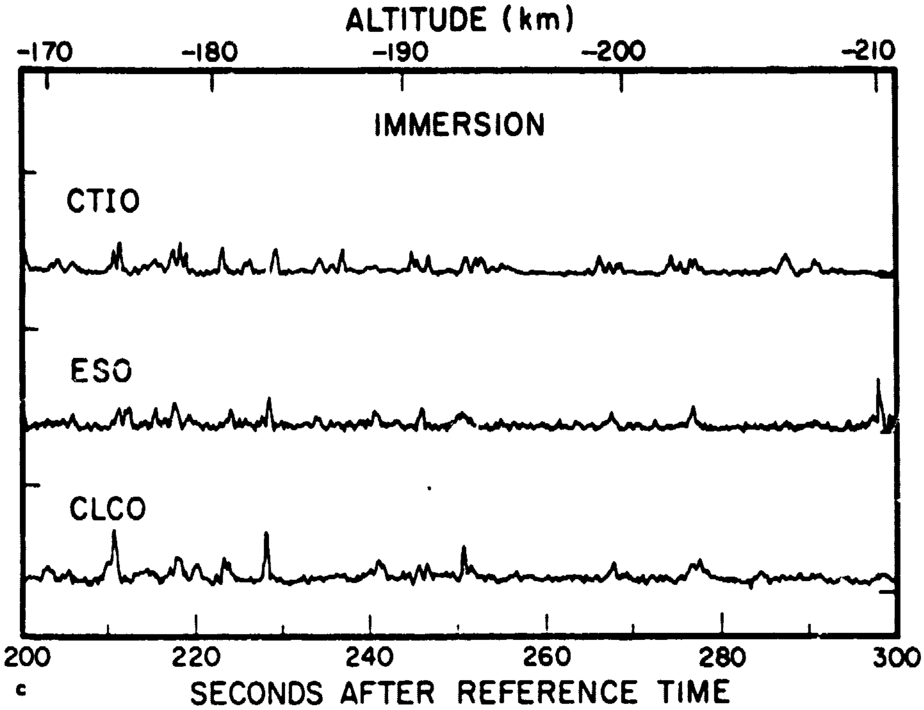

FIG. 2—*Continued.*

procedure is in maintaining a constant zero level for each section of the chart record, which in our analysis is uncertain by about 1% of the stellar intensity. Direct digital recording of the data onto magnetic tape was not possible at CLCO, but would have eliminated this source of error.

III. ANALYSIS AND DISCUSSION

The extent of similarity in atmospheric structure along the limb can be determined by examining correlations in the raw data and by comparing temperature profiles obtained by numerical inversion. The most direct test is cross-correlation of the light curves themselves. We begin our analysis by computing the intrinsic rms spike amplitude, a quantity which can be directly related to turbulence theory, and estimating the effects of noise. We then discuss occultation timing and proper alignment of the light curves for the subsequent cross-correlation analysis, and we compare the correlation results with predictions of turbulence theory. On the basis of this evidence of extensive layering in the Uranus atmosphere, we then adopt the assumptions of the numerical inversion method and compare the temperature structure derived from the three separate immersion observations. Finally, we discuss the relation of spikes to the derived temperature profiles.

A. Comparison of Light Curves

Amplitude of light curve variations. A quantitative measure of the strength of the nonisothermal character of a light curve is provided by the mean-square amplitude of the spikes. In the context of turbulence theory, this is known as the scintillation power, and can be directly related to the amplitude of the putative turbulent refractivity fluctuations. To determine the intrinsic strength of the light curve variations, it is necessary to determine the contribution of noise to the observed spike amplitude.

To estimate the importance of noise, we computed the quantity ϵ, the rms noise in

005

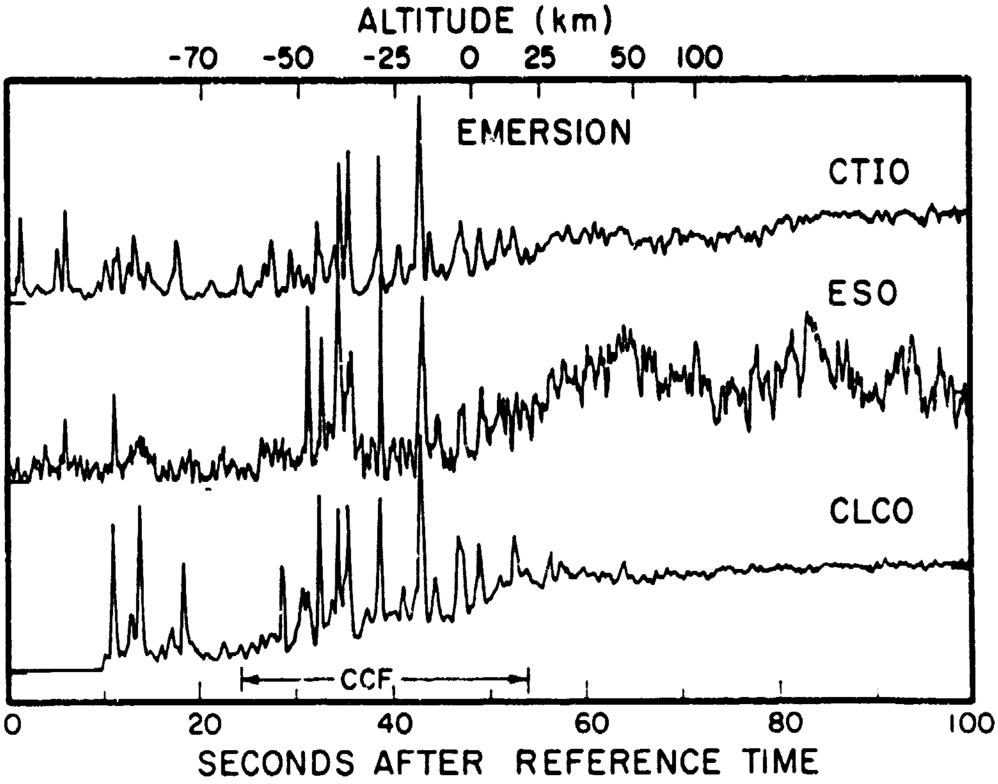

FIG. 3. Emersion occultation light curves. Time is in seconds after the following reference times on 16 August 1980 (UT): CTIO, $0^{\rm h}\,15^{\rm m}\,38^{\rm s}.21$; ESO, $0^{\rm h}\,15^{\rm m}\,31^{\rm s}.40$; CLCO, $0^{\rm h}\,15^{\rm m}\,29^{\rm s}.45$. These times were chosen so that the light curves would be in approximate alignment at the astrometric half-light time. The approximate altitude scale in the atmosphere relative to the half-light level is shown. The cross-correlation results shown in Fig. 4 were computed over the interval labeled CCF. Zero stellar intensity levels are shown on the left and unit intensity levels on the right.

the light curve for a 1-sec integration, expressed as a fraction of $n*$, the counts per second for the unocculted star. If $n(t_j)$ is the mean counting rate in counts per second for the jth integration bin of duration Δt, N is the total number of integration bins used in the calculation, and $\bar{n}$ is the mean counting rate in counts per second for all N integration bins, then

$$\epsilon = \frac{(\Delta t)^{1/2}}{n*}\left\{\frac{1}{N-1}\sum_{j=1}^{N}[n(t_j)-\bar{n}]^2\right\}^{1/2}. \quad (1)$$

Using a total of 50 sec of data (at time resolution $\Delta t = 0^{\rm s}.2$) prior to immersion and after emersion, when the only variations in the light curve would be due to noise, and computing the average ϵ for a running mean of 4 sec duration, we obtained the results given in Table II. The principal uncertainty in the ESO emersion results is in determining $n*$, because the star was drifting in and out of the aperture. (This was true to some extent during immersion as well, since offset guiding was not possible until after immersion had occurred.) The quantity $(v_\perp/H)^{1/2}\epsilon$ is a dimensionless measure of the rms noise of an occultation (French *et al.*, 1978), where $v_\perp$ is the velocity of the event perpendicular to the limb of the planet and H is the mean scale height. We computed $v_\perp$ from event astrometry and assumed that $H = 70$ km. The noise is lowest for the CTIO observations, which used the largest-aperture telescope.

ORIGINAL PAGE IS
OF POOR QUALITY

TABLE II

LIGHT CURVE FLUCTUATIONS

Station	Event	$v_\perp$[a] (km sec^{-1})	ϵ (sec$^{1/2}$)	$(v_\perp/H)^{1/2}\epsilon$[b]	$[\Delta\phi_a^2]^{1/2}$
CTIO	Immersion	6.811	0.007	0.002	0.18
ESO	Immersion	6.792	0.013	0.004	0.15
CLCO	Immersion	6.788	0.013	0.004	0.15
CTIO	Emersion	6.888	0.008	0.003	0.28
ESO[c]	Emersion	6.874	(0.04)	(0.013)	(0.45)
CLCO	Emersion	6.858	0.011	0.003	0.32

[a] Perpendicular velocities computed for an oblate planet with an ellipticity of 0.024 (Elliot *et al.*, 1981).

[b] A scale height of 70 km was assumed, corresponding to a temperature of 151°K.

[c] Results for the ESO emersion data are affected by guiding problems during the gradual reappearance of the occulted star.

Having determined the contribution of noise to the light curve fluctuations, we computed $[\Delta\phi_a^2]^{1/2}$, the rms amplitude of light curve fluctuations due to the atmosphere of Uranus, from

$$[\Delta\phi_a^2]^{1/2} = \frac{1}{N}\sum_{i=1}^{N}\left\{\Delta\phi_i^2 - \epsilon^2/\Delta t\right\}^{1/2}. \quad (2)$$

where $\Delta\phi_i$ is the *i*th observed residual of the light curve from a running mean of 4 sec of data, normalized by the unocculted stellar intensity. For the regions of Figs. 2 and 3 marked "CCF," we obtained the results in Table II. In all cases, the observed fluctuations are far larger than the noise level. Photon noise is not a significant source of error compared to known systematic effects, such as guiding errors and variable atmospheric transparency. The combined effects of all noise sources are substantially smaller than was the case for the β Sco occultation by Jupiter (Jokipii and Hubbard, 1977) or the ε Gem occultation by Mars (Texas–Arizona Occultation Group, 1977; French and Elliot, 1979). (For example, the terrestrial scintillation power was approximately five times the Martian scintillation power in the McDonald Observatory ε Gem data analyzed by the Texas–Arizona Occultation Group.) The current observations are the least noisy of any which have been used to study atmospheric correlations along planetary limbs. There is good agreement among stations for the intrinsic spike amplitude during immersion ($[\Delta\phi_a^2]^{1/2} \approx 0.16$), and although the emersion results are less certain, the rms spike amplitude is about twice that during immersion.

Occultation timing and light curve alignment. In order to compare the light curves in detail, it was necessary to determine reference times at which the occulted star was at a common sky–plane distance from the center of Uranus for all stations, both for immersion and for emersion. It has become conventional to use the "half-light" time as a reference: this is the time at which the best-fitting model isothermal light curve falls to half-intensity. We computed $t_{1/2}$, the isothermal fit half-light time, for all the immersion data and for the CTIO emersion light curve. The results of these fits are given in Table III. Because of variable signal level and insufficient data for the three emersion light curves (see Fig. 3), we have not included a comparison of all of the emersion half-light times. Nicholson *et al.* (1982a) discuss the emersion results in more detail and relate them to the determination of the oblateness of Uranus.

An independent set of reference times was computed from the event astrometry. The sky–plane coordinates of the center of

001

TABLE III

OCCULTATION TIMING RESULTS

Station	Event	Isothermal fit $t_{1/2}$ (UT)		Astrometric[a] $t_{1/2}$ (UT)	$\Delta t_{1/2}$[b] (sec)
CTIO	I	15 Aug 1980	$22^h\ 38^m\ 09^s.07$	$(22^h\ 38^m\ 09^s.07)$	(0.00)
ESO	I	15 Aug 1980	22 38 09.02	22 38 13.49	−4.47
CLCO	I	15 Aug 1980	22 38 13.34[c]	22 38 14.79	−1.45
CTIO	E	16 Aug 1980	$0^h\ 16^m\ 26^s.42$	$(0^h\ 16^m\ 26^s.42)$	(0.00)
ESO	E	16 Aug 1980	—	0 16 19.60	—
CLCO	E	16 Aug 1980	[d]	0 16 17.65	—

[a] The astrometric half-light time is the time at which the occulted star was at the sky–plane distance from the center of Uranus corresponding to the CTIO isothermal fit half-light time. The effects of refraction were assumed to be the same for all three stations.

[b] The difference between the isothermal fit and astrometric half-light times.

[c] Nicholson *et al.* (1982a) obtained an isothermal fit half-light time of $22^h\ 38^m\ 14^s.8$ from their analysis of the CLCO immersion data, with a corresponding $\Delta t_{1/2}$ of 0.0 sec.

[d] Nicholson *et al.* (1982a) obtained a half-light time of $0^h\ 16^m\ 07^s.5$, based on an isothermal fit of the CLCO emersion light curve in Fig. 3. The discrepancy between the CTIO and CLCO emersion isothermal half-light times is probably caused by the combined effects of incomplete data for CLCO and variable transmission for CTIO.

the planet were determined to high accuracy from a simultaneous solution for the orbits of the nine known Uranian rings, using all of the available ring occultation data (Elliot *et al.*, 1981). We assumed that the planetary center corresponds to the center of mass of the ring–planet system. With this information and the known relative sky–plane velocity of the planet and star, we determined an "astrometric half-light time." This is the time at which the occulted star was at the sky–plane distance from the center of Uranus corresponding to the CTIO isothermal fit half-light time.

If the atmosphere were horizontally homogeneous and the light curves were noise-free, then the astrometric and isothermal fit half-light times would be identical. In fact, there are differences of up to several seconds, as seen in Table III. To estimate the effects of the known noise level on the isothermal half-light times, we superimposed preimmersion and postemersion data on an isothermal light curve and compared the best-fit half-light times to the noise-free values. We found that the known noise introduced an uncertainty of about $\pm 0^s.8$, larger than expected on the basis of photon noise alone (French *et al.*, 1978), but less than the largest $\Delta t_{1/2}$ in Table III. Nicholson *et al.* (1982a) obtained a CLCO immersion half-light time corresponding to $\Delta t_{1/2} = 0.0$ sec from their analysis of the CLCO data. The large discrepancy between the astrometric and isothermal fit half-light times for ESO is probably a result of low-frequency modulation of the light curve due to guiding errors during immersion, since offset guiding was not employed. Comparison of the light curves in Fig. 2 reveals a loss of signal in the ESO data relative to the other two observations over the interval of 100 to 130 sec, consistent with this interpretation. Henceforth, unless otherwise noted, we shall use the term "half-light time" to refer to the *astrometric* half-light time. We emphasize that these times are computed *relative* to the CTIO isothermal fit times.

In the past, isothermal fit half-light times have been used for astrometric determination of planetary oblateness for Uranus (Elliot *et al.*, 1980, 1981), Mars (French and Taylor, 1981), Neptune (Kovalevsky and Link, 1969), and Jupiter (Hubbard and Van

008

Flandern, 1972; Lechacheux *et al.*, 1973; Taylor, 1974). This is a legitimate procedure as long as it is recognized that the half-light altitude may not correspond to an isobaric or a constant density surface. However, the present results suggest that, on occasion, isothermal half-light times may be more uncertain than is suggested by the level of noise in the data. The mutual consistency of half-light times can be checked only with multiple observations of the same event. The ESO immersion isothermal fit and astrometric half-light times (Table III) differ by more than 4 sec, corresponding to an error in the deduced radius of $v_\perp \Delta t_{1/2} \sim 30$ km. Because of the orientation of the Uranus pole, occultation observations are restricted to the equatorial regions. The total difference in planetary radius at the equator and at 30° latitude is only ~150 km, so that this newly identified potential source of error should be considered when estimating the uncertainties of the oblateness determination and the implied rotation period.

Cross-correlation of light curve residuals. One measure of the similarity of atmospheric structure along the limb is the extent of agreement in the detailed features of the light curves among the three observations. Although the relationship between light curve spikes and atmospheric structure is indirect, it is useful to quantify in a direct manner the degree of similarity of the observations themselves before proceeding to numerical inversion of the light curves.

We computed the cross-correlation function (CCF) of the light curve residuals for all of the immersion and emersion observations. Our method is similar to that used by French and Elliot (1979) in a comparison of occultation observations of Mars. Residual curves at $0\overset{s}{.}2$ resolution were formed by subtracting the running mean of 4 sec of data from each point; the results were essentially unchanged when 8-sec running means were employed. The data interval used was similar for both immersion and emersion: from 10 sec above to 20 sec below the half-light level of each curve (see Figs. 2 and 3). The corresponding range in normalized stellar flux is between 0.63 and 0.31. The residual curves were aligned at the astrometric half-light times, and the CCF was computed for lags between ±5 sec in $0\overset{s}{.}2$ increments. Each curve was scaled in time by the appropriate $v_\perp$ prior to performing the cross-correlation.

The results are shown in Fig. 4. For both immersion and emersion, there is a convincing peak near zero lag, and the shape of the CCF is similar for both sets of three curves. The maximum observed correlations, the corresponding lags, and the separation along the limb between each pair of stations are given in Table IV. Also included are the predicted time offsets between the astrometric half-light times. For a uniformly layered atmosphere on a spherical planet, the maximum correlation would occur at zero lag. The observed lags

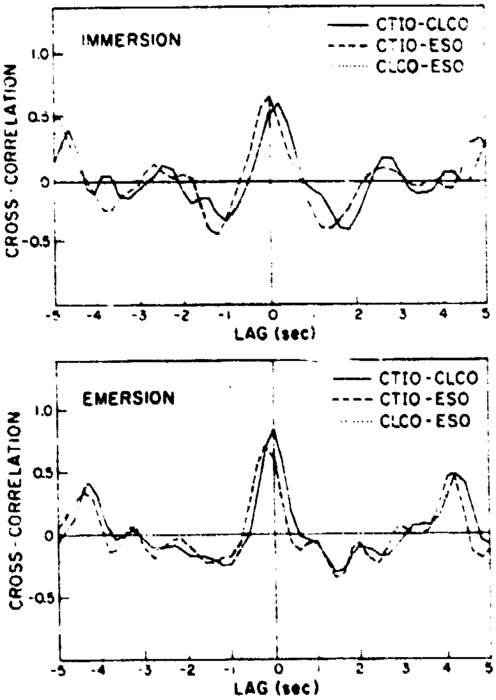

FIG. 4. Immersion and emersion cross-correlation of light curve residuals. See text for details of the computation.

TABLE IV

CROSS-CORRELATION RESULTS

Station	Event	d^a	$c_{max}{}^b$	Astrometric Δt^c (sec)	Lag^d (sec)
CLCO −					
ESO	I	32	0.77	1.30	−0.3
CTIO − ESO	I	112	0.67	−4.42	0.0
CTIO − CLCO	I	144	0.63	−5.72	+0.1
CLCO −					
ESO	E	33	(0.84)	−1.95	−0.1
CTIO − ESO	E	115	(0.73)	6.82	−0.1
CTIO − CLCO	E	147	0.83	8.77	0.0

[a] *d* is the distance along the Uranus limb separating the regions sampled by the two stations.

[b] c_{max} is the observed maximum correlation. Results involving the ESO emersion data are affected by guiding problems during the gradual reappearance of the occulted star.

[c] Astrometric Δt is the predicted time offset between the astrometric half-light times of the two stations, in the sense first station − second station.

[d] The lag corresponding to c_{max} is: observed time offset of the second station relative to the first station for maximum correlation − astrometric Δt.

are pleasingly small. As a confirmation of the smallness of any systematic timing errors among the three stations, Nicholson *et al.* (1982b) obtained mean discrepancies (observed − astrometric) in the ring occultation times of 0.2 sec (ESO − CLCO) and ≤0.1 sec (CTIO − CLCO). The full width at half-maximum (FWHM) of the CCF is $\sim 0^{s}.8$, or about 5.4 km along the light curve. The characteristic FWHM of the CTIO immersion autocorrelation function (ACF) is $\sim 0^{s}.6$, corresponding to 4.1 km. On the basis of models of ring profiles, an upper limit to the subtent of the occulted star is estimated to be 0.18 milliarcsec, or 2.4 km at the distance of Uranus. The Fresnel scale, $(\lambda D)^{1/2}$, is 2.45 km, where λ is the observed wavelength and D is the distance to the planet. The observed FWHM of both the ACF and the CCFs exceed both of these length scales, but it is still possible that the observed light curve is significantly filtered by convolution with the stellar image and by the diffraction resolution limit.

The maximum correlation as a function of station separation is shown in Fig. 5. For immersion, the correlation remains high for separations of over 100 km, decreasing slowly with distance. For emersion, the correlation is even higher, due perhaps to the larger intrinsic spike amplitude (Table II), but the trend with increasing distance is unclear because of the difficulty at ESO of acquiring the star in the aperture during emersion.

The rotation of Uranus during the occultation and the singular viewing geometry during the event cause the sampled suboccultation points in the Uranian atmosphere to be separated by somewhat more than the distance along the limb projected into the sky plane. For a rotation period of 16 hr, the immersion CTIO − CLCO separation at

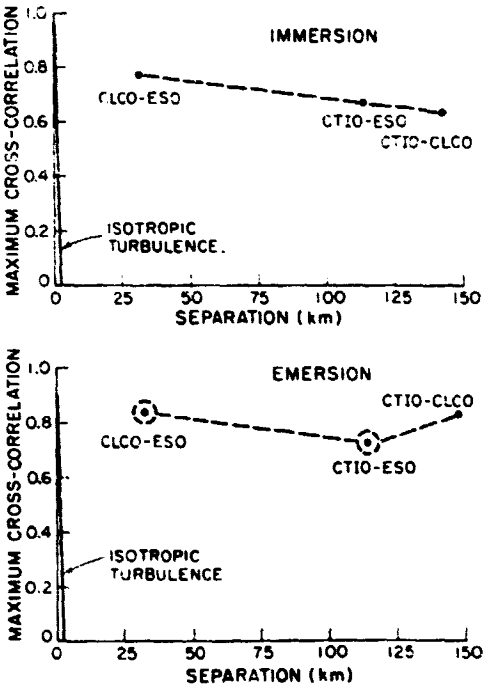

FIG. 5. Cross-correlation of light curve residuals as a function of separation distance along the limb of the planet. For immersion, the correlation remains high for separations of over 100 km, decreasing slowly with distance. For emersion, the correlation is very high, but the trend with increasing station separation is unclear because of guiding problems during ESO emersion. The correlation extends much further than predicted on the basis of isotropic turbulence theory (Jokipii and Hubbard, 1977) and provides evidence that the atmosphere is strongly stratified.

Uranus is increased by 16 km and the emersion separation by 25 km over the values given in Table IV and shown in Fig. 5.

As a test of the degree of correlation throughout the occultation, we determined the peak cross-correlation of immersion light curve residuals as a function of position along the light curve. The results are displayed in Fig. 6, where we plotted the peak cross-correlation as a function of the mid-point, relative to the half-light time, of the 30-sec interval of data used to compute the CCF. The mid-time was stepped in 5-sec increments, and the maximum correlation within 1 sec of the zero lag position was recorded. For the interval shown, the peak correlation is rather uniform over a broad section of the immersion light curves. (Similar calculations were not possible for the emersion data because of the problems previously cited.) The results shown in Figs. 4 and 5 correspond to a mid-time of +5 sec.

Although the correlation is strong during the interval used in the computation, the detailed agreement among the light curves deteriorates deeper into the occultation. The immersion data in Fig. 2 have common features well after 200 sec, but it is unclear how many of them are chance alignments. Deep in the occultation, a slight difference in depth in the atmosphere, Δz, can cause a wide separation in time, Δt, between features on the light curve. At low stellar flux ($\phi \ll 1$),

$$\Delta t \simeq \Delta z / v_\perp \phi. \tag{3}$$

For example, consider a thin spike-producing layer that differs in altitude by only 2 km over the 150-km horizontal distance separating the regions sampled by two stations. At an altitude in the atmosphere of 200 km below the half-light level, corresponding to $\phi \simeq 0.05$, the time separation along the light curves is $\Delta t \simeq 5$ sec. Since the typical spike separation on a single light curve is ~10 sec in this region of the light curve (Fig. 2c), such slight altitude varia-

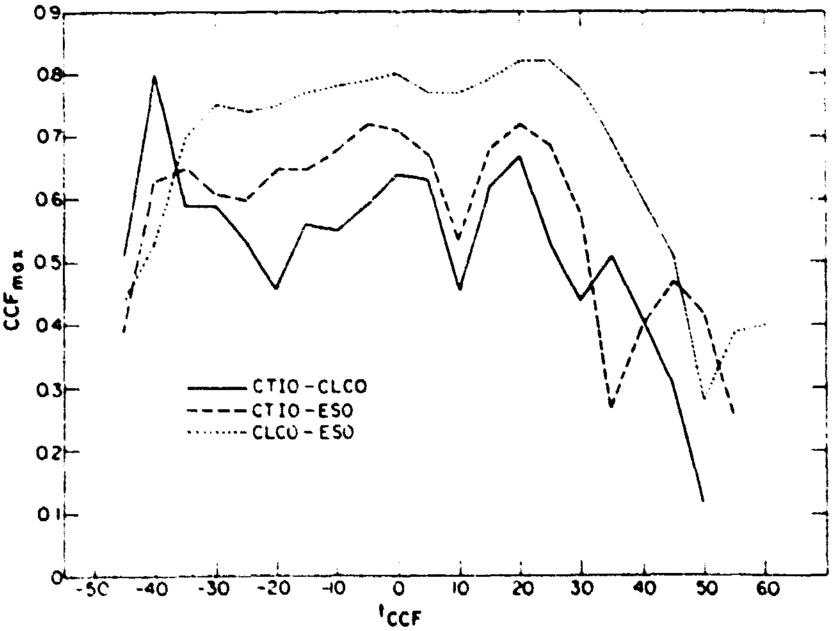

FIG. 6. Peak cross-correlation of immersion light curve residuals as a function of position along the light curve. The abscissa indicates the time, relative to the half-light time, of the mid-point of the 30-sec interval of data used to compute the cross-correlation.

tions would make it impossible to correlate the spikes in different light curves unambiguously.

Figures 2 and 3 have been labeled with an altitude scale, relative to the half-light level, computed assuming an isothermal atmosphere of scale height 70 km and a perpendicular velocity of 6.8 km $\sec^{-1}$. (The altitude scale is only approximate, since the atmosphere is not isothermal.) Wave-optical calculations of strongly focused spikes (French and Lovelace, 1982) reveal that an individual spike can be transformed into a cluster of spikes as the overfocused condition is reached. We tentatively identify the CTIO spikes at 265 and 275 sec in Fig. 2c as candidates for this diffraction phenomenon.

A key diagnostic of the importance of turbulence is the degree of correlation of spikes in the light curve as a function of separation distance. For weak isotropic turbulence, the CCF FWHM would be roughly the larger of the Fresnel scale or the projected stellar diameter, and there would be no significant correlation for stations separated by distances much larger than the FWHM. For the 15 August 1980 event, the isotropic turbulence theory (Jokipii and Hubbard, 1977) would predict the CCF shown in Fig. 5. The observations could hardly be in greater disagreement. The correlation is still strong, even for separation distances of 60 vacuum Fresnel lengths. Hubbard *et al.* (1978) have developed a wave-optical theory for weak anisotropic turbulence, which can be formally extended to perfectly stratified layers parallel to the limb. However, the present results imply an aspect ratio of well over 60 for the turbulent "pancakes." Under these circumstances, the scaling arguments from which the Kolmogorov turbulence spectrum is derived are questionable. As Jokipii and Hubbard (1977) point out: "It is possible to construct extremely anisotropic turbulence models for which the correlation distance parallel to the limb is larger than a few kilometers, but these are effectively layering models." Model realizations of anisotropic Kolmogorov turbulence, valid even for strong scintillations, show very little resemblance to the observations (French and Lovelace, 1982), and *we conclude that the effects of Kolmogorov turbulence do not dominate the structure of the Uranus upper atmosphere*.

The situation may well be different on other planets. Woo *et al.* (1980) found evidence for anisotropic Kolmogorov turbulence in the Venus atmosphere on the basis of radio occultation measurements, for example. However, based on the Pioneer Venus probe measurements, Seiff *et al.* (1980) found that this altitude region has small-scale thermal structure (see their Fig. 21). Thus it remains possible that layers might be important in interpreting the scintillations for Venus as well as for Uranus.

As a final cautionary note, we mention that statistical theories for fluctuations in light curves are based upon the starting premise of stationary statistics. A stationary ensemble is obtained only if a large number of occultations at identical levels in the atmosphere are compared.

B. Comparison of Temperature Structure

Mean temperatures and temperature profiles. Estimates of the mean temperature of the region of the atmosphere sampled during the occultation can be obtained both by numerical inversion and by modeling the light curves. Although the large intrinsic spike amplitude guarantees that the atmosphere is not perfectly isothermal, an isothermal model light curve fit to the observations does provide a measure of the mean scale height, which governs the overall rate of diminution of stellar intensity. We performed isothermal fits on all of the immersion light curves and on the CTIO emersion data. The mean temperatures we obtained are shown in Table V. A mean immersion temperature of 146°K was found. The CTIO emersion temperature was 156°K. The characteristic uncertainty in these values, as for the inversion results that follow, is ±15°K.

TABLE V

MEAN ATMOSPHERIC TEMPERATURES

Station	Event	$\bar{T}$ (isothermal fit) (°K)	$\bar{T}$ (inversion)[a] (°K)
CTIO	I	151	156
ESO	I	143	152
CLCO	I	145	140
Average		146	149
CTIO	E	156	

[a] The mean inversion temperatures are averaged over an altitude interval of ~160 km centered at number density ~3 × 10^{14} cm^{-3} and pressure ~6 × 10^{-3} mbar.

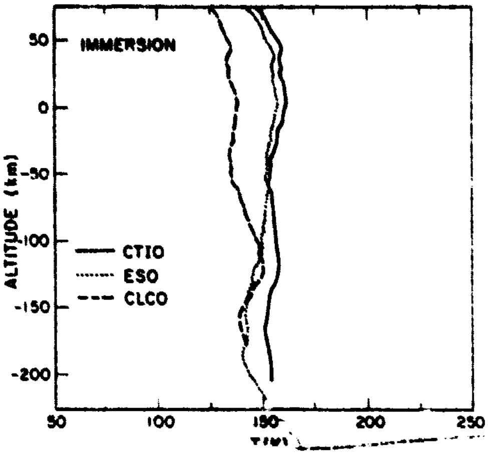

FIG. 7. Temperature profiles obtained by numerical inversion of the immersion light curves. The profiles are aligned in altitude at the level corresponding to the astrometric half-light time, given in Table III, which for CTIO is at number density 1.3 × 10^{14} cm^{-3} and pressure 3.2 × 10^{-3} mbar.

Using the results of the isothermal fits to define the full and zero stellar intensity levels, we obtained immersion temperature profiles by numerical inversion using the method of French *et al.* (1978). The method assumes that the atmosphere is stratified and that ray crossing is not severe. The adopted atmospheric parameters used in the calculations are listed in Table VI, and the profiles are shown in Fig. 7. The profiles are aligned in altitude at the level corresponding to the astrometric half-light time, given in Table III, which for CTIO is at number density 1.2 × 10^{14} cm^{-3} and pressure 3.2 × 10^{-3} mbar. Because of the instability of the initial condition of the inversion method, the profiles shown extend only to about one scale height above the half-light level, and the temperature gradients must be regarded as uncertain. The interval along the light curve used in the inversion can be estimated by comparing the altitude scales in Figs. 2 and 7. Similar profiles were obtained for the CLCO data by Nicholson *et al.* (1982a), who used the inversion algorithm of French *et al.* (1978), and for the ESO data by Sicardy *et al.* (1982), who used the inversion technique described by Vapillon *et al.* (1973). We note that Nicholson *et al.* (1982a) obtained CLCO immersion temperatures that are as much as 15°K lower than our results at the bottom of the temperature profiles. These differences appear to be attributable to the ~1% uncertainty in the base levels of the independently digitized data.

TABLE VI

ADOPTED ATMOSPHERIC PARAMETERS

Mean molecular weight	2.2 g mole^{-1}
Acceleration of gravity	818 cm sec^{-2}
Atmospheric refractivity (STP)	1.26 × 10^{-4}
Temperature/scale height	2.16°K km^{-1}

If the light curves were noise-free and the atmosphere perfectly layered, then the deduced temperature profiles would be identical. In fact, although they have many similar features, there are significant differences. The overall temperature gradients differ, as do the altitudes of several common features. Since the depth in the atmosphere is inferred by integrating the light curve in time [see French *et al.* (1978) for details], an error of a few percent in the assumed zero intensity level can produce significant distortions in the temperature profile.

Fortunately, the high degree of correla-

013

ORIGINAL PAGE IS
OF POOR QUALITY

tion in the spikes allows us to compensate for these distortions. Spikes present in all three light curves, displaced in time by the differences in astrometric half-light times, provide markers which reveal the extent of the altitude distortion. In order to compare the detailed structure of the temperature profiles, we removed the best-fitting linear temperature gradient from each profile over the altitude range corresponding to the time interval from 7 sec prior to astrometric half-light to 85 sec after half-light (corresponding to an altitude range from 25 km above half-light to 135 km below the half-light altitude for the CTIO observations). This is the same altitude interval used by Dunham *et al.* (1980) to display the March 1977 Uranus atmosphere results. The resulting temperature difference profiles ("ΔT profiles") are shown in Fig. 8 and the mean temperature from each fit is given in Table V. The average immersion temperature obtained by numerical inversion is 149°K. Note carefully that the altitude scale applies only to the CTIO data; the other profiles were linearly stretched or compressed in altitude as dictated by the spike alignment.

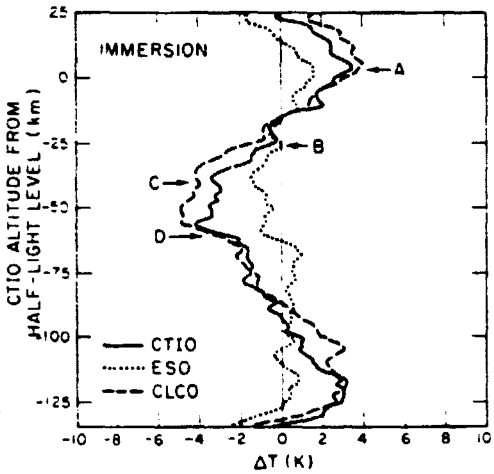

FIG. 8. Deviations of temperature profiles from a constant temperature gradient for immersion. The profiles were aligned and scaled vertically as described in the text. The detailed agreement is quite striking, and is best between CTIO and CLCO, the most distant stations. We attribute the poorer agreement of the low-frequency components of the ESO data to known difficulties in guiding during immersion. Features labeled A through D, discussed in the text, are produced by the correspondingly labeled features in the light curves shown in Fig. 9.

The ΔT profiles show close agreement, especially for CTIO and CLCO, the two most distant stations. All profiles have a ±5°K wavelike feature of similar phase and vertical wavelength of about two scale heights. The smaller-scale variations are the results of spikes on the light curve, and there is good, but not perfect, agreement here as well. The ESO profile deviates most strongly from the others below an altitude of −60 km, which we attribute to the same partial loss of signal we regard as responsible for the large error in the isothermal fit half-light time. Noise experiments confirm the plausibility of this suggestion. The atmospheric Fresnel vertical scale is ~2 km in the relevant regions for these observations, providing a resolution limit on the profiles in Fig. 8, since the assumptions of geometric optics are invalid at finer vertical scales.

C. The Relationship of Light Curve Spikes and Temperature Profiles

A light curve and its derived temperature profile contain the same information, in that each can be reproduced from the other, but the most prominent features in the light curve, the spikes, have only a minor effect on the temperature profile. The vertical wave in Fig. 8 is produced by slow modulation of the light curve. Since the light curves themselves are highly correlated, it is not surprising that the derived temperature profiles are as well, but the correlation is not perfect. It is instructive, therefore, to examine in detail several light curve spikes and the temperature variations they produce. We selected four such features in the high-resolution section of immersion data shown in Fig. 9. The corresponding features in the ΔT profile are labeled in Fig. 8.

Feature A. This is an example of a feature which is well correlated for two closely

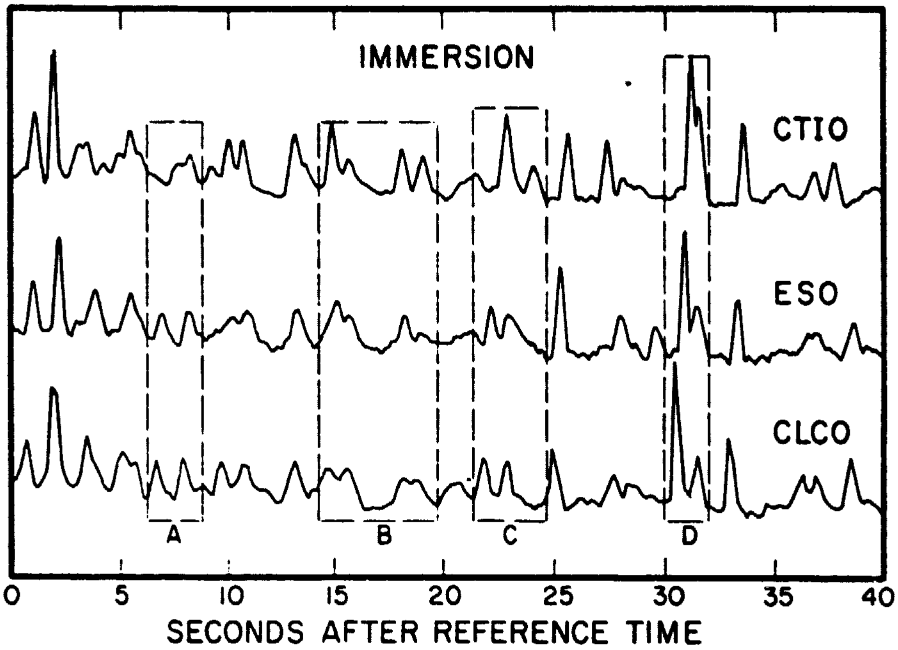

FIG. 9. High-resolution segment of immersion occultation light curves. Time is in seconds after the following reference times on 15 August 1980 (UT): CTIO, $22^{\rm h}38^{\rm m}01^{\rm s}01$; ESO, $22^{\rm h}38^{\rm m}05^{\rm s}40$; CLCO, $22^{\rm h}38^{\rm m}06^{\rm s}65$. Features labeled A through D, discussed in the text, produce the correspondingly labeled structures in the temperature profiles obtained by numerical inversion (Fig. 8).

spaced stations (ESO and CLCO), but weakly correlated with the most distant station, CTIO. The trough between the two spikes corresponds to a defocusing region, which can be thought of as a convexity in the stellar wavefront as it passes through the Uranus atmosphere. The convexity is produced by a rarefied region sandwiched between two relatively dense regions. The intensity of a spike depends upon the radius of curvature of the effective lens, which in this case involves the quantity d^2n/dr^2, where n is the number density and r is the altitude. The corresponding temperature fluctuation is indicated on the ΔT profile. The differences among the profiles of different stations are very slight, but are sufficient to produce noticeable differences in the light curve.

Feature B. This is a fine example of the gradual modification of spikes with distance along the limb. A large trough separates two pairs of spikes which are barely distinct in the CLCO data and are easily resolved in the CTIO light curve. The corresponding temperature maximum is quite pronounced in all three profiles.

Feature C. According to the layering model, sharp spikes correspond to regions of strong focusing, which are regions in the atmosphere where the temperature decreases sharply with height. In this case, two nearly identical spikes in the CLCO data migrate down the light curve and are delayed and altered when seen in the CTIO data. The delay of $\sim 1^{\rm s}2$ corresponds to an altitude difference of ~3 km over a horizontal separation of 144 km.

Feature D. Two distinct spikes in the CLCO light curve coalesce in the CTIO data and produce the sharp ledge indicated in the ΔT profile. Once again, distinct differences in the light curve are barely perceptible in the temperature profile.

ORIGINAL PAGE IS
OF POOR QUALITY

Other features. There are, conversely, prominent features in the temperature profile which are inconspicuous in the light curve. The sharp feature in the ESO and CLCO profiles at 110 km below half-light in Fig. 8 is barely visible in the CTIO profile. The differences are caused by slight differences in the depth of the "trough" in the light curve near time 120 sec (Fig. 2b).

D. Horizontal Coherence and the Validity of the Inversion Method

The spikes are clearly produced by coherent horizontal structures whose characteristic length is well over 100 km. However, the inversion method requires horizontal coherence over the effective path length in the atmosphere of ≳2300 km for the results to be strictly valid. We have seen that the spikes correspond to small inflections in the temperature profile, with a characteristic vertical extent of a few kilometers, and that the overall trend in the temperature profile is produced by low-frequency variations in the light curve. The computed CCFs are dominated by the spikes and are insensitive to these gradual, low-amplitude variations in intensity. Linear extrapolation of the immersion CCF in Fig. 5 shows that the correlation reaches zero at a separation less than the required coherence scale for numerical inversion. However, this is misleading, both because of the uncertainty of the extrapolation and because this coherence refers primarily to the sharp features in the light curve. More multiple observations are required to determine this important region of the cross-correlation, but it should be noted that agreement in the overall derived temperature profiles of widely spaced stations is itself evidence that the light curves are correlated. The unique mapping between light curves and temperature profiles obtained by stations separated by ~2000 km in the 1977 Uranus occultation (Dunham *et al.*, 1980) guarantees that the low-frequency structure of the light curves is similar. (This could be confirmed by synthesizing model light curves assuming an atmospheric refractivity profile corresponding to the lowest-order Fourier components of the derived temperature profiles.) In our view, the overall temperature profiles in Figs. 7 and 8 accurately reflect the general character of the vertical structure in the Uranus atmosphere at this time and location on the planet. The small-scale variations in the profiles, perhaps distorted somewhat by horizontal inhomogeneities in the atmosphere, are typical of the true atmospheric structure.

IV. CONCLUSIONS

Comparison of simultaneous observations of the 15 August 1980 occultation reveals strong similarity in the upper atmospheric structure of Uranus over distances of more than 100 km. Cross-correlation analysis of the light curves themselves suggests a horizontal coherence scale of at least 140 km for the features producing the sharp spikes. This is inconsistent with models of isotropic turbulence, and any acceptable anisotropic turbulence model must be able to account for axial ratios of 60. The spike correlation diminishes as the occultation proceeds, due in part to altitude variations of the atmospheric features and to slight changes in the wavefront curvature.

The results give credence to the temperature profiles obtained by numerical inversion, which can be used to investigate the structure and dynamics of the upper atmosphere of Uranus. The origin and maximum extent of the horizontal layers remain to be determined, but an upper limit to the strength of the quasi-isotropic component of turbulence can be obtained, which will provide a means of comparing the microstructure of the upper atmosphere of Uranus with other planets. In a future publication, we will compare the power spectrum of the intensity variations of these and other occultation observations with the predictions of weak-scattering turbulence

016

theory and with numerical realizations of strong, anisotropic turbulence. The great distance of Uranus from the Sun may account in part for the relative quiescence of the atmosphere, as discussed by French *et al.* (1982), and we must await further observations before concluding that these results are applicable to all planetary atmospheres.

ACKNOWLEDGMENTS

This work was supported in part by NASA Grants NAGW-68 and NSG-7526 and NSF Grant AST-8010699. B. Sicardy was supported by RCP-544-Anneaux, the ATP Planetologies of CNRS, the Observatoire de Paris, and l'Université de Paris, France. The observations at Cerro Las Campanas Observatory were supported by NASA grants.

REFERENCES

COMBES, M., L. VAPILLON, AND J. LECACHEUX (1975). The occultation of β Scorpii by Jupiter IV. Divergences with other observers in the derived temperature profiles. *Astron. Astrophys.* **45**, 399–403.

DUNHAM, E., J. L. ELLIOT, AND P. J. GIERASCH (1980). The upper atmosphere of Uranus: Mean temperature and temperature variations. *Astrophys. J.* **235**, 279–284.

ELLIOT, J. L. (1979). Stellar occultation studies of the solar system. *Annu. Rev. Astron. Astrophys.* **17**, 445–475.

ELLIOT, J. L., E. DUNHAM, D. J. MINK, AND J. CHURMS (1980). The radius and ellipticity of Uranus from its occultation of SAO 158687. *Astrophys. J.* **236**, 1026–1030.

ELLIOT, J. L., R. G. FRENCH, J. A. FROGEL, J. H. ELIAS, D. M. MINK, AND W. LILLER (1981). Orbits of nine Uranian rings. *Astron. J.* **86**, 444–455.

ELLIOT, J. L., AND J. VEVERKA (1976). Stellar occultation spikes as probes of atmospheric structure and composition. *Icarus* **27**, 359–386.

FJELDBO, E., A. J. KLIORE, AND V. R. ESHLEMAN (1971). The neutral atmosphere of Venus as studied with the Mariner V radio occultation experiments. *Astron. J.* **76**, 123–140.

FRENCH, R. G., AND J. L. ELLIOT (1979). Occultation of ε Geminorum by Mars III. Temperature structure of the Martian upper atmosphere. *Astrophys. J.* **229**, 828–845.

FRENCH, R. G., J. L. ELLIOT, E. W. DUNHAM, D. ALLEN, J. H. FROGEL, J. H. ELIAS, AND W. LILLER (1982). The thermal structure and energy balance of the Uranian upper atmosphere. In preparation.

FRENCH, R. G., J. L. ELLIOT, AND P. J. GIERASCH (1978). Analysis of stellar occultation data: Effects of photon noise and initial conditions. *Icarus* **33**, 186–202.

FRENCH, R. G., AND R. V. E. LOVELACE (1982). Stellar occultations, strong scintillation, and atmospheric waves. In preparation.

FRENCH, R. G., AND G. E. TAYLOR (1981). Occultation of ε Geminorum by Mars IV. Oblateness of the Martian upper atmosphere. *Icarus* **45**, 577–585.

HUBBARD, W. B. (1979). The ε Geminorum occultation: Evidence for waves or turbulence. *Astrophys. J.* **229**, 821–827.

HUBBARD, W. B., J. R. JOKIPII, AND B. A. WILKING (1978). Stellar occultations by turbulent planetary atmospheres: A wave-optical theory including a finite scale height. *Icarus* **34**, 374–395.

HUBBARD, W. B., AND T. C. VAN FLANDERN (1972). The occultation of Beta Scorpii by Jupiter and Io III. *Astron. J.* **77**, 65–74.

HUNTEN, D. M., AND J. VEVERKA (1976). In *Jupiter* (T. Gehrels, Ed.), pp. 247–288. Univ. of Arizona Press, Tucson.

JOKIPII, J. R., AND W. B. HUBBARD (1977). Stellar occultations by turbulent planetary atmospheres. *Icarus* **30**, 537–550.

KLEMOLA, A. R., AND B. G. MARSDEN (1977). Predicted occultations by the rings of Uranus, 1977–1980. *Astron. J.* **82**, 849–851.

KOVALEVSKY, J., AND F. LINK (1969). Diamètre, aplatissement et propriétés optiques de la haute atmosphère de Neptune d'après l'occultation de l'étoile BD-174388. *Astron. Astrophys.* **2**, 398–412.

LECHACHEUX, J., M. COMBES, AND L. VAPILLON (1973). The β Scorpii occultation by Jupiter I. The Jovian diameter. *Astron. Astrophys.* **22**, 289–292.

NICHOLSON, P. D., *et al.* (1982a). In preparation.

NICHOLSON, P. D., K. MATTHEWS, AND P. GOLDREICH (1982b). Radial widths, optical depths, and eccentricities of the Uranian rings. *Astron. J.* **87**, 433–447.

SEIFF, A., AND D. B. KIRK (1977). Structure of the atmosphere of Mars in summer at mid-latitudes. *J. Geophys. Res.* **82**, 4364–4378.

SEIFF, A., D. B. KIRK, R. E. YOUNG, R. C. BLANCHARD, J. T. FINDLAY, G. M. KELLY, AND S. C. SOMMER (1980). Measurements of thermal structure and thermal contrasts in the atmosphere of Venus and related dynamical observations: Results from the four Pioneer Venus probes. *J. Geophys. Res.* **85**, 7903–7933.

SICARDY, B., M. COMBES, P. BOUCHET, A. BRAHIC, AND C. PERRIER (1982). In preparation.

TAYLOR, G. E. (1974). *Nautical Almanac Office Technical Note No. 34*. Royal Greenwich Observatory, Hailsham, Sussex, England.

Texas–Arizona Occultation Group (1977). The occultation of Epsilon Geminorum by Mars: Analysis of McDonald data. *Astrophys. J.* **214**, 934–945.

017

ORIGINAL PAGE IS
OF POOR QUALITY

VAPILLON, L., M. COMBES, AND J. LECACHEUX (1973). The Beta Scorpii occultation by Jupiter II. The temperature and density profiles of the Jovian upper atmosphere. *Astron. Astrophys.* **29**, 135–149.

WOO, R., J. ARMSTRONG, AND A. ISHIMARU (1980). Radio occultation measurements of turbulence in the Venus atmosphere by Pioneer Venus. *J. Geophys. Res.* **85**, 8031–8038.

ZUREK, R. W. (1976). Diurnal tide in the Martian atmosphere. *J. Atmos. Sci.* **33**, 321–337.

018

APPENDIX C

THE THERMAL STRUCTURE AND ENERGY BALANCE OF THE URANIAN UPPER ATMOSPHERE

THE THERMAL STRUCTURE AND ENERGY BALANCE OF THE URANIAN UPPER ATMOPSPHERE

by

R.G. French[1,2], J.L. Elliot[1,3,4], E.W. Dunham[1],
D. Allen[5]
J.H. Elias[6], J.A. Frogel[6]
W. Liller[4,7,8]

[1] Department of Earth and Planetary Sciences
Massachusetts Institute of Technology
Cambridge, MA 01239

[2] Department of Astronomy
Wellesley College
Wellesley, MA

[3] Department of Physics
Massachusetts Institute of Technology
Cambridge, MA 02139

[4] Visiting Astronomer, Cerro Tololo Inter-American Observatory
Supported by the National Science Foundation
Under Contract No. AST 78-27879

[5] Anglo-Australian Observatory
P.O. Box 296
Epping NSW 2121, Australia

[6] Cerro Tololo Inter-American Observatory
La Serena, Chile

[7] Harvard-Smithsonian Center for Astrophysics
Cambridge, MA 02138

[8] Isaac Newton Institute
Santiago, Chile

Submitted to *Icarus*
1982

ABSTRACT

Two occultation observations of the upper atmosphere of Uranus are reported: (i) the 15-16 August 1980 occultation of KM 12 from Cerro Tololo Inter-American Observatory, and (ii) the 26 April 1981 occultation of KME 13 from the Anglo-Australian Telescope and the 1-meter telescope of the Australian National University. Mean atmospheric temperatures of 154 ± 15K for the 1980 event and 132 ± 15K for the 1981 event are derived from the light curves. A comparison of all available Uranus occultation data since March 1977 suggests that the mean atmospheric temperature of Uranus has changed significantly, with a typical variation of 15K yr^{-1}. We investigate plausible energy sources that might account for such large temperature variations. We conclude that molecular and eddy diffusion, and atmospheric dynamics, are as important as radiation to the upper atmospheric heat balance. There is evidence that no significant radiative cooling had occurred at two sub-occultation points that had been in darkness for more than 0.5 terrestrial yr., suggesting upper limits to the mixing ratios of CH_4 and C_2H_2 of 6×10^{-5} and 5×10^{-7}, respectively. The consistently close agreement of immersion and emersion mean temperatures for each occultation, in spite of apparently large secular changes in the atmospheric mean temperature, suggests that effective meridional transport occurs on Uranus. A continuing program of occultation observations in future years should reveal whether this pattern is significant.

I. INTRODUCTION

Stellar occultation observations have revealed that the upper atmospheres of Jupiter (Veverka et al., 1974a), Uranus (Elliot and Dunham, 1979; Dunham et al., 1980), and Neptune (Veverka et al., 1974b) do not exhibit the quasi-isothermal characteristic of stratospheres purely in radiative equilibrium but have strong temperature variations of large vertical and horizontal extent. By monitoring the thermal structure of these atmospheres, we can develop an observational context for a better understanding of upper atmospheric energy balance and dynamics.

In this paper, we describe the results of two recent occultation observations of Uranus and investigate the relative importance of radiation, molecular and eddy diffusion, and wave dynamics to the thermal structure of the Uranian stratosphere. On 15-16 August 1980, Uranus occulted KM 12, the twelfth star on the list of Klemola and Marsden (1977). The event was widely observed, and based on a comparison of light curves obtained from Cerro Tololo Interamerican Observatory (CTIO), European Southern Observatory (ESO) and Cerro Las Campanas Observatory (CLCO), we have concluded that the Uranian atmosphere is not strongly turbulent, and has the same vertical structure over large horizontal distances (French et al., 1982). On 26 April 1981, Uranus occulted KME 13 (Klemola, Mink and Elliot, 1981). We observed the event with the Anglo-Australian Telescope (AAT) and with the 1-meter telescope of the Australian National University (ANU). We describe the observations in the next section, and present the derived atmospheric temperature profiles in §III. In §IV, we consider the relative importance of plausible energy sources to the upper atmospheric heat balance, and in the final section, we summarize our understanding of the thermal structure of the Uranian upper atmosphere.

II. Observations and Data Reduction

Observations of the 15-16 August 1980 occultation of KM 12 by Uranus and its rings were carried out in the K band (λ = 2.2 μm, $\Delta\lambda$ = 0.4 μm) with the CTIO InSb system mounted on the 4 m telescope (Frogel and Elias, 1980). The general characteristics of the observations have been described in some detail in our analysis of the ring data (Elliot et al., 1981). The immersion and emersion light curves are shown in Figs. 1 and 2. During emersion, cirrus clouds were present and were responsible for the variations in signal level near 00:16:30 UT. The immersion signal is much cleaner, and we shall devote most of our attention to this event. The light curves are characterized by numerous sharp spikes. From a detailed comparison of observations from several stations, we find that the spikes are not caused by isotropic turbulence, but are produced by layered atmospheric structure which extends at least 140 km along the limb of the planet (French et al., 1982).

We observed the 26 April 1981 occultation of KME 13 by Uranus and its rings with the AAT infrared system in the K band (λ = 2.2 μm; Barton and Allen, 1980). The ring events will be decribed in a future publication. The immersion and emersion light curves obtained from AAT are shown in Figs. 3 and 4; the immersion event as seen from the 1 m telescope of the Australian National University (ANU) is shown in Fig. 5. Because the ANU observations were made at 0.8 μm, the signal was contaminated by light from Uranus and the data are significantly noisier than the AAT data, which were taken in the 2.2 μm band, where the contribution from Uranus is small; however, the unocculted stellar flux was roughly 4% of the background at the ANU.

On the basis of a simultaneous solution for the best fitting coplanar, precessing elliptical orbits of the nine confirmed Uranian rings, using the pole of the ring plane as determined by Elliot _et_ _al_. (1981), we determined the occultation geometry as shown in Fig. 6. From the event astrometry, and assuming a planetary oblateness of 0.024 (Elliot _et_ _al_., 1981), we computed $v_\perp$, the event velocity perpendicular to the planetary limb. This is tabulated in Table I for the midpoint of the occultation, defined by $t_{1/2}$, the time at which the best-fitting isothermal light curve reached half-intensity.

All of the light curves contain fluctuations that are caused partly by noise and partly by Uranus' atmosphere. To determine the contribution due to Uranus, we first obtained a measure of the rms noise in the occultation data, according to the relation

$$\varepsilon = \frac{(\Delta t)^{1/2}}{n_*}\left[\frac{1}{N-1}\sum_{j=1}^{N}[n(t_j) - \bar{n}]^2\right]^{1/2} \qquad (1)$$

where ε is the rms noise in the light curve for a one-second integration, expressed as a fraction of n_*, the counts per second for the unocculted star; $n(t_j)$ is the mean counting rate in counts per second for the j^{th} integration bin of duration

Δt, N is the total number of integration bins used in the calculation, and $\bar{n}$ is the mean counting rate in counts per second for all N integration bins.

For the 15-16 August 1980 data, we computed ε using the parameters described in French et al. (1982). For the AAT data of 26 April 1981, we used a total of 50s of data (at a time resolution of $\Delta t = 0.1$s) prior to immersion, when the only variations in the light curve would be due to noise, and computed the average ε for a running mean of 4s duration (corresponding to $N = 40$). The results are given in Table I. Because emersion was observed at dawn, the post-emersion light curve at AAT was rising rapidly, making it difficult to estimate ε during the occultation, and we have assigned the immersion AAT noise level to the emersion data as well. For comparison with other occultation data, we have computed a dimensionless measure of the noise level of an occultation, given by $\varepsilon(v_\perp/H)^{1/2}$ (French et al., 1978). This is the rms noise, as a fraction of the unocculted stellar flux, over the time interval during which the star probes one scale height in the atmosphere. The results are given in Table I.

Once the contribution of noise to the total fluctuation strength is known, the intrinsic rms spike amplitude in the light curve due to Uranus' atmosphere can be computed, according to:

$$\langle \Delta\phi^2_u \rangle^{1/2} = \left\{ \left[\frac{1}{N} \sum_{i=1}^{N} \Delta\phi^2_i\right] - \varepsilon^2/\Delta t \right\}^{1/2} \qquad (2)$$

where $\Delta\phi_i$ is the ith observed residual of the light curve from the local mean, normalized by the unocculted stellar intensity. For the 1980 observations, a data interval between 10^s before the half light level and 20^s after the half light level was used for immersion, and a symmetric interval for emersion. The corresponding interval, scaled by the corresponding $v_\perp$, was used for the 1981 observations: between 23^s before half light and 45^s after half light. The results are given in Table I. Photon noise and terrestrial scintillation are not dominant sources of fluctuation power, except for the ANU immersion data, the noisiest observation. The rms spike amplitudes are very similar (≈ 0.2) for all events except for 16 August 1980 emersion, where the rms amplitude is significantly larger.

ORIGINAL PAGE IS
OF POOR QUALITY

III. Thermal Structure of the Uranian Upper Atmosphere

The isothermal model light curves fit to the data in Figs. 1-5 provide a measure of the mean temperature of the Uranian upper atmosphere. For the perpendicular velocities given in Table I and a value of 2.16 K km^{-1} for the ratio of temperature to scale height, we obtained the temperatures given in Table II. Since the atmosphere is manifestly non-isothermal ($[\Delta\phi_u{}^2]$ is non-zero), the formal errors of the fits give no clue to the uncertainties of the temperature estimates. To proceed further, we adopted the usual assumptions of the numerical inversion method to obtain temperature profiles from occultation light curves. The method is described in French _et_ _al_. (1978). The critical assumption is that the atmospheric density varies only with radius. For Uranus, the observations of the 15-16 August 1980 occultation support the validity of this assumption, since details of the atmospheric vertical structure persist essentially unchanged over large horizontal distances (French _et_ _al_., 1982). We adopted an acceleration due to gravity of 818 cm s^{-2} and an atmospheric refractivity at STP of 1.26×10^{-4} (corresponding to an atmosphere of 90% H_2 and 10% He by number). The levels corresponding to full and zero stellar intensity were determined from the isothermal fits.

The temperature profiles we obtained are shown in Fig. 7. The inversion procedure is particularly sensitive to noise in the light curve at the onset of the occultation, and because of the significant signal variations due to clouds during emersion on 16 August 1980, we have not shown the CTIO emersion temperature profiles, which we regard as unreliable. To determine the effects of noise in the data on the derived temperature profiles, we superimposed on an isothermal light curve actual noisy data prior to immersion for each occultation and obtained the corresponding temperature profiles. For CTIO and AAT data, the noise caused only low-frequency variations in the temperature profile of less than 1 K amplitude. However, the ANU data are sufficiently affected by terrestrial scintillation and background light from Uranus that the noise-induced temperature variations in the derived profiles are about 5 K in amplitude. Consequently, we regard these inversion results as unreliable.

The temperature profiles in Fig. 7 are aligned vertically at the altitude corresponding to the time of half-light on each light curve; the number density at the half-light altitude is $\sim 10^{14}$ cm^{-3} and the pressure is ~ 3 μb. The mean temperatures of the atmosphere, computed over the interval from 25 km above to 150 km below the half-light altitude, are given in Table II. This is the region in which the inversion results are most reliable: at higher altitudes the initial condition of the inversion strongly influences the results, and deeper in the atmosphere, uncertainties in the baseline corresponding to zero stellar intensity are important.

Because the major noise source is terrestrial scintillation rather than photon noise, and because the assumptions of the inversion method are not absolutely satisfied, it is difficult to quantify the uncertainty in the overall placement of the temperature profiles, but we estimate them to be accurate to ±15K. This estimate takes into account station-to-station variations for multiply observed occultations, as well as differences resulting from independent analysis of the same observations by different investigators. We emphasize that the variations in the temperature profiles are more reliable than their means or gradients and accurately represent the true atmospheric state to the extent that the atmosphere can be regarded as perfectly layered. Although the full horizontal extent of the stratification has not yet been determined, it has been demonstrated that the effects of isotropic turbulence in the Uranus atmosphere do not invalidate the inversion procedure (French et al., 1982). In what follows we assume that the derived profiles correspond to the true atmospheric structure and investigate the implications for the energy balance in the stratosphere. Additional multiple station occultation observations are necessary before more definitive conclusions can be drawn.

Every temperature profile obtained to date of the Uranian upper atmosphere reveals temperature variations of from ±5K to ±30K with a characteristic vertical scale of two scale heights. Multiple observations of the 15-16 August 1980 occultation reveal that these are not the artifacts of atmospheric turbulence, but are genuine characteristics of the layered atmosphere (French et al., 1982). The immersion and emersion AAT profiles have quite different structure, with the large amplitude immersion variations reminiscent of the 10 March 1977 temperature profile (cf. Fig. 5b, Dunham et al., 1980). Also present are variations of a few tenths of a degree K over an altitude of a few km. These smaller-scale features are not due to noise, since for the 1980 data the structure is matched in detail in the temperature profile obtained from the CLCO immersion data, separated by 144 km along the limb (cf. Fig. 7, French et al., 1982).

The upper atmospheric structure of Uranus has been determined from observations of four separate stellar occultations between March 1977 and April 1981. In Fig. 8 we compare the mean temperature as determined from numerical inversion and isothermal fits to the light curve, as reported for each of these events: the 10 March 1977 results are from Dunham et al. (1980), the 10 June 1979 results from Nicholson et al. (1982), and both the 15-16 August 1980 and the 26 April 1981 results are from this work. In each case, the mean temperature obtained by numerical inversion was determined over the altitude interval from 25 km above the half-light level to 150 km below the half-light level. Two features are worth noting: first, the average temperature obtained by inversion varies by several tens of K over the four year interval for which data are available; second, the variation from occultation to occultation is generally larger than the difference between immersion and emersion mean temperatures for a given date.

Are these characteristics significant, or are the uncertainties in the results sufficiently large that they are

ORIGINAL PAGE IS
OF POOR QUALITY

consistent with an unchanging mean atmospheric temperature? A spirit of caution is in order when considering the results in Fig. 8. It is important to bear in mind that isothermal fits to non-isothermal light curves may give systematically erroneous mean temperatures. For example, for the March 1977 results, both immersion and emersion isothermal fit temperatures are ~20 K warmer than the corresponding inversion temperatures. Also, it is difficult to define the mean temperature precisely when the observed profiles show large temperature variations with height, although we have adopted a uniform procedure for all derived temperature profiles. In spite of these caveats, we regard the trends in Fig. 8 as provocative and we shall accept them at face value for the purposes of discussion. As more observations become available, it should become clear whether these characteristics persist, or are fortuitous groupings of data points.

IV. The Upper Atmospheric Energy Budget

The observations in Fig. 7 and 8 raise a number of questions:

- What is the energy source for the vertical temperature variations?
- What are the time scales for the plausible growth and destruction mechanisms at work?
- How important are the observed small-scale temperature variations to the overall energy balance?
- Are the large-scale thermal variations a dynamical or a radiative phenomenon?
- What is the cause of the apparent secular changes in the mean atmospheric temperature over the observed four year period?
- Why are immersion and emersion mean temperatures generally so similar for a given occultation, in spite of the antipodal separation of the suboccultation points?

We begin our discussion of these issues by summarizing the characteristics of existing atmospheric models and comparing them with the observations. Next, we consider the energetics of radiation, diffusion, and wave motion under Uranian upper atmospheric conditions; then we determine the diurnally and orbitally averaged insolation on Uranus. Finally, we examine the observations and indicate what further information will be necessary to resolve the uncertainties.

IV.A. Atmospheric Results

The most detailed models of the thermal structure of the Uranian atmosphere have been developed by Wallace (1975, 1980) and Appleby (1980). For the region of interest here (number density ~10^{14} cm^{-3}; pressure ~3 μb) and for plausible concentrations of CH_4, C_2H_2, and C_2H_6, the important energy balance in these models involves radiation in the methane bands. A simple balance between heating by absorption of solar radiation in the ν_3 (3.3 μm) band and cooling by radiation in the ν_4 (7.7 μm) band predicts a radiative equilibrium temperature of 125K over the region where methane is optically thin. This calculation assumes that LTE applies and that other energy sources are not significant. The abundances of effective infrared radiators such as CH_4, C_2H_2, and C_2H_6 in the stratosphere are unknown. Gillett and Rieke (1977) obtain an upper limit of $\eta_{CH_4} = [CH_4/H_2] \lesssim 3 \times 10^{-6}$, based on their IR observations and an assumed temperature of 125K. However, Appleby (1980) obtains $\eta_{CH_4} = 3 \times 10^{-5}$, on the basis of model calculations, and feels that this value is not ruled out by Gillett and Rieke's (1977) observations. By varying the CH_4, C_2H_2, and C_2H_6 abundances and taking proper account of non-LTE effects, Appleby has produced a variety of models with mean upper atmospheric temperatures ranging from 105K to 130K (cf. Fig. 33, Appleby (1980)). However, none of these models exhibits the relatively rapid variations of temperature with altitude which are observed. Clearly, some additional physical process is at work.

IV.B. Heating and Cooling Mechanisms

In the absence of detailed information, we begin by investigating in a simple way the relative importance of radiation, diffusion (both eddy and molecular), and dynamics to upper atmospheric heating and cooling. These are the principal energy sources and sinks at these pressure levels. (We can ignore aerosol heating because the fallout rate of aerosol particles, governed by Epstein drag, is very large at these altitudes. An enormous aerosol production rate would be required to maintain a significant aerosol abundance.) We first present the functional forms of heating and cooling rates, and then evaluate the expression for a specific example of interest.

Radiation

The thermal energy density, ΔE, of a temperature perturbation of amplitude ΔT is given by

$$\Delta E = \mu m_H c_p \Delta T \qquad (3)$$

where μm_H is the mean molecular weight in gm, n is the atmospheric number density, and c_p is the specific heat per gm at constant pressure. If the vertical extent of the perturbation is of order the scale height, H, then $H\Delta E$ represents the thermal energy per unit surface area contained in the disturbance.

The radiative heating flux, F_{rh}, absorbed by an optically thin gas within this altitude range is

$$F_{rh} = \langle D \rangle f_\lambda W \qquad (4)$$

where $\langle D \rangle$ is the diurnally averaged insolation, expressed as a fraction of f_λ, the normal incidence solar flux outside Uranus' atmosphere per unit area and wavelength interval. An upper limit to the equivalent width, W, of the band, adequate for this scaling analysis, is given by assuming that the band is optically thin:

$$W = b\eta nH/L \qquad (5)$$

where b is the band strength (in $\mu m\ cm^{-1}\ am^{-1}$), η is the fractional abundance of the absorbing gas and L is Loschmidt's number. (Under these assumptions, W is an upper limit to the true equivalent width.)

Combining Eqs. 3-5, and approximating the flux divergence as F_{rh}/H, we can determine the characteristic time, τ_{rh}, to heat the atmosphere by radiation:

$$\tau_{rh} = H\Delta E/F_{rh} \qquad (6)$$

or

$$\tau_{rh} = \mu m_H c_p LT/b\eta f_\lambda \langle D \rangle$$

The corresponding radiative heating rate is

$$(dT/dt)_{rh} = b\eta f_\lambda \langle D \rangle / \mu m_H c_p L \qquad (7)$$

The radiative heating rate is independent of the atmospheric density, in this approximation, and depends primarily on the abundance of the absorbing gas and the location of the absorption on the solar radiation curve. It is important as an indication of the rapidity of changes in thermal structure in a stratified atmosphere due to radiative imbalance.

Analogously, a radiative cooling time for the Uranus atmosphere can be estimated. Using the formalism of Strobel and Smith (1973), Wasserman (1974) estimated diurnal temperature variations in the Jovian upper atmosphere. We adopt Wasserman's notation and apply his Eqs. (1-4) to obtain radiative cooling rates for CH_4 and C_2H_2. For each constituent

$$\left(\frac{dT}{dt}\right)_{rc} = \frac{-Ah\nu nn(g_1/g_0)\exp(-h\nu/kT)P_{1\to 0}Z}{\mu m_H c_p(A + P_{1\to 0}Zn)} \qquad (8)$$

where A is the transition probability, h = Planck's constant, ν is the frequency associated with the transition, n is the mixing ratio of the radiator, g_1 and g_0 are statistical weights, k is Boltzmann's constant, $P_{1\to 0}$ is the probability of of collisional de-excitation, Z is the temperature-dependent collision frequency, and n is the total gas density.

Eddy Diffusion

Bulk atmospheric motion in the form of turbulence carries an associated energy flux, F_e, which can be approximated as

$$F_e = \mu m_H n g K \qquad (9)$$

where g is the acceleration of gravity and K is the eddy diffusion coefficient (in $cm^2\ s^{-1}$). The corresponding heating rate for eddy transport is as follows:

$$\left(\frac{dT}{dt}\right)_e = gK/Hc_p \qquad (10)$$

Here, it is assumed that the layer over which F_e varies significantly is one scale height deep.

Molecular Diffusion

The molecular diffusion flux is

$$F_m = -2\mu m_H c_v (dT/dz)(kT/\pi\mu m_H)^{1/2}/3\sigma \tag{12}$$

where c_v is the specific heat at constant volume, k is Boltzmann's constant, T is the mean atmospheric temperature, σ is the collision cross-section of the dominant atmospheric constituent, and dT/dz is the mean vertical temperature gradient (Reif, 1965). The corresponding molecular diffusion cooling rate is

$$\left(\frac{dT}{dt}\right)_m = \left(\frac{-2}{3\sigma n\gamma}\right)\left(\frac{g}{\pi H}\right)^{1/2}\left(\frac{dT}{dz}\right) \tag{13}$$

Here, γ is the ratio of specific heats. Molecular conduction time scales thus decrease roughly exponentially with increasing altitude.

Atmospheric Waves

Typical wave dynamical energy fluxes are given by (French and Gierasch, 1974):

$$F_w = \gamma\overline{wp}/(\gamma-1) \tag{14}$$

Here, w is the vertical velocity of the propagating mode, and the overbar denotes a time average. The dynamical energy flux depends strongly on the properties of the particular propagating wave in question. The corresponding wave dynamical heating rate is

$$\left(\frac{dT}{dt}\right)_w = \gamma\overline{wp}/(\gamma-1)\mu n c_p H \tag{15}$$

An implicit assumption of Eq. 15 is that the wave deposits a significant fraction of its energy in the region in question.

IV.C. Solar Energy Budget

Armed with the preceding expressions, we can evaluate the relative importance of these energy sources and sinks to the thermal balance of the upper atmosphere. Before proceeding with a specific example appropriate for the occultation region, however, we shall provide a context for discussion of time constants by computing the diurnally and orbitally averaged solar flux at Uranus as a function of latitude.

For a planet whose rotation period is much shorter than its orbital period, the diurnally averaged insolation at latitude θ, in units of the normal-incidence solar constant at the planet, is given by

$$\langle D \rangle = \frac{1}{2\pi} \int_0^{2\pi} z(\lambda,\ \theta,\ \theta_p,\ \phi) u_{-1}(z) d\lambda \qquad (16)$$

where

$$z(\lambda,\ \theta,\ \theta_p,\ \phi) = \cos\ \phi(\cos\theta_p\ \sin\lambda - \sin\theta_p\ \cos\lambda\ \sin\theta) - \sin\phi\ \cos\theta\ \cos\lambda \qquad (17)$$

In these expressions, θ_p is the angle between the rotation axis and the orbital plane, λ is longitude, ϕ is the angle between the sun and the projection of the rotation axis into the orbital plane (hence ϕ varies as the planet moves in its orbit), and $u_{-1}(z)$ is the Heaviside step function:

$$u_{-1}(z) = \begin{cases} 0 & z < 0 \\ 1 & z > 0 \end{cases} \qquad (18)$$

Similarly, the latitude dependence of the insolation averaged over the entire orbit can be expressed as

$$\langle A\rangle = \frac{1}{2\pi}\int_0^{2\pi}\langle D(\theta,\ \theta_p,\ \phi)\rangle d\phi \qquad (19)$$

where, again, the average insolation is expresed as a fraction of the normal incidence solar constant at the planet. For simplicity, we have assumed that the orbit is circular.

Fig. 9 shows $\langle D\rangle$ for the geometry appropriate for the dates of observed Uranus atmosphere occultations. The sampled sub-occultation latitudes are indicated by dots. Table III lists $\langle D\rangle$ for specific occultation observations. Notice that, because of the orientation of Uranus' pole and the phase angle of the observations, two events probed regions of the atmosphere which had received *no* solar radiation for many planetary rotations: the 10 June 1979 CLCO emersion sub-occultation point had been in darkness for 0.5 terrestrial yr; the 15 August 1980 immersion CTIO sub-occultation point for ~0.75 yr. The Uranian day is ~16 hours long (Elliot *et al.*, 1981). The orbitally averaged insolation, $\langle A\rangle$, is shown in Fig. 10. Because of the extreme obliquity of Uranus, the equatorial regions sampled by the occultations receive significantly less radiation than the polar regions. The orbital period of Uranus is 84 yr.

IV.D. Heating and Cooling Rates for Uranus' Upper Atmosphere

We now compute energy fluxes and time constants for the specific circumstances appropriate for the occultation region.

We assume Appleby's (1980) mixing ratios of $n_{CH_4} = [CH_4]/[H_2] = 3 \times 10^{-5}$ and $n_{C_2H_2} = [C_2H_2]/[H_2] = 10^{-8}$, although these must be regarded as only educated guesses, and adopt the parameter values given in Table IV. The 3.3 μm (ν_3) methane band strength is computed from Appleby's (1980) careful evaluation of available band intensities. The radiative heating rate in the CH_4 ν_3 band is, from Eq. (7)

$$\left(\frac{dT}{dt}\right)_{rh} = 0.3 \left[\frac{n_{CH_4}}{3 \times 10^{-5}}\right] \left[\frac{\langle D \rangle}{0.25}\right] \text{ K yr}^{-1} \qquad (20)$$

and the corresponding characteristic heating time is

$$\tau_{rh} = 460 \left[\frac{T}{125K}\right] \left[\frac{3 \times 10^{-5}}{n_{CH_4}}\right] \left[\frac{0.25}{\langle D \rangle}\right] \text{ yr} \qquad (21)$$

The cooling rates for radiation by CH_4 and C_2H_2 are calculated from Eq. (8) and are shown in Figs. 11 and 12 for a range of atmospheric temperatures and number densities, and selected values of the cooling rates and corresponding radiative relaxation times are given in Table V. For temperatures and densities comparable to those sampled during the occultation ($T \sim 100$-150 K, $n \sim 10^{13}$-10^{15} cm^{-3}), radiative cooling times are significantly longer than a year, particularly for low temperatures and densities. Naturally, the greatest uncertainties in these figures are the minor constituent abundances, n_{CH_4} and $n_{C_2H_2}$. We shall return to this point.

The eddy diffusion heating rate is, for the conditions of the occultation and for parameter values in Table IV:

$$\left(\frac{dT}{dt}\right)_e = 3.8 \left[\frac{K}{10^5(\mathrm{cm}^2\mathrm{s}^{-1})}\right] \mathrm{K\ yr}^{-1} \qquad (21)$$

and the characteristic eddy heating time is

$$\tau_e = 33 \left[\frac{10^5(\mathrm{cm}^2\ \mathrm{s}^{-1})}{K}\right] \mathrm{yr} \qquad (22)$$

For molecular diffusion, the corresponding relations are

$$\left(\frac{dT}{dt}\right)_m = -2.8 \left[\frac{10^{14}\mathrm{cm}^{-3}}{n}\right] \mathrm{K\ yr}^{-1} \qquad (23)$$

and

$$\tau_m = 45 \left[\frac{n}{10^{14}\mathrm{cm}^{-3}}\right] \mathrm{yr} \qquad (24)$$

for a vertical temperature gradient of 0.2 K km^{-1}. Typical values for these quantities are given in Table VI. At low number densities, the molecular diffusion time is much shorter than the radiative relaxation time, and even as low an eddy viscosity as $K = 10^5$ cm^2 s^{-1} yields a time constant shorter than typical radiative relaxation times at 125K. Evidently, radiative heating and cooling are slow processes in the stratosphere of Uranus. The lack of detectable cooling over the long times during which the 1979 CLCO emersion and the 1980 CTIO immersion sub-occultation points were in darkness is consistent with the adopted values of n_{CH_4} and $n_{C_2H_2}$. However, if n_{CH_4} were as large as 6×10^{-5} and $n_{C_2H_2}$ were as large as 5×10^{-7}, an overall stratospheric cooling of about 20K would have taken place over the long nighttime, and such a cooling is not evident in Fig. 8. We therefore rule out such large abundances, unless there is effective horizontal mixing.

Radiative equilibrium calculations for Uranus make precise predictions about the thermal structure because of the strong temperature dependence of the 7.7 μm CH_4 emission; the Wien region of the blackbody curve of Uranus is extremely steep in this wavelength range. This acts as a highly effective thermostat, since radiative cooling increases rapidly as the mean temperature increases. However, the energy content of the heating radiation is low because of the great distance of Uranus from the sun. Consequently, even as inefficient a process as molecular diffusion is of comparable importance to the energy balance of the upper atmosphere, and we conclude that the atmospheric structure cannot be described adequately in terms of radiative equilibrium alone, regardless of the detailed properties of putative minor atmospheric constituents.

Other energy sources must be responsible for the observed temperature variations. What are the possibilities? The formation and growth of a thermal perturbation is possible only if the energy flux divergence is non-zero. Since molecular diffusion always attempts to create an isothermal state, a lower limit to the required energy is that the energy flux divergence exceed that due to diffusion. The corresponding heating rate must be at least as large as that due to molecular diffusion, typically 1-10K yr^{-1} in the occultation region (cf. Table VI). In other words, any energy source large enough to overcome the effects of molecular diffusion and produce the observed thermal structure must also be large enough to influence significantly the basic state temperature of the upper atmosphere. Thus, although molecular diffusion has little direct effect on the basic thermal state in a radiative equilibrium model, the diffusion flux divergence implied by the observed temperature gradients gives a measure of the energy fluxes important to the thermal balance, and these are at least as important as radiative energy sources. Under these circumstances, it is not surprising that the observed mean temperature does not match the precise predictions of radiative equilibrium, nor that the mean atmospheric temperature is observed to change so quickly (Fig. 8).

Heating by turbulent energy can be significant if the eddy viscosity is sufficiently large and if there is a localized source of energy to feed the eddies. Such a region could be produced by shear instabilities or by dissipation of vertically propagating waves, for example. The overall structure in Fig. 7 cannot be an inertia-gravity wave, because Dunham et al. (1980) have shown that such a mode would have an enormous energy flux. However, there are many small-scale features in Fig. 7. These features extend for at least 144 km along the limb for the 15-16 August 1980 observations. If these are regarded as inertia-gravity waves, then the dispersion relation given in French and Gierasch (1974) can be used to estimate the associated energy flux. For example, assuming a vertical wavelength, λ_v, of 6 km, a horizontal wavelength of 144 km, and a temperature perturbation of 0.5 K, at $n = 10^{15}$ cm^{-3}, the corresponding energy flux is $F_w = 0.024$ erg cm^{-2} s^{-1}, and the associated heating rate is $(dT/dr)_w \sim 1$ K yr^{-1}. Such short vertical wavelength modes cannot propagate when the molecular or eddy diffusivity exceeds a critical value, which for this example is 3×10^4 cm^2 s^{-1}. The waves then dissipate their energy and heat up the atmosphere.

This is an attractive possibility because it accounts for both the observed fine structure of the temperature profile and satisfies the energy requirements. The mechanism requires a low eddy viscosity ($K < 3 \times 10^4$ cm^2 s^{-1}) to permit waves generated deeper in the atmosphere to propagate into the occultation region without significant dissipation. (Such small values of K are not unheard of. For example, Tomasko (1974) determined that $K = 2 \times 10^4$ cm^{-2} s^{-1} in the Jovian stratosphere at pressures between 20 and 500 mbar.) Unfortunately, we have no information about the stratospheric eddy viscosity for Uranus, but it is conceivable that vertical mixing could be inhibited in the atmosphere of a planet which has no significnt internal heat source and which is so far from the sun. Stone (1973) shows that the troposphere of Uranus is expected to be remarkably stable, with very weak turbulence and a Richardson number in excess of 1000. Under such conditions, vertical mixing by eddies should be minimal. Alternatively, the temperature structure may reflect dissipation of turbulent energy resident in a stratospheric region of strong shear, but little further can be said in the absence of more information.

One of the intriguing aspects of Fig. 8 is the generally close agreement of immersion and emersion mean temperatures, compared to the larger variation in temperature with time. If these observations are representative, then they suggest that the atmospheric circulation is sufficiently strong to isothermalize the stratosphere, in spite of the large differences in diurnally averaged insolation (Fig. 9). Although radiative time constants are long in the occultation region, they are shorter deeper in the atmosphere, and a typical radiative relaxation time at the 2 mb level is seven days (Appleby, 1981, private communication). Consequently, the variations in <D> shown in Fig. 9 may be important drives to circulation at deeper levels which ultimately influences the upper atmospheric thermal structure on time scales shorter than the local radiative time constant. It is unclear what the global mean circulation is on a planet with a deep atmosphere whose poles receive more energy than the equator (Fig. 10), and even less clear how important these tropospheric dynamics are to the stratospheric structure. Stone (1975) suggests that the deeper layers where solar radiation is absorbed will have a moderating effect on the higher layers where the time constant is considerably shorter.

Many of these issues will remain unsettled until Voyager encounters Uranus in 1986, but some of them may be clarified considerably in early 1982, when three high quality atmospheric occultations of Uranus will be observed within six weeks (Klemola, Mink and Elliot, 1981). From these observations, we can learn whether the agreement between immersion and emersion temperatures persists, and can chart more accurately the secular changes in the mean atmospheric temperature. Multiple observations of each event will permit the horizontal scales of the temperature perturbations to be determined, allowing more precise identification of the possible dynamical modes they represent.

V. CONCLUSIONS

Observations of both the mean stratospheric temperature and the detailed thermal structure of Uranus' atmosphere reveal that non-radiative sources of energy are important to the heat balance, with heating rates of tens of K yr^{-1}. Radiative time constants are longer than the time scales over which significant changes in the mean stratospheric temperature have been observed. The possibility that the upper atmosphere is isothermalized over time scales shorter than a few months suggests that the general circulation may be very effective at meridional transport of energy at these levels. Under these circumstances, discussions of a constant amplitude temperature inversion of the upper atmosphere are simplistic, and ignore important, and perhaps dominant, non-radiative energy sources. The complexities of the picture can be sorted out only when more precise measurements of the abundances of radiatively important minor constituents such as C_2H_2 and C_2H_6 have been made, and when additional occultation observations confirm or deny the existence of the patterns presented by the observations available so far. At that time, it will be appropriate to construct more realistic atmospheric models which take proper account of these non-radiative effects, in order to determine the sensitivity of the thermal structure to changes in thermal and dynamical forcing.

ACKNOWLEDGMENTS

We would like to thank Philip Nicholson for providing us with the results of 1979 CLCO occultation prior to publication and John Appleby for very helpful discussions. We also thank Doug Mink and Martha Schaffer for performing preliminary calculations; we are grateful to Ramon Galvez, Daniel Maturana and Hugo Vargas for assistance with the observations at Cerro Tololo. This work was supported in part by NASA Grants NAGW-68 and NSG 7526 and NSF Grant AST-8010699.

References

Appleby, J.F. 1980. Ph.D. Thesis, State University of New York at Stony Brook.

Barton, J.R. and Allen, D.A. 1980. "An Integrating Preamplifier for Indium Antimonide Infrared Detectors", Pub. Astr. Soc. Pac. 92, 368-374.

Dunham, E., Elliot, J.L. and Gierasch, P.J. 1980. "The Upper Atmosphere of Uranus: Mean Temperature and Temperature Variations", Ap. J. 235, 274-284.

Elliot, J.L. and Dunham, E. 1979. "Temperature Structures of the Uranian Upper ATmosphere", Nature 279, 307-308.

Elliot, J., French, R.G., Frogel, J.A., Elias, J.H., Mink, D.J., Liller, W. 1981. "Orbits of Nine Uranian Rings", A.J. 86, 444-455.

French, R.G., Elliot, J.L. and Gierasch, P.J. 1978. "Analysis of Stellar Occultation Data", Icarus 33, 186-202.

French, R.G., Elliot, J.L., Sicardy, B., Nicholson, P., and Matthews, K. 1982. "The Upper Atmosphere of Uranus: A Critical Test of Isotropic Turbulence Models", Icarus (submitted).

French, R.G. and Gierasch, P.J. 1974. "Waves in the Jovian Upper Atmosphere", J. Atmos. Sci. 31, 1707-1712.

Frogel, J.A. and Elias, J.H. 1980. CTIO Facilities Manual, revised edition. (CTIO, La Serena, Chile).

Gillett, F.C. and Rieke, G.H. 1977. "5-20 Micron Observations of Uranus and Neptune", Ap.J. (Letters) 218, L141-L144.

Klemola, A.R. and Marsden, B.G. 1977. "Predicted Occultations by the Rings of Uranus, 1977-1980", A.J. 82, 849-851.

Klemola,A.R., Mink, D.J. and Elliot, J.L. 1981. "Predicted Occultations by Uranus: 1981-1984", A.J. 86, 138-140.

Nicholson, P., et al. In preparation.

Reif, F. 1965. Fundamentals of Statistical and Thermal Physics. (McGraw-Hill, Inc., New York).

Stone, P.H. 1975. "The Atmosphere of Uranus", Icarus 24, 292-298.

Strobel, D.F. and Smith, G.R. 1973. "On the Temperature of the Jovian Thermosphere", J. Atmos. Sci. 30, 718-725.

Tomasko, M.G. 1974. "Ammonia Absorption Relevant to the Albedo of Jupiter. II. Interpretation", Ap.J. 187, 641-650.

Veverka, J., Wasserman, L.H., Elliot, J.L., Sagan, C. and Liller, W. 1974a. "The Occultation of β-Scorpii by Jupiter: [illegible] The Structure of the Jovian Upper Atmosphere", A.J. 79, 73-84.

Veverka, J., Wasserman, L.H. and Sagan, C. 1974b. "On the Upper Atmosphere of Neptune", Ap.J. 189, 569-575.

Wallace, L. 1975. "On the Thermal Structure of Uranus", Icarus 25, 538-544.

Wallace, L. 1980. "The Structure of the Uranus Atmosphere", Icarus 43, 231-259.

Wasserman, L. 1974. "Diurnal Temperature Variations and the Methane Mixing Ratio in the Jovian Upper Atmosphere: Evidence From the Occultation of β-Scorpii by Jupiter", Icarus 22, 105-110.

TABLE I

Light Curve Properties and Occultation Timing

Date	Station	Event[a]	$v_\perp$(km-s^{-1})[b]	ε(s$^{1/2}$)	$\varepsilon(v_\perp/H)^{1/2}$[c]	$\langle \Delta\phi^2_u \rangle^{1/2}$	$t_{1/2}$(UT)
15 Aug 1980	CTIO	I	6.811	0.007	0.002	0.18	22:38:09.07
16 Aug 1980	CTIO	E	6.888	0.008	0.003	0.28	00:16:26.42
26 April 1981	ANU	I	15.248	0.123	0.058	0.18	19:33:07.80
	AAT	I	15.248	0.007	0.003	0.17	19:33:07:12
	AAT	E	15.196	(0.007)[d]	(0.003)	0.14	20:04:43.85

Notes

[a] I = Immersion, E = Emersion

[b] Event velocities computed for an assumed planetary ellipticity of 0.024.

[c] Scale height of 70 km assumed.

[d] ε for AAT emersion was assumed to be the same as for AAT immersion, since sunrise prevented an independent determination of ε from post-emersion data.

TABLE II

Mean Atmospheric Temperatures

Date	Station	Event[a]	$\bar{T}$(K) (Isothermal Fit)	T(K)[b] (Inversion)
15 August 1980	CTIO	I	151	156
16 August 1980	CTIO	E	156	c
26 April 1981	ANU	I	(121)[d]	(119)[d]
	AAT	I	129	138
	AAT	E	131	129

Notes

[a] I = immersion, E = emersion.

[b] The mean temperatures obtained from numerical inversion were averaged over an altitude interval of ~175 km, from 175 km, from 25 km above to 150 km below the half-light level. The midpoint of this range is near number density 3×10^{14} cm^{-3}.

[c] Inversion of this emersion event was not reliable because of clouds.

[d] These data are significantly noisier than the AAT observations. (cf. Table I).

TABLE III

Diurnally and Annually Averaged Insolation at the Observed Sub-Occultation Latitudes on Uranus

Date	Station	Event	Sub-Occultation Latitude on Uranus	<D>[†]	<A>[‡]
10 March 1977	KAO	I	4°.7	0.23	0.21
	KAO	E	-18.1	0.08	0.22
	CAPE	I	7.4	0.25	0.21
	CAPE	E	-20.8	0.06	0.23
10 June 1979	CLCO	I	26.2	0.39	0.24
	CLCO	E	-30.4	0.0[*]	0.25
15-16 August 1980	CTIO	I	-26.3	0.0[*]	0.24
	CTIO	E	17.9	0.30	0.22
26 April 1981	AAT	I	8.4	0.19	0.21
	AAT	E	-18.6	0.004	0.23

Notes

[†] <D> is the diurnally averaged insolation in units of the normal incidence solar constant at Uranus, for the observed sub-occultation latitude.

[*] The observed sub-occultation latitude was in darkness throughout a full rotation of the planet. See text for details.

[‡] <A> is the orbitally averaged insolation in units of the normal incidence solar constant at Uranus, for the observed sub-occultation latitude.

TABLE IV

Adopted Parameter Values

μm_H	3.7×10^{-24} g
c_p	1.17×10^{8} erg g^{-1} K^{-1}
γ	1.47
b (3.3 μm CH_4 band)	0.25 μm cm^{-1} am^{-1}
n_{CH_4}	3×10^{-5}
$n_{C_2H_2}$	2×10^{-8}
g	818 cm s^{-2}
$\sigma(H_2)$	6.9×10^{-16} cm^2
dT/dz	0.2 K km^{-1}
f_λ (at λ = 3.3 μm)	54.2 erg-cm^{-2} s^{-1} μm^{-1}
T	125 K

TABLE V

Radiative Cooling Rates and Relaxation Times*

T(K)	75		100		125		150		175	
n(cm^{-3})	CH_4: dT/dt(K-yr^{-1}) C_2H_2: dT/dt(K-yr^{-1})	τ(yr) τ(yr)	CH_4: dT/dt(K-yr^{-1}) C_2H_2: dT/dt(K-yr^{-1})	τ(yr) τ(yr)	CH_4: dT/dt(K-yr^{-1}) C_2H_2: dT/dt(K-yr^{-1})	τ(yr) τ(yr)	CH_4: dT/dt(K-yr^{-1}) C_2H_2: dT/dt(K-yr^{-1})	τ(yr) τ(yr)	CH_4: dT/dt(K-yr^{-1}) C_2H_2: dT/dt(K-yr^{-1})	τ(yr) τ(yr)
10^{12}	7.2×10^{-8} 7.8×10^{-5}	1.0×10^{9} 9.6×10^{5}	1.1×10^{-4} 3.0×10^{-3}	6.8×10^{5} 2.5×10^{4}	9.3×10^{-3} 2.7×10^{-2}	1.3×10^{4} 4.6×10^{3}	0.20 0.12	750 1.3×10^{3}	1.9 0.34	92 510
10^{13}	7.2×10^{-7} 5.8×10^{-4}	1.0×10^{8} 1.3×10^{5}	1.0×10^{-3} 2.2×10^{-2}	7.5×10^{4} 3.4×10^{3}	8.7×10^{-2} 0.19	1.4×10^{3} 660	1.8 0.82	83 180	16 2.4	11 73
10^{14}	6.4×10^{-6} 1.7×10^{-3}	1.2×10^{7} 4.4×10^{4}	7.9×10^{-3} 5.8×10^{-2}	9.5×10^{3} 1.3×10^{3}	0.57 0.48	220 260	9.3 2.0	16 75	66 5.4	2.7 32
10^{15}	3.4×10^{-5} 2.1×10^{-3}	2.2×10^{6} 3.6×10^{4}	2.5×10^{-2} 6.9×10^{-2}	3.0×10^{3} 1.1×10^{3}	1.2 0.56	104 220	16 2.3	9.4 65	96 6.2	1.8 28
10^{16}	6.0×10^{-5} 2.2×10^{-3}	1.3×10^{6} 3.4×10^{4}	3.3×10^{-2} 7.0×10^{-2}	2.3×10^{3} 1.1×10^{3}	1.4 0.58	89 220	17 2.4	8.8 63	100 6.4	1.8 27

* Computed for $\eta_{CH_4} = 3 \times 10^{-5}$ and $\eta_{C_2H_2} = 2 \times 10^{-8}$.

TABLE VI

Thermal Relaxation Times*

Process	$n(cm^{-3})$	$K(cm^2\ s^{-1})$	$dT/dt(K\ yr^{-1})$	$\tau(yr)$
Molecular Diffusion	10^{12}	--	360	0.45
	10^{13}	--	36	4.5
	10^{14}	--	3.6	45
	10^{15}	--	0.36	450
Eddy Diffusion	--	10^4	.38	330
	--	10^5	3.8	3.3
	--	10^6	380	0.33
	--	10^7	3.8×10^3	3.3×10^{-2}
	--	10^8	3.8×10^4	3.3×10^{-3}

* A temperature of 125K is assumed.

FIGURE CAPTIONS

Fig. 1. Immersion light curve of the 15-16 August 1980 occultation observed from CTIO. The light curve begins at 22:36:40.0 (UT) and is plotted at $0\overset{s}{.}2$ resolution. The best fitting isothermal light curve is also shown, corresponding to a temperature of 151K.

Fig. 2. Emersion light curve of the 15-16 August 1980 occultation observed from CTIO. The light curve begins at 00:12:30.0 (UT) 16 August 1980 and is plotted at $0\overset{s}{.}2$ resolution. The best fitting isothermal light curve is also shown, corresponding to a temperature of 156K. The strong undulations at the end of the plotted data were caused by clouds.

Fig. 3. Immersion light curve of the 26 April 1981 occultation observed from AAT. The light curve begins at 19:31:44.4 (UT) and is plotted at $0\overset{s}{.}3$ resolution. The best fitting isothermal light curve is also shown, corresponding to a temperature of 129K.

Fig. 4. Emersion light curve of the 26 April 1981 occultation observed from the AAT. The light curve begins at 20:00:29.4 (UT) and is plotted at $0\overset{s}{.}3$ resolution. The best fitting isothermal light curve is also shown, corresponding to a temperature of 131K.

Fig. 5. Immersion light curve of the 26 April 1981 occultation observed from ANU. The light curve begins at

ORIGINAL PAGE IS
OF POOR QUALITY

19:31:44 (UT) and is plotted at 1^s resolution. The best fitting isothermal light curve is also shown, corresponding to a temperature of 121K. The data are considerably noisier than those shown in Fig. 4 because a smaller telescope was used, and the observations were not carried out in the 2.2 μm methane band.

Fig. 6. Occultation Geometry. The tracks of the 15 August 1980 and 26 April 1981 events are shown for CTIO and AAT, respectively. The labelled dots indicate the location of the Uranus north pole for the two occultations. The immersion and emersion 1980 events probed latitudes -26° and +18°, respectively, on Uranus. The immersion and emersion latitudes for the 1981 events are +8° and -19°, respectively.

Fig. 7. Temperature profiles of the Uranian stratosphere obtained by numerical inversion of the light curves in Figs. 2, 4 and 5. The profiles are aligned in altitude at the point corresponding to the half-light time obtained from an isothermal fit to the data. This corresponds roughly to a number density of 3×10^{14} cm^{-3} and a pressure of 6 μb. Because of the uncertainties in the initial condition and the choice of baselines used for the inversion, the overall placement of the temperature profiles are uncertain by about 15K.

Fig. 8. Occultation determinations of mean upper atmospheric temperatures for Uranus. The circles mark the temperatures obtained from isothermal fits to the

occultation light curves obtained on the following dates: 10 March 1977 from the Kuiper Airborne Observatory, 10 June 1979 from Cerro Las Campanas Observatory, 15-16 August from CTIO, and 28 April 1981 from the AAT. The squares mark the mean temperatures obtained from numerical inversion of the same data. Open symbols correspond to immersion and closed symbols correspond to emersion events. The variations in mean temperature with time are generally larger than the variations in temperature with location in the planet (immersion and emersion) for a given occultation. Typical uncertainties in mean temperatures are of order ±15K. This estimate takes into account differences resulting from independent analysis of the same observations by different investigators, as well as station-to-station variations for multiply observed events.

Fig. 9. Diurnally averaged insolation on Uranus, as a function of latitude, for the dates of the observed atmosphere occultation. The ordinate is in units of the normal incidence solar constant at Uranus. The large dots correspond to the Uranus latitudes probed for each date.

Fig. 10. Orbitally averaged insolation on Uranus for one Uranian year, as a function of latitude. A circular orbit was assumed. The ordinate is in units of the normal incidence solar constant at Uranus. The polar regions receive, on average, more solar energy per orbit

than the equatorial regions.

Fig. 11. Cooling rates for emmission in the 7.7 μm CH_4 band, as a function of total atmospheric number density and temperature. The assumed CH_4 mixing ratio is $\eta_{CH_4} = 3 \times 10^{-5}$.

Fig. 12. Cooling rates for emission in the 13.7 μm C_2H_2 band, as a function of total atmospheric number density and temperature. The assumed C_2H_2 mixing ratio is $\eta_{C_2H_2} = 2 \times 10^{-8}$.

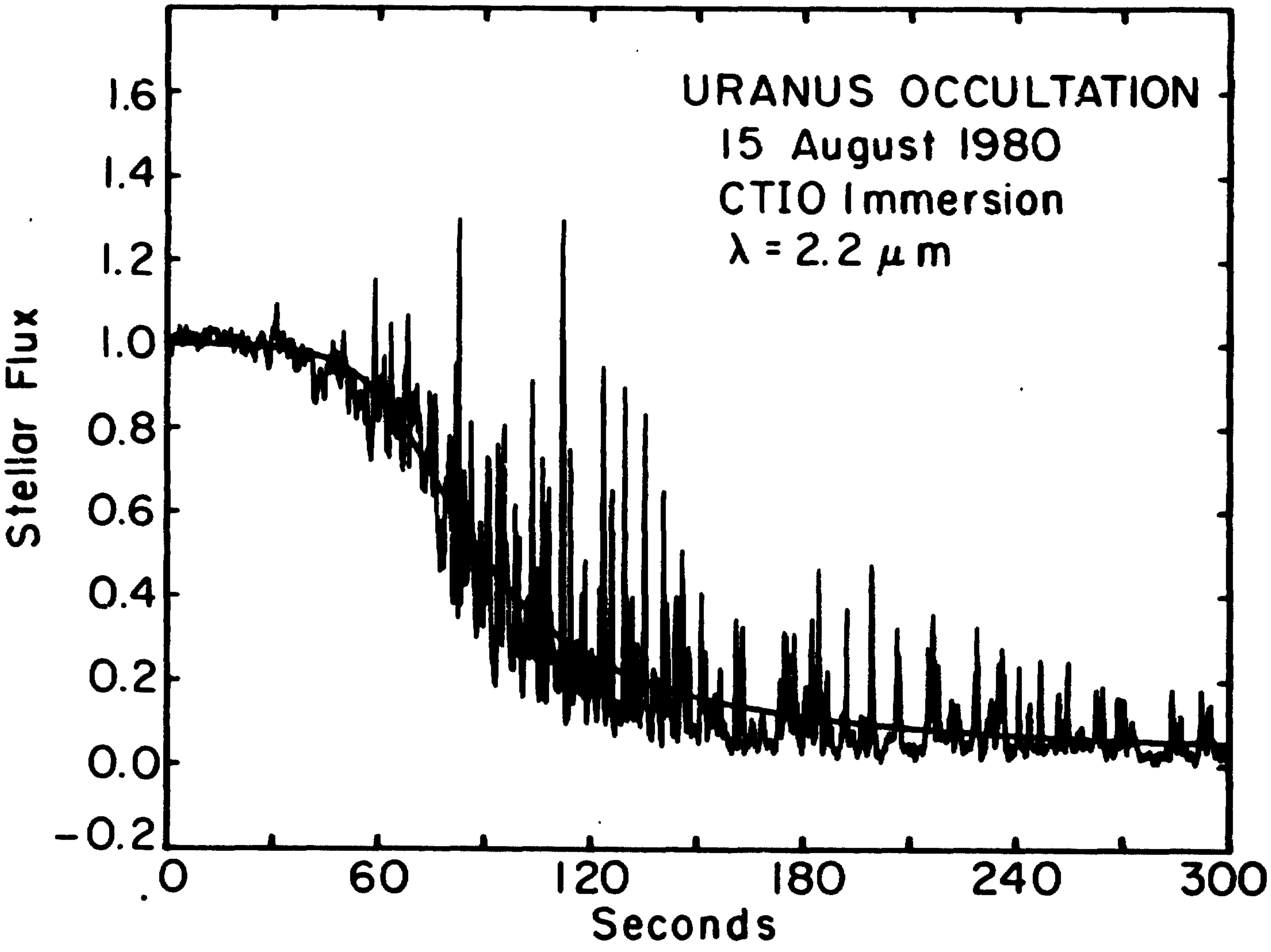
URANUS OCCULTATION
15 August 1980
CTIO Immersion
λ = 2.2 μm
Stellar Flux
1.6
1.4
1.2
1.0
0.8
0.6
0.4
0.2
0.0
−0.2
0
60
120
180
240
300
Seconds

Fig. 1

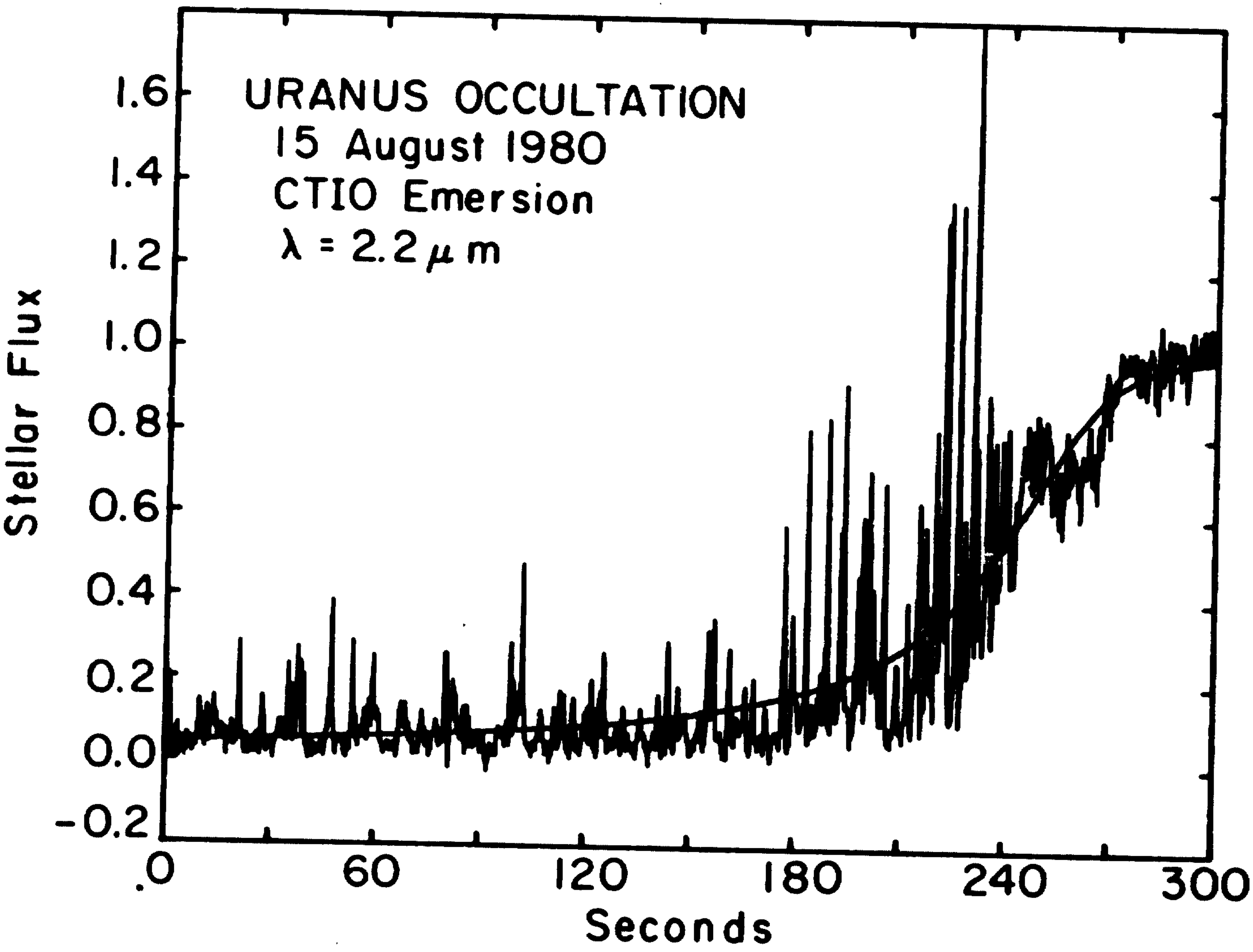
URANUS OCCULTATION
15 August 1980
CTIO Emersion
$\lambda = 2.2\,\mu m$
Stellar Flux
1.6
1.4
1.2
1.0
0.8
0.6
0.4
0.2
0.0
-0.2
.0
60
120
180
240
300
Seconds

Fig. 2

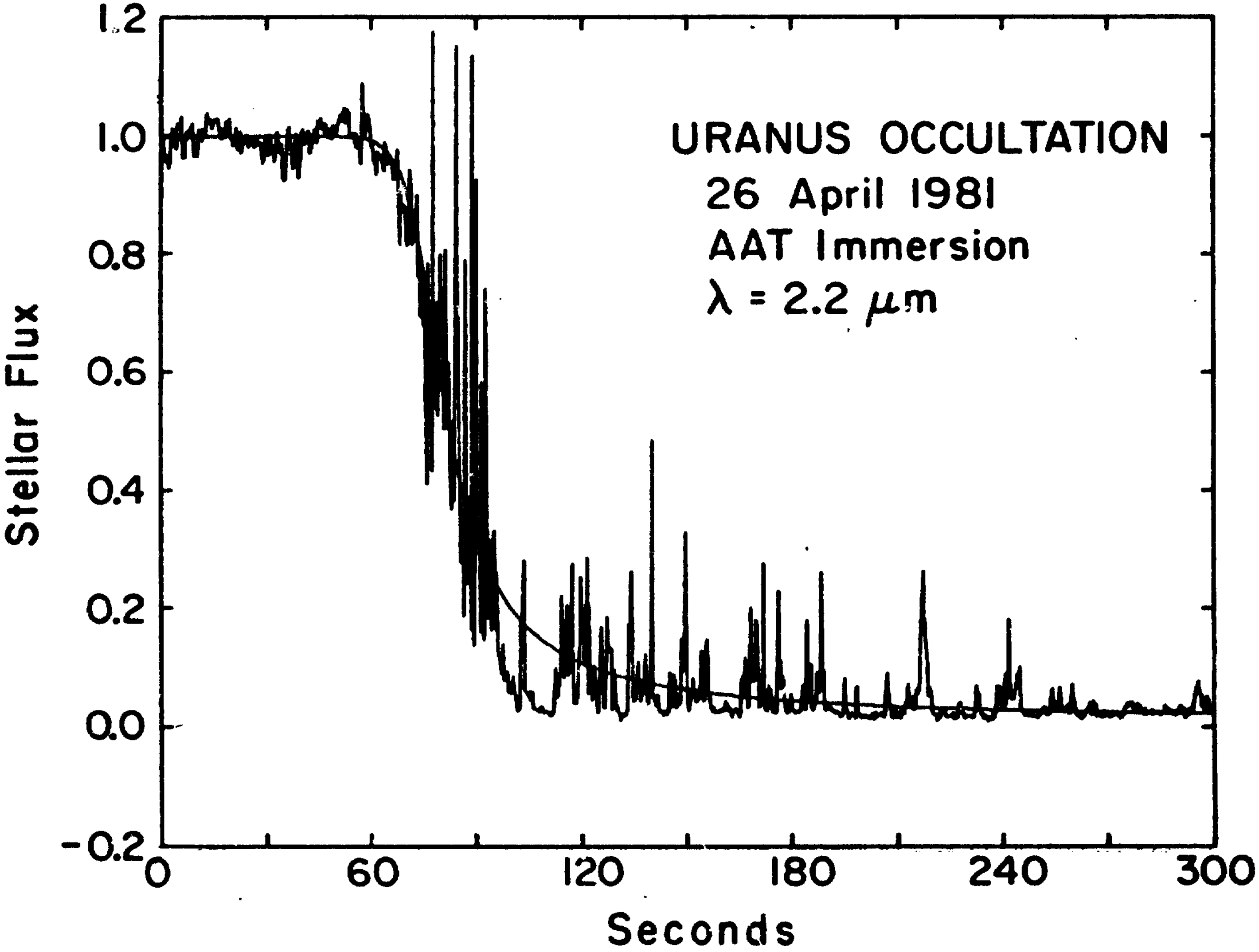
URANUS OCCULTATION
26 April 1981
AAT Immersion
λ = 2.2 μm
Stellar Flux
1.2
1.0
0.8
0.6
0.4
0.2
0.0
-0.2
0
60
120
180
240
300
Seconds

Fig. 3

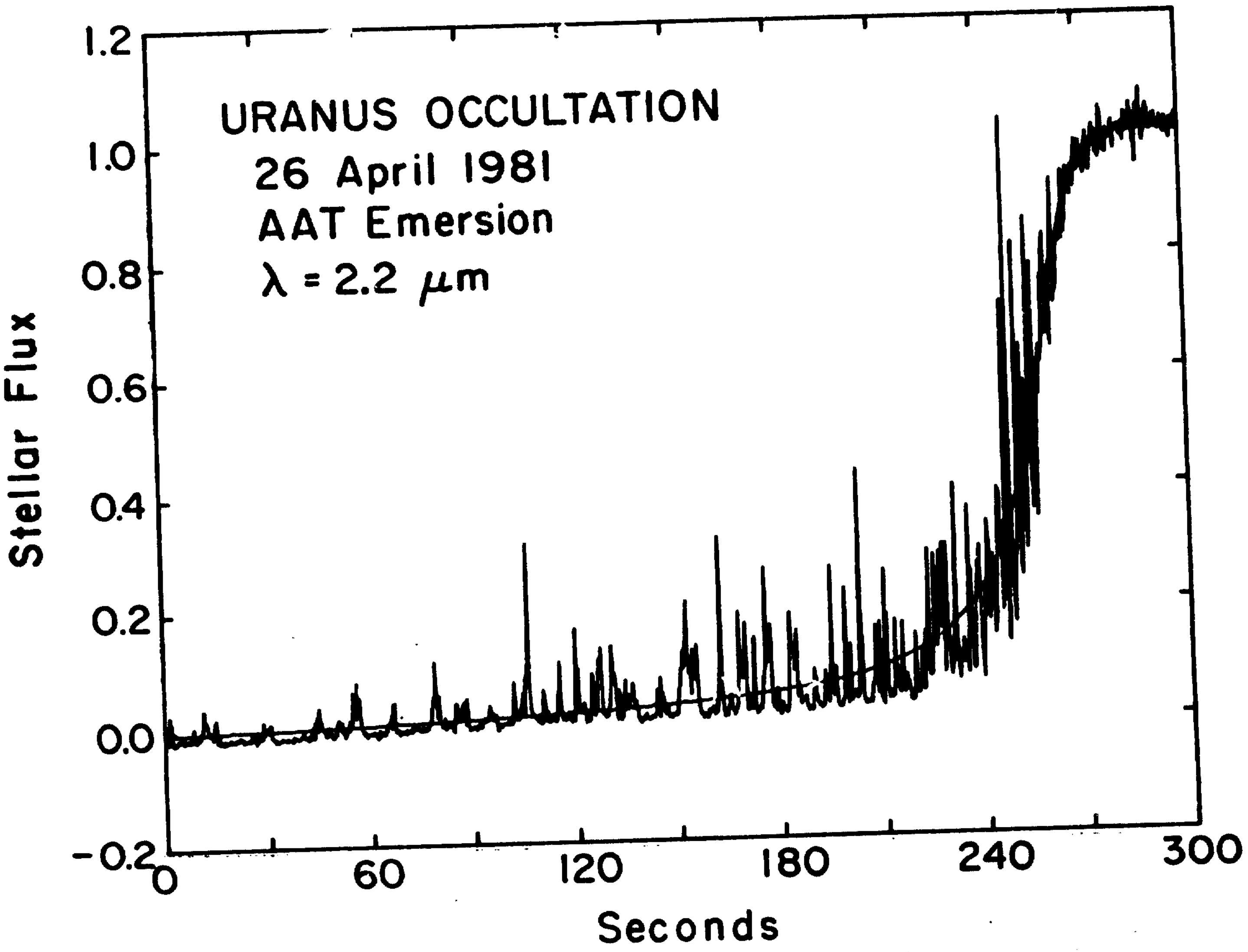
URANUS OCCULTATION
26 April 1981
AAT Emersion
λ = 2.2 μm
Stellar Flux
1.2
1.0
0.8
0.6
0.4
0.2
0.0
-0.2
0
60
120
180
240
300
Seconds

Fig. 4

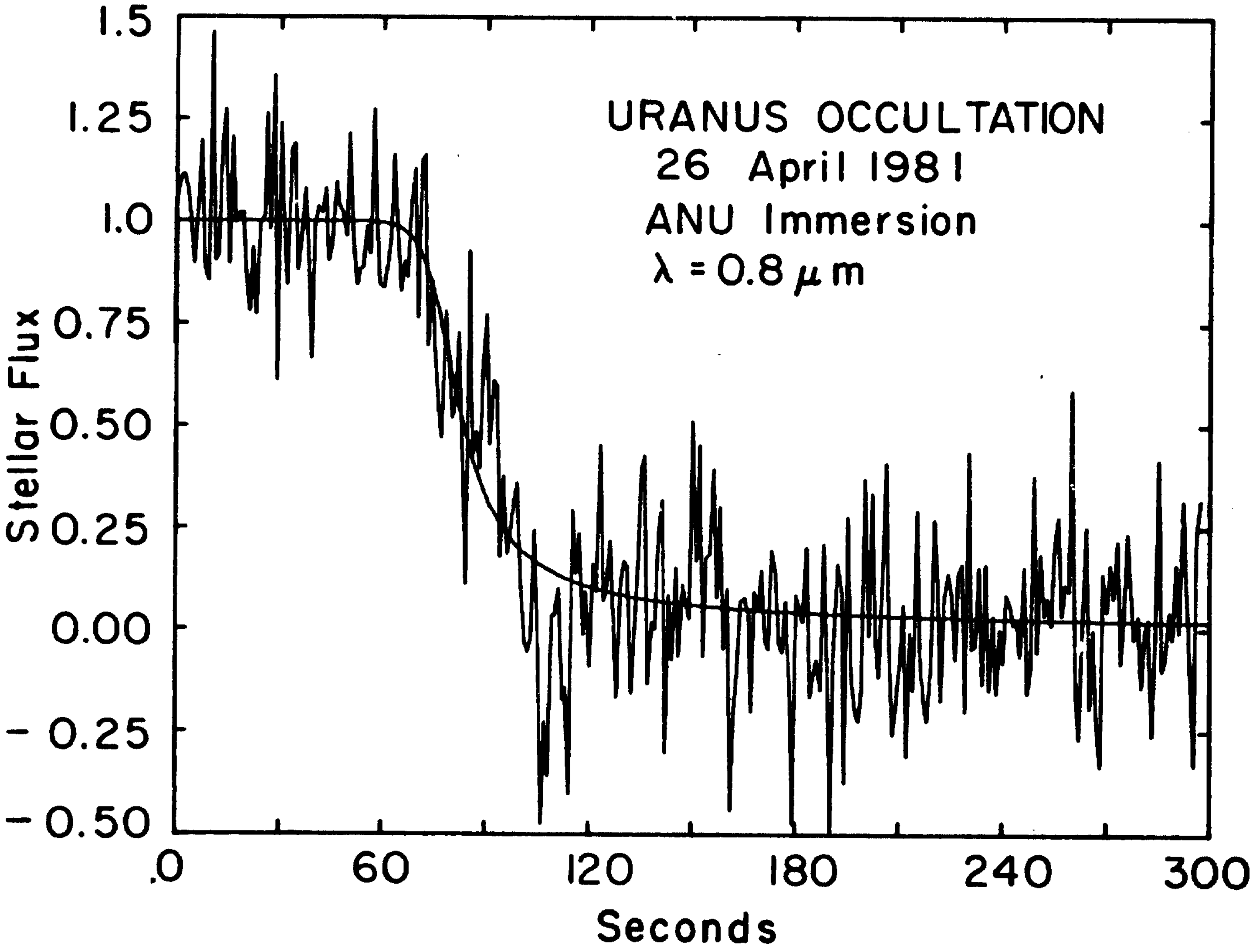
URANUS OCCULTATION
26 April 1981
ANU Immersion
λ = 0.8 μm
Stellar Flux
1.5
1.25
1.0
0.75
0.50
0.25
0.00
– 0.25
– 0.50
.0
60
120
180
240
300
Seconds

Fig. 5

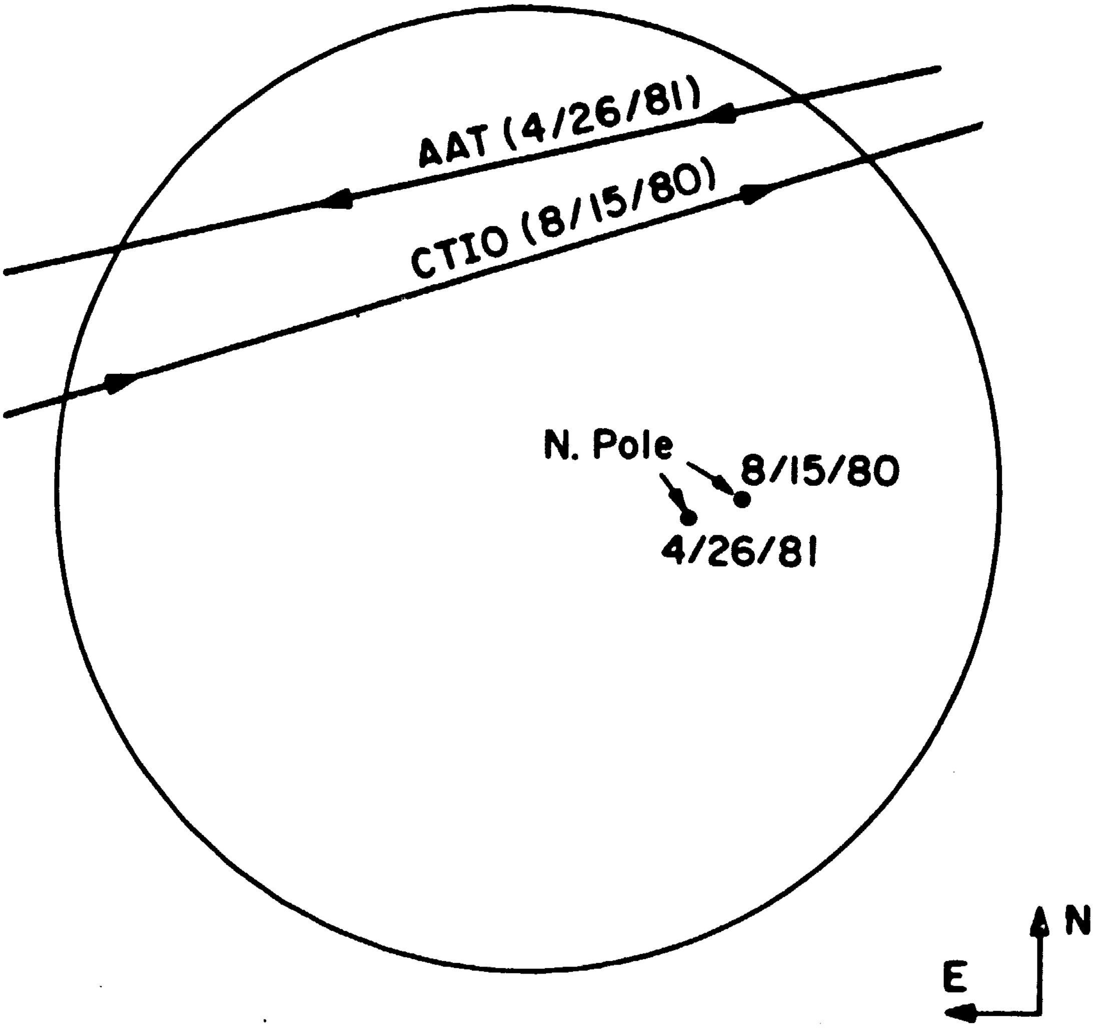

OCCULTATION GEOMETRY

Fig. 6

ORIGINAL PAGE IS
OF POOR QUALITY

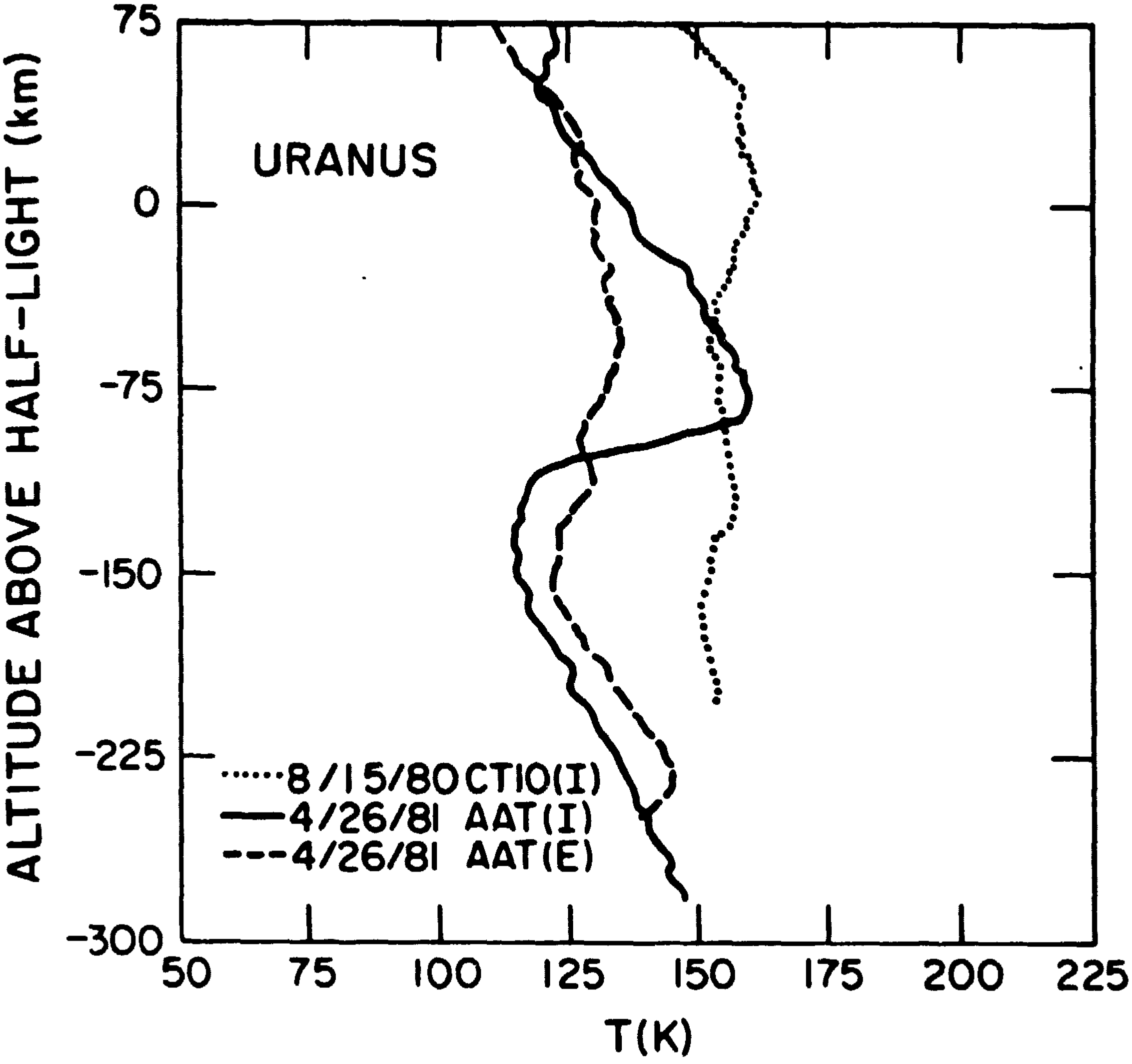

Fig. 7

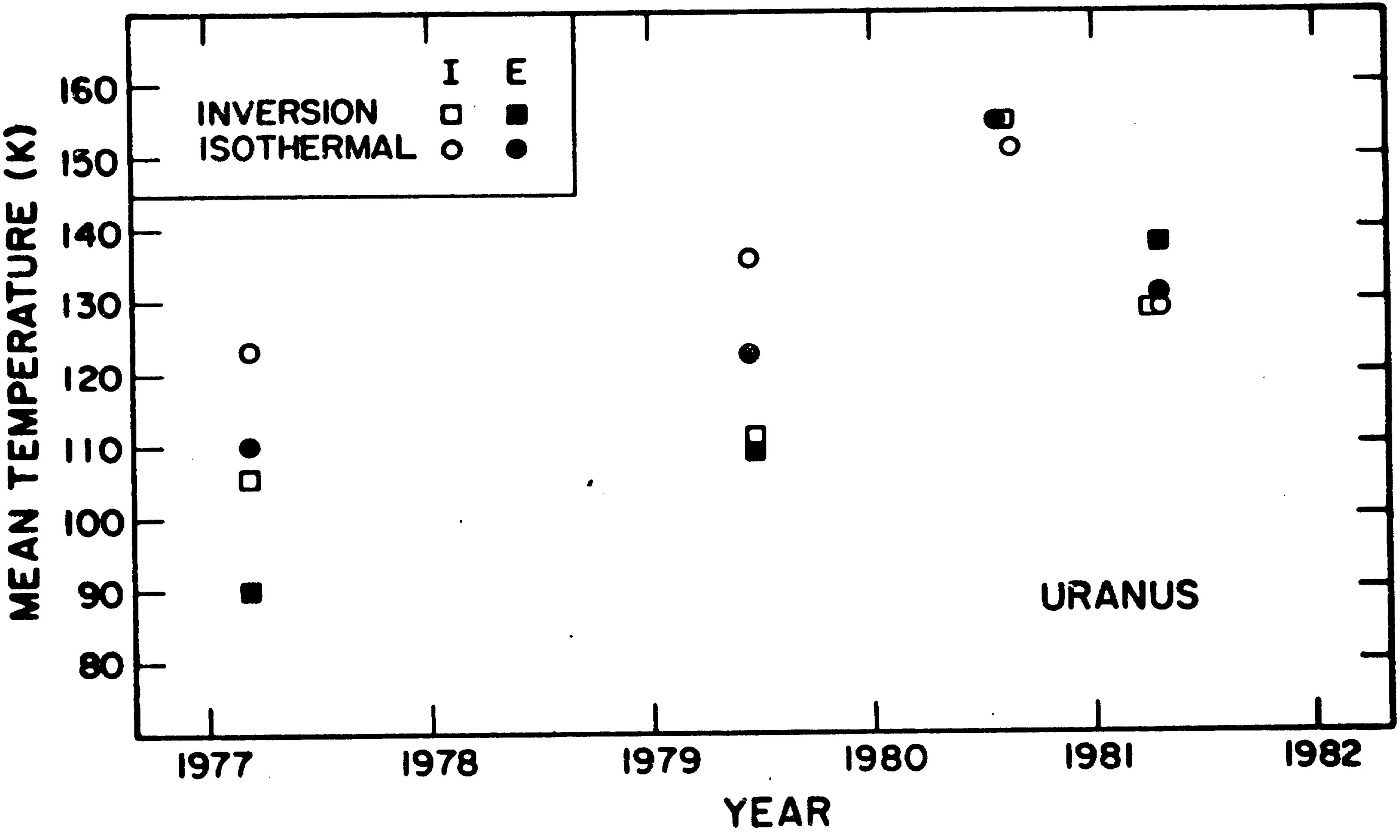
MEAN TEMPERATURE (K)
160
150
140
130
120
110
100
90
80
YEAR
1977
1978
1979
1980
1981
1982
I
E
INVERSION □ ■
ISOTHERMAL ○ ●
URANUS

Fig. 8

ORIGINAL PAGE IS
OF POOR QUALITY

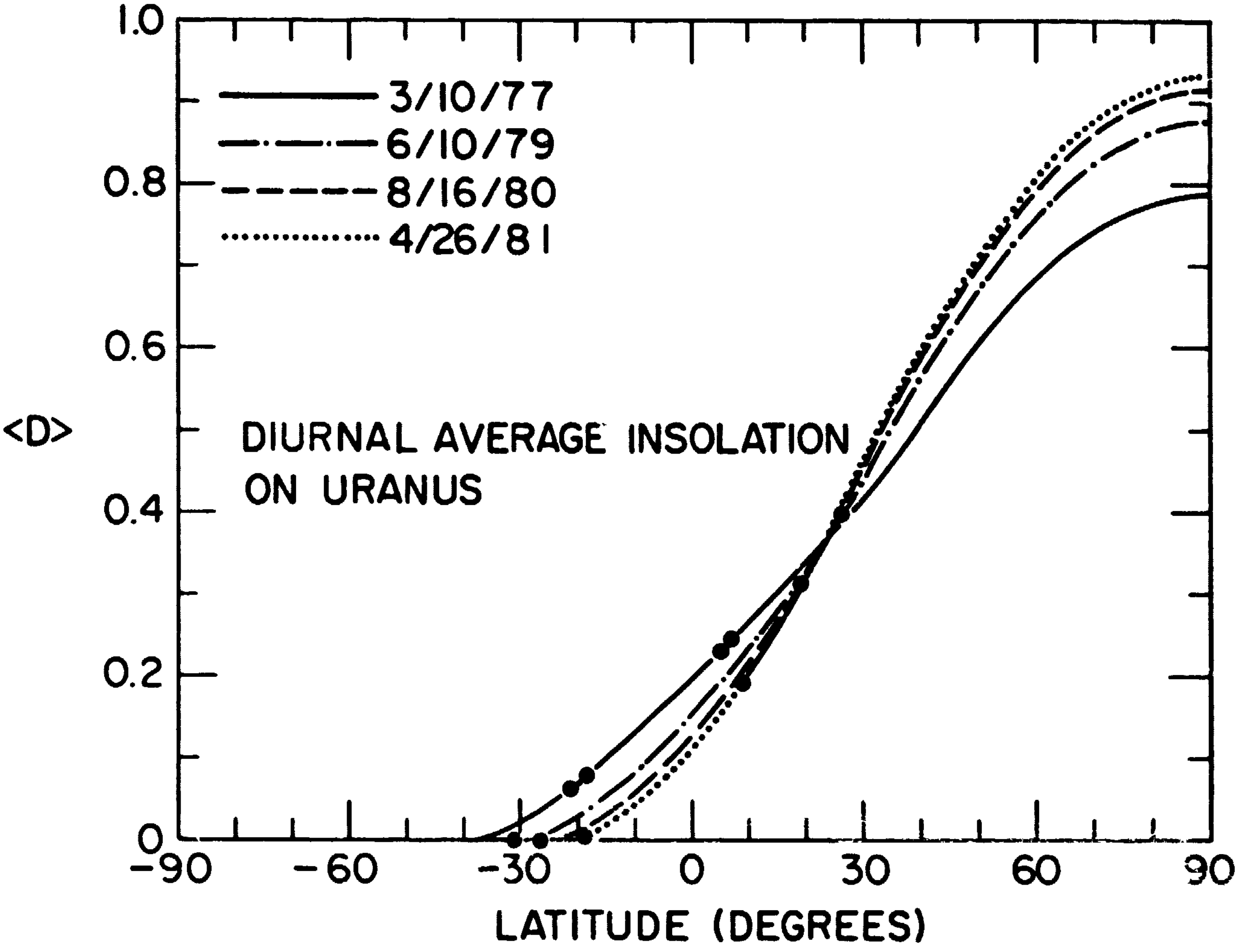

Fig. 9

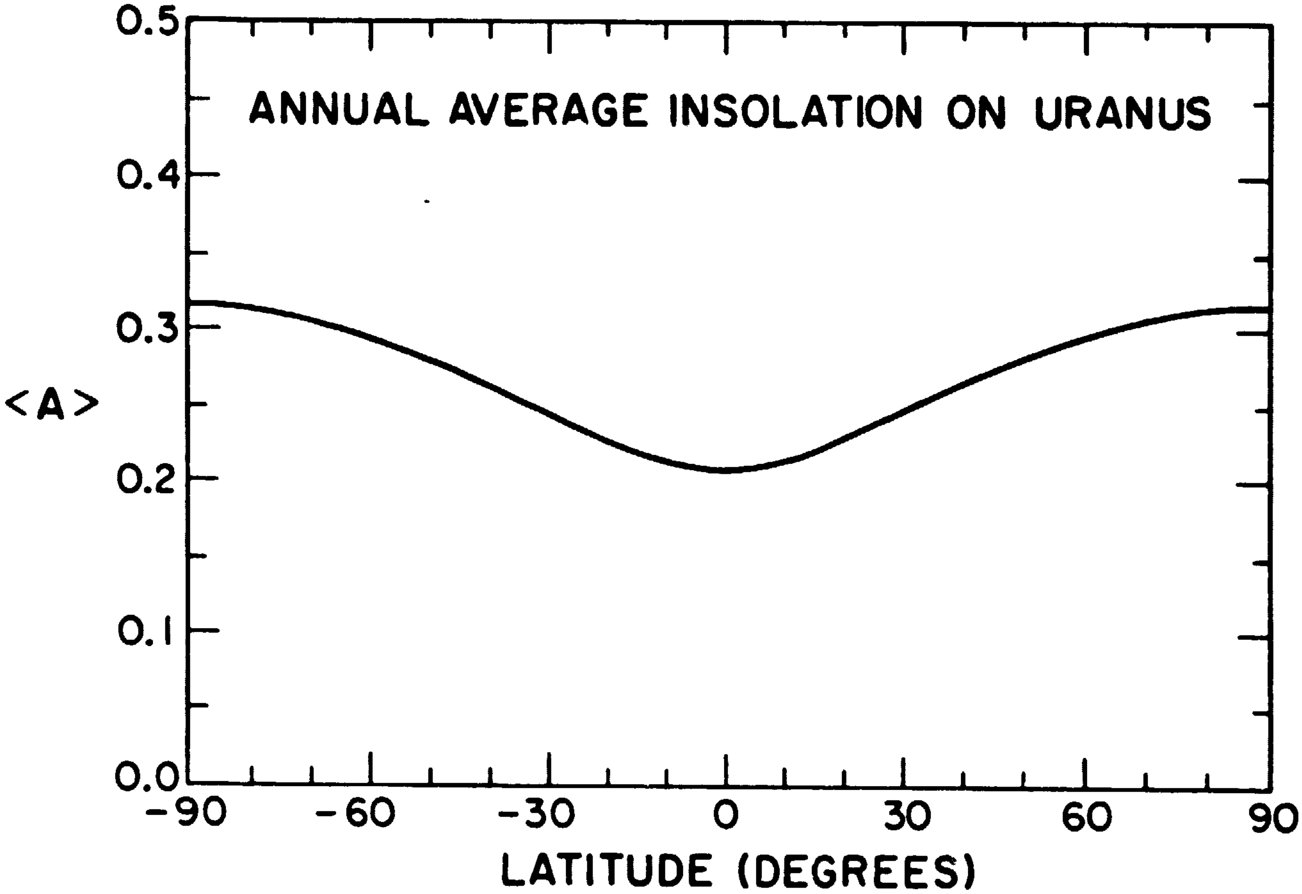
ANNUAL AVERAGE INSOLATION ON URANUS
<A>
0.5
0.4
0.3
0.2
0.1
0.0
-90
-60
-30
0
30
60
90
LATITUDE (DEGREES)

Fig. 10

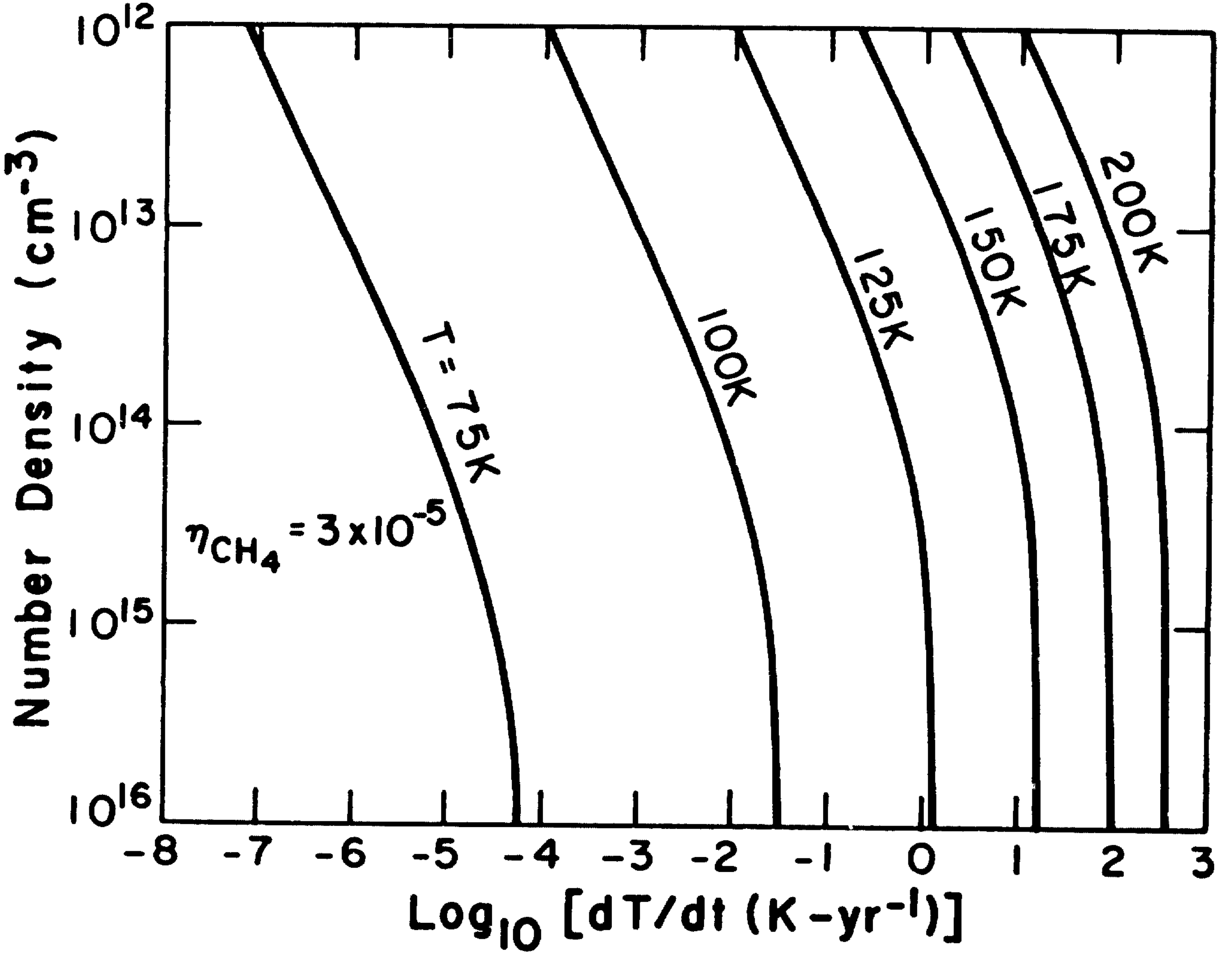
10^{12}
10^{13}
10^{14}
10^{15}
10^{16}
Number Density (cm^{-3})
-8
-7
-6
-5
-4
-3
-2
-1
0
1
2
3
Log_{10} [dT/dt (K-yr^{-1})]
T = 75K
100K
125K
150K
175K
200K
$\eta_{CH_4} = 3 \times 10^{-5}$

Fig. 11

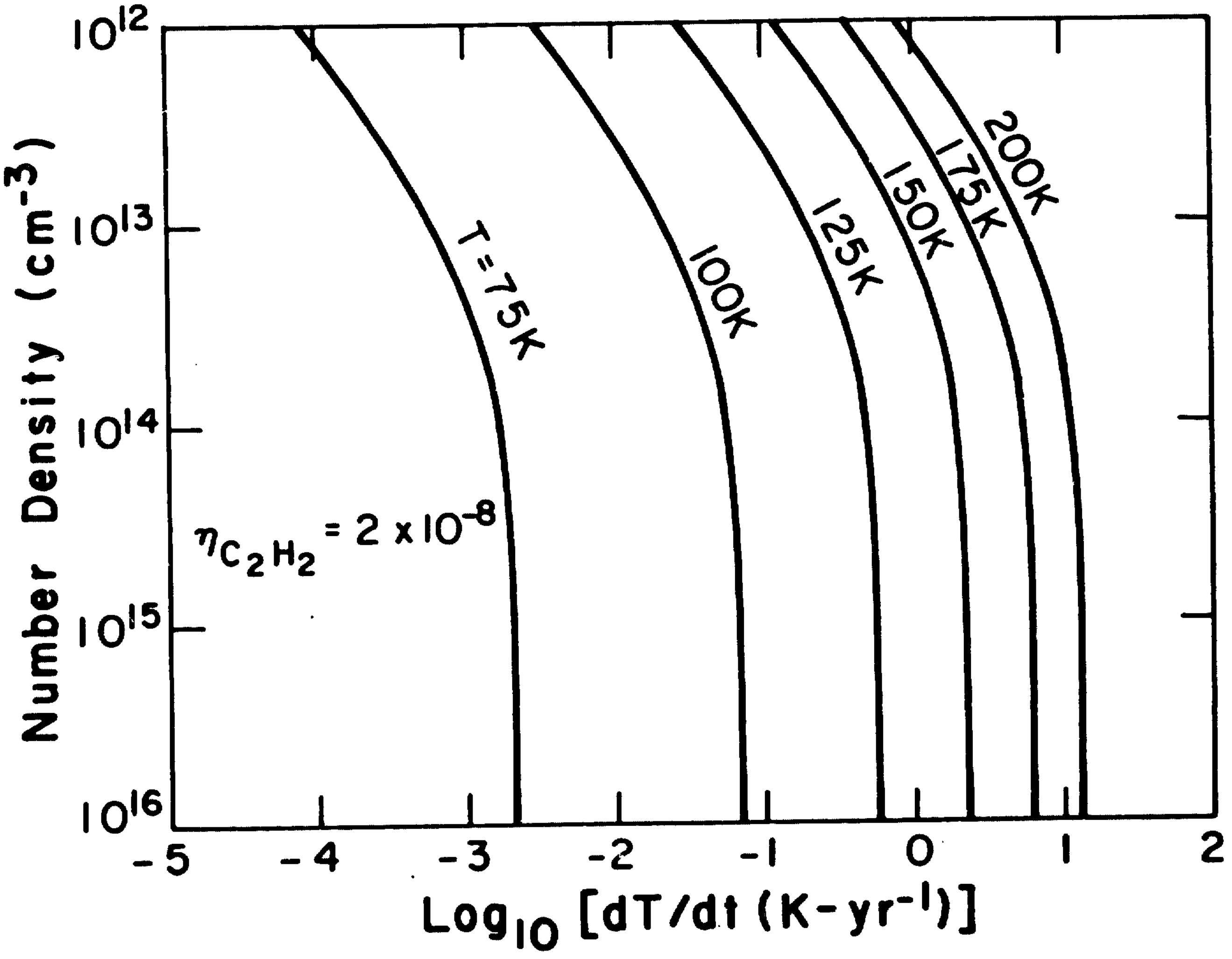
Number Density (cm^{-3})
10^{12}
10^{13}
10^{14}
10^{15}
10^{16}
-5
-4
-3
-2
-1
0
1
2
Log$_{10}$ [dT/dt (K-yr^{-1})]
T=75K
100K
125K
150K
175K
200K
$\eta_{C_2H_2} = 2 \times 10^{-8}$

Fig. 12

APPENDIX D

STRONG TURBULENCE AND ATMOSPHERIC WAVES IN STELLAR OCCULTATIONS

STRONG TURBULENCE AND ATMOSPHERIC WAVES IN STELLAR OCCULTATIONS

by

Richard G. French

Department of Earth and Planetary Science
Massachusetts Institute of Technology
Cambridge, Massachusetts 02139

and

Department of Astronomy
Wellesley College
Wellesley, Massachusetts 02181

and

Richard V.E. Lovelace

Department of Applied Physics
Cornell University
Ithaca, New York 14853

2 July 1982

I. Introduction

Stellar occultations are sensitive probes of distant planetary atmospheres, and in some cases, provide the only information we have about the structure of these remote upper atmospheres. Unfortunately, it has not proven easy to extract definitive results from the observations. The spiky structure of the light curves has been variously interpreted as scintillation due to isotropic turbulence (Jokipii and Hubbard, 1977; Texas-Arizona Occultation Group, 1977; Hubbard, 1979a) and as evidence for layered atmospheric structure (Kovalevsky and Link, 1969; French and Elliot, 1979; French et al., 1982b). A large (and occasionally acrimonious) body of literature has been generated by champions of each view, but there has been little common ground for discussion. Proponents of turbulent scintillation argue that the assumption that the atmosphere is perfectly layered is naive and unrealistic, while their critics contend that the assumptions of weak scintillation theory are violated by the very observations the theory is used to explain.

A new approach is called for: the investigation of the properties of light curves for atmospheres with more realistic properties than those considered so far. In §II we relax the restrictions of weak scintillation theory and construct model light curves for atmospheres with strong, anisotropic turbulence using wave optics. We compare the results with available weak scintillation theory and with recent occultation data. Then, in §III, we examine the effects of large-scale atmospheric waves with realistic horizontal structure. We assess the reliability of the numerical inversion method in retrieving the true atmospheric vertical structure under circumstances of strong ray crossing and horizontal inhomogeneities. Next, we compare the nature of model light curve spikes generated using geometric optics and wave optics. In the last section, we present our conclusions and indicate fruitful areas for further work. In an appendix, we provide a list of definitions of the symbols employed in this paper.

II. Strong Scintillation in Stellar Occultations

The most striking feature of typical stellar occultation light curves is the presence of numerous sharp and intense spikes, produced by non-isothermal structure in the planetary atmosphere. Young (1976) first articulated the view that spikes were the manifestation of turbulence, and subsequently the theory of turbulent occultations has been well developed by Hubbard, Jokipii, and Wilkening (1978, henceforth referred to as HJW), and by Haugstad (1978a,b,c and 1979). and Eshleman and Haugstad (1979). [Although there has been a long-standing debate between these two groups concerning certain details of the theory, (Hubbard, 1979; Eshleman and Haugstad, 1979, and references cited therein) these differences are not important for the present discussion.] Woo _et_ _al_. (1975, 1980b) have developed an analogous theory for radio occultations.

These authors restrict their treatment to weak scintillation, because the more general case is analytically intractable. This is a serious limitation, since the observed rms spike amplitude is not small compared to the mean intensity in most occultations, contrary to the fundamental assumption of weak scintillation theory. In this section, we investigate the properties of strong scintillation in stellar occultations by generating model light curves for strongly turbulent atmospheres. We confirm the results of weak scintillation theory, and summarize the qualitative differences apparent as the turbulence strength in increased. Finally, we discuss the applicability of these results to actual occultation observations.

A. Thin Screen Model

The general problem of stellar occultation theory is to relate the refractive properties of a planetary atmosphere to the characteristic features of the corresponding light curve. The occultation geometry is shown in Fig. 1, where an incident plane wave from a star is distorted by the planetary atmosphere on its path toward the earth. The effect of the atmosphere can be represented by a thin phase-changing screen which changes the phase of the incident plane wave but not its amplitude. The thin screen approximation is well satisfied for stellar occultations, as HJW demonstrate in some detail.

We adopt the coordinate system showwon in Fig 1. The star is considered to be monochromatic with vacuum wavelength λ. Let $\Phi(x,y)$ represent the phase delay suffered by the emergent ray passing through the point x,y in a reference plane perpendicular to the line of sight. In the absence of the planet's atmosphere we would have $\Phi = 0$. Thus:

$$\Phi(x,y) = \int_{-\infty}^{\infty} dz \ \nu(x,y) \tag{1}$$

where ν is the atmospheric refractivity. The lateral deflection of the ray is negligible within the atmosphere.

The atmosphere is assumed to be such that the refractivity can be decomposed as

$$\nu = \nu_A(r) + \nu_t(x,y,z) \tag{2}$$

where ν_A is the refractivity of the average atmosphere (with r the distance from the center of the planet), and where ν_t is the variation of the refractivity from its average value. The variations may represent turbulence, density waves, or other phenomena in the atmosphere. For the consideration of turbulence, we adopt an isothermal average atmosphere:

$$\nu_A(r) = \nu_o \exp[-(r-r_o)/H] \tag{3}$$

where r_o is a reference altitude, ν_o is the refractivity at this level, and H is the atmospheric scale height. Letting r_o be the altitude corresponding to the half-intensity point of the average light curve, we have the half-light refractivity

$$\nu_o = \frac{H^{3/2}}{(2\pi R)^{1/2} D} \tag{4}$$

where R is the planetary radius and D is the distance from the earth to the planet.

Furthermore, we assume that the rms turbulent refractivity is proportional to the local mean refractivity throughout the atmosphere:

$$\langle \nu_t{}^2 \rangle^{1/2} \propto \nu_A \tag{5}$$

It follows from the decomposition of Eq. 2 that one has from Eq. 1:

$$\Phi = \Phi_A + \Phi_t \tag{6}$$

where Φ_A is the phase shift due to the average atmosphere, and Φ_t that due to the variations. For the "half-intensity" ray, $\Phi_A \sim 2\pi(H/r_f)^2$, where the Fresnel scale is given by $r_f = (\lambda D)^{1/2}$. Generally, the point source wave amplitude at the reference screen is simply

$$E_s(x,y) = \exp(i\Phi_A + i\Phi_t) \tag{7}$$

The Fresnel small-angle approximation to the wave propagator is applicable, and, therefore, the point source wave amplitude at the earth is given by

$$E(x,y) = \frac{1}{r_f{}^2} \iint_{-\infty}^{\infty} dx'dy'E_s(x',y') \exp\left\{\frac{i\pi}{r_f{}^2}\left[(x-x')^2 + (y-y')^2\right]\right\} \tag{8}$$

The wave intensity at the earth is

$$I(x,y) = |E(x,y)|^2 \tag{9}$$

For a finite angular size source or star, in which different parts of its surface radiate incoherently, the intensity at the earth is given by

$$I_{fs}(x,y) = \iint d\theta_x d\theta_y S(\theta_x, \theta_y) I(x-\theta_x D,\ y-\theta_y D) \tag{10}$$

where $S(\theta_x, \theta_y)$ is the brightness distribution of the star and θ is a measure of subtended angle as viewed from the earth. We have in mind the common situation where the star is small in the sense that $d_* = \theta_* D << H$, where θ_* is the star's angular diameter.

Our approach is to evaluate Eqs. 8-10 numerically to produce simulated light waves for cases of interest, and to determine the statistical properties of the fluctuations. The basic properties of the resultant curves are governed by the non-dimensional scale factors $\hat{H} = H/r_f$ and $\hat{d}* = d*/r_f$, and by the nature and strength of the turbulence field. Representative scale factors for recent stellar occultations are given in Table I.

The central idea behind the simulations is that Eqs. 8 and 10 are of the form of convolutions, so that the fast Fourier transforms (FFTs) of these equations become simple products of the FFTs of the separate factors. In practice, the light curve is computed in overlapping pieces which are appropriately scaled and fitted together. Fig. 1 shows schematically how two adjacent portions of the light curve, A and B, are computed from overlapping segments of the upstream phase screen. Care is taken to insure that there is no aliasing during the computation, and the coordinates are scaled by the effective Fresnel scale in such a way that there is no loss of precision deep in the occultation where Φ_A becomes very large.

Once the point source light curve has been obtained, the influence of the finite source is taken into account by convolving the light curve with the intensity distribution of a uniform stellar disk. Again, this is accomplished with FFT's and application of the convolution theorem.

B. Anisotropic Kolmogorov Turbulence

An aspect of Eqs. 7-10 which is poorly known is the characterization of the refractivity variations ν_t, or the phase variations Φ_t, on the reference plane. The fact that observed light curves of finite size stars have prominent spikes provides a broad constraint on the nature of Φ_t. Furthermore, there is evidence, in some cases, of substantial anisotropy of whatever atmospheric structures are producing the spikes. As early as 1969, Kovalevsky and Link proposed that the spikes in Neptune occultation light curves were caused by layered structure rather than by turbulent scintillation. More recent Uranus observations have provided unequivocal evidence of homogeneous fine scale horizontal structure extending for hundreds of km along the planetary limb (French *et al.*, 1982b). Woo *et al* (1980a) concluded that the turbules in the atmosphere of Venus have characteristic aspect ratios of 20 or more. Terrestrial observations are consistent with Kolmogorov turbulence for horizontal scales of up to a dozen km (Armand *et al.*, 1975).

These observations provide the motivation for investigating in some detail the nature of strong scintillations produced by anisotropic turbulence. As an extreme case of such models, we will consider perfectly layered Kolmogorov turbulence in which the refractivity varies only with radial distance from the planet's center, r. (We are interested for the moment in the characteristics of the resulting light curves, and will defer a discussion of the actual realization of such turbulence fields in real atmospheres.) Letting $P_\nu(q_x)$ be the wavenumber power spectrum of the refractivity fluctuations, with q_x as the vertical wavenumber, one can readily show that wavenumber spectrum of the phase on the reference screen is given by

$$P_S(q_x) = (2\pi)^3 \frac{R}{\lambda^2} \frac{P_\nu(q_x)}{|q_x|} \qquad (11)$$

(Questions for R.L.: Is this valid for the geometry in question ?)

For one-dimensional Kolmogorov turbulence, the refractivity fluctuations have the power spectrum

$$P_\nu(q_x) \propto (q_x{}^2 + 1/L_c{}^2)^{-xx} \leftarrow * \qquad (12)$$

where L_c is the outer scale of the turbulence, assumed to be equal to H.

(RL-Wh
should
the
expone
be for
this
case?)

Representative results are shown in Fig. 2 for point source light curves, ($\hat{d} = 0$) with one-dimensional Kolmogorov turbulence and $\hat{H} = 30$, a typical value for recent occultations (cf. Table I). The turbulence strength is defined by A, the rms phase shift in radians at the altitude corresponding to the half-light ray. Note that from Eqs. 3-5,

$$\left\langle \left(\frac{\nu_t}{\nu_A}\right)^2 \right\rangle^{1/2} = \frac{A}{2\pi} \frac{r_f}{H}^{\;2} \qquad (13)$$

and

$$\langle \nu_t{}^2 \rangle^{1/2} = \frac{A\ r_f{}^2 \exp[-(r-r_o/H]}{(2\pi)^{3/2}(RH)^{1/2}D} \qquad (14)$$

The curves in Fig. 3 range from A = 0.0, equivalent to an isothermal atmosphere, to A = 4.0, corresponding to very strong turbulence. In each case, the same random phase front was used, scaled by the turbulence amplitude, A, so that the modification of individual light curve features can be observed as A increases. The curves are characterized by many narrow, intense spikes.

The effects of convolution with a finite source are seen in Fig. 3, for cases of both weak ($A = 0.5$) and strong ($A = 4.0$) scintillation, and for stellar diameters of $d_* = 0$, 1, 2, 5 and 10 r_f. Even for very strong scintillation, the spikes are strongly suppressed by the stellar smearing. (Further remarks?)

Statistics of Spike Intensity

A statistical measure of the scintillation strength is given by $\langle(\Delta\phi)^2\rangle^{1/2}$, the rms deviation of the light curve from the mean, isothermal light curve. Weak scintillation corresponds to the case where the fractional intensity fluctuations at a given point in the light curve are small compared with unity. Equivalently, the modulation index, m, is small compared to unity. Here:

$$m = \left\langle\left(\frac{\Delta\phi}{\phi}\right)^2\right\rangle^{1/2} \qquad (15)$$

where ϕ is the intensity of the mean (isothermal) light curve. Fig. 4 displays the rms amplitude and the modulation index of the fluctuations in the light curves of Fig. 2. In each box, the triangles correspond to the computed values, averaged over a distance of 2.5 H along the light curve. (Adjacent points are separated by 0.5 H.) The solid curves correspond to the predictions of HJW [their Eqs. 36-39] for layered Kolmogorov turbulence, based on weak scintillation theory, and properly scaled for the appropriate turbulence amplitude, A. Notice carefully that the vertical axis scales differ from plot to plot. Also shown in each case is an isothermal light curve.

Several points are worth noting. There is excellent agreement between the HJW curves and the simulations for A = 0.25 and 0.50, but the agreement becomes poorer as the turbulence amplitude is increased. (The apparent systematic offset of the rms amplitude model curve and simulation results between ϕ = 0.9 and ϕ = 0.7 is due to the large (2.5 H) bin size employed to compute the average fluctuations, which biases the results where the light curve is steep.) Similar results were found using turbulence spectra generated from independent sets of random noise, providing assurance that the results in Fig. 4 are truly representative of anisotropic Kolmogorov turbulence.

As the turbulence amplitude increases, the modulation index saturates at unity. This result "has been more or less accepted as an empirical fact in the field of radio waves" (Rumsey, 1975), and has been demonstrated numerically for strong, isotropic turbulence in a homogeneous background (Marians, 1975). According to Fante (1980), "it is now generally accepted that in very strong turbulence, the normalized variance of the irradiance fluctuations approaches unity." This is the first demonstration of such saturation under stellar occultation conditions, with a strongly defocussing background atmosphere.

Single Frequency Autocorrelation Functions

Under conditions of weak scintillation, the width of typical spikes increases along the light curve. This is because the Fresnel radius scales as $\phi^{1/2}$ in the atmosphere (HJW) and adjacent rays diverge as ϕ^{-1}, with the result that the characteristic spike width increases as $\phi^{1/2}$. The autocorrelation function (ACF) of a light curve provides a measure of typical spike widths, and we computed ACF's of point source light curves for both weak ($A = 0.5$) and strong ($A = 4.0$) scintillation according to the relation:

$$C(i,j,\tau) = \frac{\int_{-t}^{t} \Delta\phi_i(t')\Delta\phi_j(\tau-t')dt'}{\int_{-t}^{t} \Delta\phi_i(t')\Delta\phi_j(t')dt'} \qquad (16)$$

which represents the cross-correlation between residuals, $\Delta\phi$, of light curves i and j, at a lag, τ, computed over a centered interval of length 2t. For the ACF calculations, i equals j, and t corresponds to 2.5 H along the light curve. The results are shown in Figs. 5 and 6. Note that the width of the ACF increases as $\phi^{1/2}$, as predicted, for the weak scintillation case, but the FWHM of the ACF reaches a maximum and then decreases with decreasing stellar intensity. (Further comments?) [Discuss ACF's of finite sources?)

Two Frequency Point Source Correlation Functions

A measure of the importance of diffraction in the formation of an occultation light curve is provided by the cross-correlation function (CCF) of observations observed simultaneously at two different frequencies. In a nondispersive layered medium, goemetric optics dictates that the two light curves would be identical, and the peak CCF would be unity. On the other hand, the Fresnel radius varies with frequency, so that the fine-scale refractivity variations are filtered differently in the two cases. As a result, the maximum of the CCF is expected to be less than unity, on the basis of wave optics.

We have determined the peak CCF for two point source light curves constructed from the same turbulence field but differing by a factor of two in wavelength, as a function of turbulence amplitude and distance along the light curve. The results are shown in Fig. 7. The turbulence amplitude shown corresponds to the shorter wavelength light curve; the corresponding values for the longer wavelength light curves are a factor of two lower. HJW predict a maximum CCF of 0.63 for this case, independent of ϕ, using weak scintillation theory. Our results indicate that the maximum cross-correlation does have a weak dependence on ϕ, and that the maximum decreases as the turbulence strength is increased. [Further comments]

These results apply only to the special case of a point source. In fact, for extended sources, the CCF maximum will be larger than shown in Fig. 7, as long as FWHM of the point source light curve is smaller than the FWHM of the stellar image brightness distribution. For weak scintillations, the effect of image convolution will eventually become unimportant, since the characteristic spike width increases as $\phi^{1/2}$, and will, at some value of ϕ, greatly exceed the image size. As a rough guide, this condition is satisfied when $\phi < \hat{d}_*^{-2}$. When scintillations are strong, the situation is more complicated: the spike width does not increase indefinitely as ϕ decreases (Figs. 5 and 6), while at the same time, the two-frequency CCF peak is depressed as ϕ decreases. In this case, the image convolution has an important effect deep into the occultation, but the intrinsic correlation between the two point source light curves is low.

The significance of these results is that weak scintillation theory provides only a rough limit to the degree of similarity of two-frequency observations. If stellar occultations are evidence of strong turbulence, then the maximum cross-correlation of the two-frequency light curves should be less than that predicted by HJW, when the effects of a finite source are not dominant. In practical cases, it will be important to take care to include such convolution effects, which could be simulated by generating model light curves with parameters appropriate for the specific occultation in question.

Power Spectra of Light Curve Residuals

Although a power spectrum is just the Fourier transform of the ACF, and hence contains no additional information, it does display more clearly than the ACF the relative importance of high-frequency components of light curve residuals. In radio occultations, power spectra have been used to determine the scintillation characteristics in Venus (Woo *et al.*, 1980a) but they have not been used in stellar occultations because of the importance of noise and the consequent limited dynamic range of the usable region of the power spectrum. Nevertheless, it is instructive to translate the ACF results in Figs. 5 and 6 into the parlance of power spectra, and to investigate the effects of finite image size in the presence of strong scintillation.

To begin, we present a theoretical power spectrum for weak anisotropic turbulence in Fig. 8, computed by evaluating the Fourier transform of HJW's Eq. 67 for the one-frequency point source ACF. For this case, we used an anisotropy parameter of $\rho = 50$ (the axial ratio of the turbules), $\phi = 0.1$, and $H = 30$; wavenumber one corresponds to a distance of 5.12 H along the light curve. The maximum of the power spectrum occurs near wavenumber 25, corresponding to a wavelength of about 6 r_f. Note from Fig. 5 that the weak scintillation ACF for $\phi = 1$ is approximately a cosine wave of this wavelength, as one would expect. The fringes in Fig. 8 are closely spaced because $\hat{H} << 1$, and the fringes are deep because $\rho >> 1$.

In passing, we note that we also computed power spectra for weak isotropic turbulence, and confirmed that the results of HJW and of Haugstad (1979) are identical in this case, in spite of their dissimilar outward form [Eq. 67 in HJW and Eq. 3.3 in Haugstad, 1979.] Haugstad does not account for anisotropy in his presentation, but he includes several figures of intensity power spectra for $\hat{H} = 3$ as a function of ϕ.

For comparison, we computed the power spectra of light curve residuals for weak (A = 0.5) and strong (A = 4.0) scintillations, with finite sources of $\hat{d}$ = 0.0, 2.0, and 10.0. The results are shown in Figs. 9 and 10. Again, wavenumber one corresponds to 5.12 H along the light curve. The theoretical power spectrum (Fig. 8) represents the average of a large statistical ensemble, while Figs. 9 and 10 correspond to single samples from such an ensemble, and are therefore somewhat noisy. However, it should be noted that each occultation observation is itself such a sample, and that interpretation of the power spectrum of actual data is subject to the same limitations. The weak scintillation point source power spectrum (Fig. 9) peaks near wavenumber 25 and has the same slope at higher wavenumbers as the theoretical spectrum (Fig. 8), but the deep fringes have been averaged over and are lost in the noise. As the stellar image size is increased, the high frequency tail of the spectrum is truncated and the fringes are reduced, but there remains a significant peak in power near wavenumber 25, where the point source spectrum is at maximum.

In contrast, the strong scintillation point source power spectrum (Fig. 10) does not turn down sharply until wavenumber 100, corresponding to a wavelength of $1.5r_f$. Again, this is consistent with the results of Figs. 5 and 6, which show that the ACF is narrower for strong than for weak scintillation, and consequently has relatively strong high frequency Fourier components. [Further comments? - Effects of changing spectral index?]

Comparison With Observations

To what extent do occultation observations resemble the anisotropic turbulence simulations computed above? For purposes of discussion, we will consider observations of the 1980 August 15 occultation of KM 12 from Cerro Tololo Interamerican Observatory. A detailed discussion of these observations is given by French *et al.* (1982a), and from a comparison of light curves obtained by widely separated observers (French *et al.*, 1982b) concluded that the data are fundamentally inconsistent with isotropic turbulence theory. It remains to consider whether these layers, which are coherent over distances in excess of 60 r_f, are turbulent.

As Crane (1980) points out, the scaling arguments from which the Kolmogorov spectrum is derived apply to the inertial-convective subrange, and, for these scales, the turbulent fluctuations are expected to be isotropic. At larger length scales, in the buoyancy subrange, the turbulence is anisotropic, but the spectrum need not be Kolmogorov, and depends both on the mean atmospheric flow and the strength of the short-period gravity waves present in the flow (Crane, 1980). In the absence of such detailed information about the upper atmosphere of Uranus, we will content ourselves for the moment with a comparison of the statistical properties of the data and the anisotropic turbulence simulations given above, with an outer scale of one scale height.

In Fig. 11, the CTIO immersion light curve of the 1980 event is shown, together with the rms amplitude and modulation index of the fluctuations about the mean curve, computed as before for Fig. 4. For this event, $\hat{d}_* = 1$ (French *et al.*, 1982a), and simulations of weak and strong scintillations for $\hat{d}_* = 1$ are shown in Fig. 3. Of the simulations shown, the observations most closely resemble the $A = 4.0$, $\hat{d}_* = 1.0$, although the spikes are sparser in the data than in the model curves. Statistical analysis of the spikes shows that the modulation index of the observations saturates near unity, and a broad maximum in the rms spike amplitude just below half-light is similar to the strong scintillation results ($A = 4.0$) in Fig. 4 in shape and amplitude. It should be noted that the modulation index is insensitive to the low-frequency variations of the mean light curve that are reflected as large-scale vertical temperature variations in the atmospheric profile obtained by inversion.

The characteristic FWHM of the ACF of the observations is roughly 4.1 km, or 1.7 r_f (French *et al.*, 1982b). In contrast, the maximum ACF FWHM for model strong turbulence light curves with $\hat{d}_* = 1$ is $\approx 0.9\ r_f$. Thus, the spikes are significantly broader than predicted by turbulence theory. There is no evidence for spike broadening deep in the occultation, in contrast to the predictions of weak scintillation theory.

In summary, the observed modulation index resembles the turbulence simulations, but the ACF is significantly broader than the diffraction models predict, suggesting that in some respects, geometric optics may be adequate to account for the observations. Observations at two (or more) widely separated frequencies are necessary before more definitive conclusions can be drawn. In the meantime, it is worth estimating in a simple way the strength of refractivity variations required to produce strong scintillations such as shown in Fig. 2.

Scintillation Strength and Atmospheric Irregularities

For isotropic Kolmogorov turbulence, the usual measure of turbulence strength is the structure constant, C_T, of the temperature fluctuations (Tatarskii, 1971), and the concept can be extended to anisotropic turbulence as well (Woo *et al.*, 1980a). Since the structure constant depends upon the spectral index of the turbulence (which, as we have pointed out, is uncertain for large-scale layered atmospheric inhomogeneities), we will consider the general class of isotropic and layered media in which the resultant rms phase shift upon passage through the atmosphere is dominated by the largest scale features, with characteristic dimension L_c. The Kolmogorov spectrum satisfies this condition. From an obvious generalization of Eq. 1, we have

$$\langle \Phi_t{}^2 \rangle^{1/2} = \frac{2\pi}{\lambda} \int_{-\infty}^{\infty} dz \langle \nu_t{}^2 \rangle^{1/2} \tag{16}$$

The effective path through the atmosphere, L, is given by $(2\pi RH)^{1/2}$, and for isotropic turbulence, there will be $N = L/L_c$ transected independent turbules of size L_c. Then adopting the usual random-walk assumptions, we can approximate Eq. (16) as

$$\langle\phi_t{}^2\rangle^{1/2}_{iso} = \frac{2\pi}{\lambda} L_c\ N^{1/2}\langle\nu_t{}^2\rangle^{1/2}_{iso} \tag{17}$$

or

$$\langle\phi_t{}^2\rangle^{1/2}_{iso} = \frac{2\pi}{\lambda} (L\ L_c)^{1/2}\ \langle\nu_t{}^2\rangle^{1/2}_{iso}\ , \tag{18}$$

a result obtained by HJW. In terms of the rms fractional refractivity fluctuations, $\langle(\nu_t/\nu_A)^2\rangle^{1/2}_{iso}$, and the normalized stellar intensity, ϕ, we find:

$$\langle\phi_t{}^2\rangle^{1/2}_{iso} = \frac{(2\pi)^{3/4}\ H^{7/4}\ L_c{}^{1/2}}{r_f{}^2\ R^{1/4}}\left(\frac{1}{\phi} - 1\right)\left\langle\left(\frac{\nu_t}{\nu_A}\right)^2\right\rangle^{1/2}_{iso} \tag{19}$$

If the turbulence is Kolmogorov, the fractional refractivity fluctuations can be related to the structure constant (Haugstad, 1981):

$$\frac{\nu_t}{\nu_A}\quad{}^{2}\quad{}^{1/2} \simeq \frac{L_c{}^{1/3}C_T}{2^{1/2}(\gamma-1)T_o} \tag{20}$$

where γ is the ratio of specific heats and T_o is the mean temperature of the background atmosphere. Then

$$\langle\phi_t{}^2\rangle^{1/2}_{iso} = \frac{2^{1/4}\ \pi^{3/4}\ H^{7/4}\ L_c{}^{5/6}}{(\gamma-1)\ r_f{}^2\ R^{1/4}T_o}\left(\frac{1}{\phi} - 1\right)\left\langle\left(\frac{\nu_t}{\nu_A}\right)^2\right\rangle^{1/2}_{iso} \tag{21}$$

With Eq. 13, we can relate the turbulence strength, A, directly to the structure constant:

$$A = \frac{2^{1/2}\pi}{(\gamma-1)T_o}\left(\frac{H}{r_f}\right)^2 L_c{}^{1/3}\ C_T \quad \text{(isotropic)} \tag{22}$$

Analogous results for layered atmospheric structure can be found with the modification that N, the number of independent turbules crossed by a ray, is now given by H/L_c:

$$\langle\phi_t{}^2\rangle^{1/2} = \frac{2\pi\ H^{3/2}\ L_c{}^{1/2}}{r_f{}^2}\left(\frac{1}{\phi} - 1\right)\left\langle\left(\frac{\nu_t}{\nu_A}\right)^2\right\rangle^{1/2} \tag{23}$$

or

$$\langle \phi_t^2 \rangle^{1/2} = \frac{2^{1/2}\,\pi\, H^{3/2}\, L_c^{5/6}}{(\gamma-1)\, r_f^2\, T_o} \left(\frac{1}{\phi} - 1\right) C_T \qquad (24)$$

Recall that $A = \langle \phi_t^2 \rangle^{1/2}$ for the case $\phi = 0.5$.

Comparing Eqs. 19 and 13, we find the ratio of the rms phase shift for layered and isotropic turbulence with the same outer scale and rms refractivity to be

$$\frac{\langle \phi_t^2 \rangle^{1/2}}{\langle \phi_t^2 \rangle^{1/2}_{iso}} = \left(\frac{2\pi R}{H}\right)^{1/4} \qquad (25)$$

The implication is that anisotropic turbulence should give enhanced scintillations compared to isotropic turbulence, for the usual circumstance, $R/H \gg 1$. Physically, this is because there is less cancellation of phase: fewer independent turbules are encountered in a layered medium, and the contribution of each turbule is enhanced by the long slant path of the ray through the fluctuation.

To obtain a feeling for the magnitudes involved, we note that, for Kolmogorov turbulence,

$$C_T \approx \frac{\Delta T}{(\Delta r)^{1/3}} \qquad (26)$$

where ΔT is the rms temperature difference over a separation distance of Δr. For Uranus, we adopt $L_c = H = 70$ km, $R = 26000$ km, $T = 150$ K, $\gamma = 1.47$, and $r_f = 2.45$ km. Then, from Eqs. 21 and 29 we have

$$A = 30\, \frac{\Delta T}{(\Delta r)^{1/3}} \quad \text{(isotropic)} \qquad (27)$$

and

$$A = 210 \frac{\Delta T}{(\Delta r)^{1/3}} \quad \text{(layered)} \qquad (28)$$

for Δr in km. (Note that the turbulence amplitude for a layered atmosphere is ~7 times larger than for the isotropic case.) Since the simulations show that intense scintillations occur for $A \gtrsim 1$, we conclude that, in a layered atmosphere, temperature variations as small as 0.005 K over an altitude range $\Delta r = 1$ km can produce large spikes.

It is unlikely that such small temperature fluctuations could be maintained coherently over the large horizontal distances (>140 km) for which individial light curve spikes remain recognizable (French et al., 1982b). Of course, Eqs. 27 and 28 assume Kolmogorov scaling of the variations. An alternate possibility is that the anisotropic turbulence spectrum is flatter than the Kolmogorov law, but Crane (1980) shows that in fact the vertically directed spectrum has a steeper slope than the Kolmogorov spectrum. Still another possibility is that the spikes are produced by relatively large-scale structure (with typical length scale > r_f). We discuss these possibilities in greater detail in the next section. [Note: this transition needs to be improved].

III. Atmospheric Waves, Spikes, and Ray Crossing

We have demonstrated that intense scintillations can occur in occultations by atmospheres with $C_T = 0.01$ K km$^{-1/3}$. For comparison, a typical terrestrial value is $C_T = 0.2$ K km$^{-1/3}$ in the lower stratosphere (Crane, 1980), and $C_T = 1.5$ K km$^{-1/3}$ for

Venus at 60 km altitude (Woo and Ishimaru, 1981). The strong evidence for layering in the Uranus makes such comparisons misleading, however. It seems far more likely that the Uranian upper atmosphere has a combination of small-scale isotropic turbulence, moderately anisotropic turbulence at larger scales, and underlying atmospheric structure of significant horizontal extent. Under these more complicated circumstances, what does an occultation curve look like? How well can the numerical inversion method (which assumes horizontal coherence over a distance $L \sim (2\pi RH)^{1/2}$ (French et al., 1978) retrieve the true atmospheric basic state in the presence of turbulence and horizontal inhomogeneities? To explore some of these issues, we have constructed light curves for a variety of model atmospheres with large-scale non-isothermal features.

A. Waves in the Presence of Turbulence

If the spikes in the Uranus observations (Fig. 11) are in fact turbulence-induced scintillations, is it still possible for large-scale layered structure in the atmosphere to be correctly determined by numerical inversion? As a test, we generated, using wave optics, light curves for a model atmospheres with a vertical wave of constant fractional refractivity ϵ (with $\epsilon << 1$) and vertical wavenumber $\mu = 2\pi n/H_0$, where n is the number of vertical wavelengths per scale height and H_0 is the mean atmospheric scale height. The corresponding perturbation phase component on the thin screen,

Φ_w, obtained by integrating along the ray-path through the atmosphere, is given by

$$\Phi_w(r) = 2\pi \left(\frac{H_o}{r_f}\right)^2 \frac{\sin[{}^1/_2 \tan^{-1}(\mu H_o) + \mu(r-r_o) + \psi]}{[1 + (\mu H_o)^2]^{1/4}} \qquad (29)$$

where ψ specifies the phase of the atmospheric wave at the half-light altitude, $r=r_o$. The temperature profile corresponding to the sinusoidal refractivity profile is obtained by integrating the hydrostatic equation and using the perfect gas law, with the result:

$$H(r) = H_o \left\{ \frac{[1 + \frac{\varepsilon}{[1+(\mu H_o)^2]}(\sin \Omega + \mu H_o \cos \Omega)]}{(1 + \varepsilon \sin \Omega)} \right\} \qquad (30)$$

where the temperature is expressed in terms of scale height, and

$$\Omega = \mu(r-r_o) + \psi \qquad (31)$$

In the short wavelength limit, $\mu H_o >> 1$, the temperature profile is sinusoidal with amplitude ε. In the long wavelength limit, $\mu H_o << 1$, and the temperature wave is strongly suppressed, with amplitude $\varepsilon(\mu H_o)^2 << \varepsilon$.

As a typical example, we present results for the case, $n = 3$, $\varepsilon = 0.005$. The light curve corresponding to this wave is shown in Fig. 12a. The stretching of the sinusoidal variations is clearly evident deep in the light curve. Next, we added the wave perturbation phase front, Φ_w, to the appropriate perturbation phase front for strong scintillation (A = 4.0), and constructed the corresponding light curve (Fig. 12b). Also shown is the light curve for turbulence alone (Fig. 12c).

The effects of the wave are barely perceptible by eye when strong turbulence is present. The results of numerical inversion of these light curves are shown in Fig. 13. The sinusoidal variation in temperature is retrieved exactly, in the absence of turbulence (Fig. 13a), and is still clearly discernible when strong scintillation is present (Fig. 13b). The spurious temperature variations due to the turbulence alone are shown in Fig. 14c, Here, even for strong scintillations, these spurious variations are only a few tenths of one per cent. We conclude that the horizontally non-varying component of the thermal structure can still be retrieved, even when strong turbulence is present. It is interesting that observations of oceanic eddies suggest that such mixtures of turbulence and waves do occur in fluids of geophysical interest (Rhines, 1973). We note parenthetically that the rms amplitude of the fluctuations is almost identical for the two turbulent light curves in Fig. 12, so that such statistical calculations act as high-pass filters, and are not sensitive to low-amplitude long wavelength atmospheric structure.

B. Occultations by Atmospheres With Gravity Waves

The simultaneous presence of turbulence, gravity waves, and global-scale layered structure in real atmospheres introduces both complexity and uncertainty into the spectrum of refractivity variations. We have determined that the radially symmetric component of the atmospheric structure can be retrieved in the midst of turbulence, as long as ray crossing is not severe, but many layered features in atmospheres are patchy and localized, and are not coherent over the distance $L = (2\pi RH)^{1/2}$ required by the inversion method.

Occultation temperature profiles are frequently characterized by wavelike variations which, for the β Sco occultation by Jupiter, are consistent with gravity waves (French and Gierasch, 1974). The confirmation of this interpretation would be significant, since propagating inertia gravity waves can be important to the upper atmospheric energy balance. To explore this issue, we have constructed model light curves for an isothermal atmosphere with a realistic field of gravity waves, using geometric optics. We assume a vertical wavelength $\lambda_v = H$, and horizontal wavelengths λ_h of ∞, 20, 15 and 10 times the scale height, H. The radius of the planet is chosen to be $R = 1000\ H$. The ratio, λ_h/L, is a measure of the horizontal coherence of the atmosphere. For $\lambda_h/L < 1$, the assumptions of the inversion method are no longer satisfied.

In the absence of damping, temperature perturbations grow exponentially with height, for gravity waves, but in real atmospheres such growth is checked by internal instabilities, or by trapping and reflection of the waves. We model the situation where the eddy diffusivity is just sufficient to suppress the exponential growth, so that the fractional amplitude, ϵ, of the wave is constant with height; we take $\epsilon = 0.05$. The refractivity field is definied, after French and

Gierasch (1974), as

$$\nu(r,z) = \nu_A\left\{1 + \epsilon \sin\left[\mu(r-r_o) + kz + \psi\right)\right]\right\} \qquad (32)$$

where μ and k are the vertical and horizontal wavenumbers, respectively.

The resulting light curves are displayed in Fig. 14. The top figures corresponds to a radially symmetric atmosphere. As λ_h is decreased, the horizontal structure changes significantly over L, the effective path length through the atmosphere, and the broad spikes in the corresponding light curves are suppressed and, ultimately, become imperceptible. The corresponding temperature profiles, obtained by inversion of the light curves, are shown in Fig. 15. For $\lambda_h/L \lesssim 0.25$, the vertical structure of the atmosphere can no longer be determined accurately by numerical inversion because of horizontal averaging effects.

C. Severe Ray Crossing

The preceding simulations demonstrate that horizontal inhomogeneities produced by either turbulence or by larger scale waves have little effect on the inferred temperature profile, and that the quasi-global component of the atmospheric structure can be accurately retrieved even when turbulence and short-wavelength waves are strong. This is not true in general: an implicit assumption of the inversion technique is that ray crossing is not severe, since the method requires that the light at a point on the light curve corresponds to a unique ray. In the wave model for spikes, it can be shown that the condition for eventual ray crossing, as $\phi \to 0$, is:

$$\epsilon(\mu H)^{3/2} > 1 \qquad (33)$$

or

$$\epsilon(2\pi n)^{3/2} > 1 \qquad (34)$$

Thus, for a given vertical wavelength, there is a critical wave amplitude, ϵ, above which ray crossing will occur. Fig. 16 displays the regimes of no ray crossing and of eventual ray crossing.

What is the effect of ray crossing on the inversion technique? In any inversion, the light curve is divided into bins and the average flux in computed for each bin. If the ray crossing is sufficiently mild to be confined to a single bin, then the inversion will not be affected, since the mean flux does not depend on how the rays have distributed themselves in any given bin. We find that the minimum altitude interval that can be resolved, Δh, is given by

$$\frac{\Delta h}{H} > \epsilon(\mu H)^{1/2} \qquad (35)$$

or

$$\frac{\Delta h}{H} > \epsilon(2\pi n)^{1/2} \qquad (36)$$

In order to resolve a wave of n wavelengths per scale height, we require $\Delta h < {}^{1}/2nH$; thus, the maximum amplitude wave that can be resolved when ray crossing is present is given by

$$\epsilon < 1/(8\pi)^{1/2}n^{3/2} \qquad (37)$$

Two model light curves with ray crossing are shown in Fig.

17. In the first case, a fairly large vertical wavelength (λ_v = H/2, or n = 2) of amplitude ε = 0.1 is assumed. According to Eq. 37, the maximum amplitude wave that can be resolved is ε = 0.07, so that ray crossing is severe. In the second case, λ_v = H/5, n = 5, and ε = 0.025. The critical amplitude from Eq. 37 is ε = 0.018, and again, ray crossing is severe. In each case, the refractivity perturbations produce intense, sharp spikes in the light curve. Inversion of the light curves yields the derived temperature profiles shown in Fig. 17. At first, the correct atmospheric structure is derived. As the inversion proceeds and ray crossing becomes severe, the computed profile shows a strongly damped wave, whereas in fact the true profile has a constant amplitude wave. The result is that the inversion essentially "ignores" the severely crossed rays, and, importantly, introduces only very minor spurious features into the derived profiles. When the ray crossing is not severe, the inversion technique introduces insignificant error into the retrieved profiles, a result also obtained by Wallace (1975).

All of the foregoing simulations tend to confirm the following assertion: *Quasi-global features of atmopsheric structure are accurately determined by numerical inversion; horizontally inhomogeneous structures (including turbulence) with coherence scale L << $(2\pi RH)^{1/2}$ are filtered out and have little effect on the derived temperature profiles.* Naturally, the influence of photon noise and terrestrial scintillation must also be considered when interpreting the observations.

D. The Wave Optics of Ray Crossing

The light curves in Fig. 17 were computed using geometric optics, which is not legitimate for determining the detailed structure of well-focussed or over-focussed spikes. We have, therefore, computed light curves of a sequence of increasingly sharp spikes to determine the effects of diffraction in the ray-crossing regime. In Fig. 19, a sequence of spikes is displayed. The upper figures were computed with wave optics, and for the lower figures we employed geometric optics. In each case, an atmospheric wave with vertical wavelength λ_V = H/4 was used. Each figure shows the same region of the resultant light curve; the only differences are in the amplitude of the wave, ε, and in the optics assumed. (Note, however, that the vertical scale varies from plot to plot.) For the first case ($\varepsilon = 0.01$), wave optics and geometric optics give essentially identical results. For $\varepsilon = 0.015$, diffraction fringes become apparent for this very sharp spike, and for the ray-crossed spikes in the two final cases, there are strong interference fringes in the wave optical results.

Although the detailed structure of the spikes clearly depends on the assumed atmospheric structure, a general result is that a single layered feature can be responsible for many detailed variations in the light curve. This suggests that multiple-peaked "blobs" along the tail of an occultation light curve may represent diffraction of light passing through a single coherent layer, rather than through multiple layers. (An example of such features is shown in Fig. 2c of French et al. (1982b), for the 15 August 1980 occultation by Uranus.)

IV. Conclusions

Many of the problems of interpretation of stellar occultation observations stem from the difficulty of defining in a general way the effects that realistic atmospheric structure have on the resultant light curves. The theory of turbulent scintillations in occultations has been well developed, for conditions of interest, only for weak scintillations (HJW), whereas the assumption of perfect layering in the atmosphere has permitted temperature profiles to be derived whose validity is uncertain. We have formulated quite general techniques for producing model light curves for a wide variety of realistic atmospheres, not subject to the above restrictions. We generally confirm the weak-scintillation results of HJW, but we find that there are important qualitative differences for strong scintillations. These include saturation of the modulation index at unity for strong, one-dimensional, Kolmogorov turbulence, and independence of the FWHM of the ACF of light curve residuals upon the mean intensity, ϕ, in strong contradiction to weak scintillation theory. Comparison of recent observations with the turbulence simulations reveals that the modulation index of the observations saturates at unity, suggestive of strong scintillation, but that the FWHM of the ACF is significantly wider than the turbulence simulations. The critical test of the importance of diffraction effects will be to observe an occultation of a small star at two widely separated frequencies.

Although it remains an open question whether or not the fine-scale structure observed during occultations is turbulent scintillation, we have demonstrated in a variety of ways that the numerical inversion of light curves is only weakly influenced by horizontally inhomogeneous atmosperic structure, and that the underlying large-scale coherent structure can be retrieved. This suggests the possibility that occultations will allow us to determine both the quasi-global atmospheric structure and the statistical characteristics of small-scale refractivity variations. A large number of high-quality observations of occultations exist, and a most productive approach would be to construct model turbulent light curves for the specific parameters (H, r_f, and d*) appropriate to each event. By comparing the statistical properties of the observations with the simulations, it should be possible to restrict considerably the possible turbulence characteristics in these planetary upper atmospheres.

Acknowlegments

We would like to thank W.B. Hubbard, B. Haugstad, and R. Woo for helpful discussions. This work was supported in part by NASA Grant NAGW-68 and by [R.L. - add your acknowledgements (Joyce?) and grants.]

APPENDIX I

A	Turbulence Amplitude
ACF	Autocorrelation Function
C	Generalized Correlation Function
C_T	Structure Constant of Turbulence
CCF	Cross-Correlation Function
D	Earth-Planet distance
d_*	Projected Stellar Diameter (km)
$\hat{d}_*$	Non-dimensional Stellar Diameter (d_*/r_f)
E	Point Source Wave Amplitude at the Earth
E_s	Point Source Wave Amplitude at the Reference Screen
FFT	Fast Fourier Transform
H	Atmospheric Scale Height
$\hat{H}$	Non-Dimensional Scale Height (H/r_f)
H_o	Scale Height of Mean Atmosphere
I	Point Source Wave Intensity at the Earth
I_{fs}	Finite Source Wave Intensity at the Earth
iso	Isotropic
k	Horizontal Wavenumber of Inertia-Gravity Wave
L	Effective Path Length Through the Atmosphere $[(2\pi RH)^{1/2}]$
L_c	Outer Scale of Turbulence
m	Modulation Index of Light Curve Fluctuations
N	Number of Turbules Transected by a Ray
n	Number of Vertical Wavelengths per Scale Height of an Atmospheric Wave
P_s	Wavenumber Power Spectrum of Phase on the Reference Screen
P_ν	Wavenumber Power Spectrum of Atmospheric Refractivity Fluctuations
q_x	Vertical Wavenumber of Turbulent Refractivity Fluctuations
R	Radius of Planet
r	Distance from Center of Planet
r_f	Fresnel Scale $[(\lambda D)^{1/2}]$
r_o	Distance from Center of Planet of Half-light Ray
S	Brightness Distribution of the Star
t	Half-width of Interval Over Which Correlation is Computed
T_o	Mean Temperature of Background Atmosphere
x	Vertical Coordinate
y	Horizontal Coordinate Perpendicular to Earth-Planet Line
z	Horizontal Coordinate Parallel to Earth-Planet Line
γ	Ratio of Specific Heats
Δh	Altitude Interval in Atmosphere
Δr	Interval in Altitude
ΔT	RMS Temperature Difference Over a Separation Distance of Δr

$\Delta\phi$	Deviation of Normalized Light Curve Intensity from Mean Value, ϕ.
ϵ	Fractional Amplitude of Atmospheric Wave in Refractivity
θ_x	Subtended Angle in x Direction as Viewed from Earth
θ_y	Subtended Angle in y Direction as Viewed from Earth
θ_*	Subtended Angle of Star as Viewed from Earth
λ	Wavelength of Light
λ_h	Horizontal Wavelength of Inertia-Gravity Wave
λ_v	Vertical Wavelength of Inertia-Gravity Wave
μ	Vertical Wavenumber of Inertia-Gravity Wave
ν	Atmospheric Refractivity
ν_A	Mean Atmospheric Refractivity
ν_t	Turbulent Atmospheric Refractivity
ν_o	Atmospheric Refractivity at Altitude of Half-light Ray
ρ	Axial Ratio of Anisotropic Turbules (Horizontal/ Vertical)
τ	Lag of Correlation Function
Φ	Phase Shift of Plane Wave Produced by Passage Through the Atmosphere
Φ_A	Contribution of Mean Atmosphere to Φ
Φ_t	Contribution of Turbulence to Φ
Φ_w	Contribution of Atmospheric Waves to Φ
ϕ	Mean Intensity of Light Curve, In Units of Intensity of the Unocculted Star
ψ	Phase of Atmospheric Wave at Half-light Altitude, r_o
Ω	Phase of Atmospheric Wave at Altitude, r

REFERENCES

Armand, N.A., Lomakin, A.N. and Sarkisyanz, V.A. (1975). Antenna investigation of a statistically inhomogeneous atmosphere. Radio Science 10, ** get page number **.

Crane, R.K. (1980). A review of radar observations of turbulence in thelower stratosphere. Radio Science 15, 177-193.

Dunham, E., Elliot, J.L. and Gierasch, P.J. (1980). The upper atmosphere of Uranus: mean temperature and temperature variations. Ap.J. 235, 274-284.

Elliot, J.L., French, R.G., Dunham, E., Gierasch, P.J., Veverka, Church, C. and Sagan, C. (1977). Occultation of ε Geminorum by Mars. II. The structure and extinction of the martian upper atmosphere. Ap.J. 217, 661-679.

Eshleman, V.R. and Haugstad, B.S. (1979). Comment on the W.B. Hubbard paper, 'On the atmosphere with exponential turbulence'". Icarus 39, 479-485.

Freeman, K.C. and Lyngå, G. (1970). Data for Neptune from occultation observations. Ap.J. 160, 767-780.

French, R.G., Elliot, J.L. and Gierasch, P.J. (1978). Analysis of stellar occultation data. Icarus 33, 186-202.

French, R.G. and Elliot, J.L. (1979). Occultation of ε Geminorum by Mars. III. Temperature structure of the martian upper atmosphere. Ap.J. 229, 828-845.

French, R.G., Elliot, J.L., Dunham, E.W., Allen, D., Elias, J.H., Frogel, J.A. and Liller, W. (1982a). The thermal structure and energy balance of the uranian upper atmosphere. Icarus, submitted.

French, R.G., Elliot, J.L., Sicardy, B., Nicholson, P. and Matthews, K. (1982b). The upper atmosphere of Uranus: A critical test of isotropic turbulence models. Icarus, in press.

French, R.G. and Gierasch, P.J. (1974). Waves in the jovian upper atmosphere. J. Atmos. Sci. 31, 1707-1712.

Haugstad, B.S. (1978a). Turbulence in planetary occultations. I. A theoretical formulation. Icarus 35, 121-138.

Haugstad, B.S. (1978b). Turbulence in planetary occultations. II. Effects on atmospheric profiles derived from Doppler measurements. Icarus 35, 410-421.

Haugstad, B.S. (1978c). Turbulence in planetary occultations. III. Effects on atmospheric profiles derived from intensity measurements. Icarus 35, 422-435.

Haugstad, B.S. (1979). Turbulence in planetary occultations. IV. Power spectra of phase and intensity fluctuations. Icarus 37, 322-335.

Haugstad, B.S. (1981). Spacecraft and stellar occultations by turbulent planetary atmospehres. NDRE 81, 1002.

Hubbard, W.B. (1979a). The ε Geminorum occultation: Evidence for waves or turbulence. Ap.J. 229, 821-827.

Hubbard, W.B. (1979b). On the atmosphere with exponential turbulence. Icarus 39, 473-476.

Hubbard, W.B., Jokipii, J.R. and Wilking, B.A. (1978). Stellar occultations by turbulent planetary atmospheres: A wave-optical theory including a finite scale height. Icarus 34, 374-395.

Jokipii, J.R. and Hubbard, W.B. (1977). Stellar occultations by turbulent planetary atmospheres: The Beta Scorpii events. Icarus 30, 537-550.

Klemola, A.R. and Marsden, B.G. (1977). Predicted occultations by the rings of Uranus: 1977-1980. A.J. 82, 849-851.

Kovalevsky, J. and Link, F. (1969). Diamètre, aplatissement et propriétés optiques de la haute atmosphère de Neptune d'après l'occultation de l'étoile BD-17°4388. Astron. Astrophys. 2, 398-412.

Marians, M. (1975). Computed scintillation spectra for strong turbulence. Radio Science 10, 115-119.

Rhines, P. (1973). Observations of the energy-containing oceanic eddies, and theoretical models of waves and turbulence. Boundary-Layer Meteorology 4, 345-360.

Rumsey, V.H. (1975). Scintillations due to a concentrated layer with a power-law turbulence spectrum. Radio Science 10, 107-114.

Tatarskii, V.I. (1971). In The Effects of the Turbulent Atmospheres on Wave Propagation, National Technical Information Service, Springfield.

Texas-Arizona Occultation Group. (1977). The occultation of Epsilon Geminorum by Mars: Analysis of McDonald data. Ap.J. 214, 934-945.

Veverka. J., Wasserman, L.H., Elliot, J.L., Sagan, C. and Liller, W. (1974a). The occultation of β Scorpii by Jupiter. I. The structure of the jovian upper atmosphere. A.J. 79, 73-84.

Wallace, L. (1975). On the occultation of BD-17°4388 by Neptune. Ap.J. 197, 257-261.

Woo, R., Armstrong, J.W. and Ishimaru, A. (1980a). Radio occultation measurements of turbulence in the venus atmosphere by Pioneer Venus. J.G.R. 85, 8031-8038.

Woo, R. and Ishimaru, A. (1981). Eddy diffusion coefficient for the atmosphere of Venus from radio scintillation measurements. Nature 289, 383-384.

Woo, R., Ishimaru, A. and Yang, F.C. (1980b). Radio scintillations during occultations by turbulent planetary atmospheres. Radio Science 15, 695-703.

Woo, R., Yang, F.C. and Ishimaru, A. (1975). Wave propagation in a random medium with inhomogeneous background. J.G.R. 85, 8021-8038.

Young, A.T. (1976). Scintillation during occultations by planets. Icarus 27, 335-358.

TABLE I

Recent Stellar Occultations

Date	Planet	Star	Observatory	λ(μm)	r_f (km)	H(km)	$\hat{H}$	d_*(km)	$\hat{d}_*$	References
4/7/68	Neptune	Bd-17°4388	Mt. Stromlo	0.55	1.5	55	35	10	6.4	Freeman and Lyngå (1970)
5/13/71	Jupiter	β Sco	Boyden	0.35	0.48	25	52	1.3	2.7	Veverka *et al.* (1974)
				0.39	0.51	25	49	1.3	2.5	
				0.62	0.64	25	39	1.3	2.0	
4/18/76	Mars	ε Gem	KAO[a]	0.38	0.30	7.5	25	6	20	Elliot *et al.* (1977)
				0.45	0.33	7.5	23	6	19	
				0.75	0.41	7.5	18	6	15	
3/10/77	Uranus	SAO 158687	KAO[a]	0.62	1.3	45	35	7	5.4	Dunham *et al.* (1980)
				0.73	1.4	45	32	7	5	
				0.85	1.5	45	30	7	4.7	
8/15/80	Uranus	KM12[b]	CTIO[c]	2.2	2.4	70	29	2.4	1.0	French *et al.* (1982a)

Notes

[a] KAO - Kuiper Airborne Observatory
[b] KM 12 - Star #12 on the list of Klemola and Marsden (1977)
[c] CTIO - Cerro Tololo Interamerican Observatory

FIGURE CAPTIONS

Fig. 1. Occultation Geometry. The distortions in the wave front of a plane wave, due to passage through a turbulent atmosphere, can be represented by a thin phase-changing screen at distance D from the earth's path. The light curve as viewed from the earth along its path is computed in overlaping sections (for example, A and B) by summing the phases of the appropriate section of the upstream phase screen. Edge effects are avoided by apodizing.

Fig. 2. Occultation light curves for model isothermal atmospheres with anisotropic Kolmogorov turbulence. A measure of the turbulence strength is given by A, the rms turbulence-induced phase change (in radians) at the level in the atmosphere corresponding to the half intensity ra For $A \gtrsim 1$, the resultant scintillations are strong.

Fig. 3. Turbulent occultations of a finite source. In the simulations at left, a weak-scintillation ($A = 0.5$) point-source light curve is convolved with succesively larger sources whose diameter at the occulted planet is $d*$ (in units of r_f). On the right, a strong scintillation ($A = 4.0$) case is shown. The scintillations are strongly damped for $d* \gtrsim 2\ r_f$.

Fig. 4. Statistical properties of turbulent scintillations. The rms amplitude of the fluctuations from the mean of the point-source light curves in Fig. 2 is plotted as a function of distance along the earth's path. The

triangles mark the measured values and the solid line is from HJW's weak scintillation theory. Also shown is an isothermal light curve. Note that the scales on successive plots are increased by a factor of two. As the turbulence strength increases beyond A = 2, the scintillations saturate, a phenomenon not predicted by weak scintillation theory. At right, the modulation index is shown for the same circumstances, along with the weak scintillation model of HJW. As the turbulence becomes very strong, the modulation index saturates to unity.

Fig. 5. Autocorrelation function of point source light curve residuals for weak (A = 0.5) and strong (A = 4.0) turbulence. For weak scintillation, the ACF broadens as the stellar flux, ϕ, decreases, but for strong scintillation, the ACF remains essentially independent of ϕ.

Fig. 6. Point source autocorrelation FWHM for residuals of turbulent light curves. For weak turbulence, the weak-scintillation model, shown by a bold solid line, is obeyed: the FWHM increases as $\phi^{-1/2}$. For turbulence amplitudes A $\gtrsim$ 2, the FWHM of the ACF remains small at all ϕ.

Fig. 7. Two-frequency cross-correlation of turbulent point-source light curve residuals for a frequency ratio of 2. The prediction of HJW's weak scintillation theory is shown dashed. As the turbulence amplitude is increased, the maximum cross-correlation diminishes.

Fig. 8. Theoretical power spectrum of light curve residuals

for weak anisotropic turbulence, calculated from HJW's model. See text for details.

Fig. 9. Computed power spectra of light curve residuals for model turbulent occultations of a finite source with projected diameter $d*$ (in units of r_f) and turbulence amplitude $A = 0.5$, corresponding to weak scintillation.

Fig. 10. Computed power spectra of light curve residuals for model turbulent occultations of a finite source with projected diameter $d*$ (in units of r_f) and turbulence amplitude $A = 4.0$, corresponding to strong scintillation.

Fig. 11. Occultations observations from CTIO of the 8/15/80 Uranus occultation of KM 12. The immersion light curve contains many sharp spikes. The rms amplitude and modulation index of the fluctuations are plotted as triangles, below. Also shown is the model isothermal light curve scaled appropriately for the occultation.

Fig. 12. Model occultation light curves for radially symmetric atmospheres containing waves and/or strong turbulence, computed using wave optics. Notice that, in the presence of turbulence, the effects of the wave are barely perceptible to the eye.

Fig. 13. Temperature profiles obtained by numerical inversion of the light curves in Fig. 12. The wave is still clearly resolved, in the presence of strong turbulence.

Fig. 14. Model occultation light curves for atmospheres containing inertia-gravity waves. See text for details.

Fig. 15. Temperature profiles obtained by numerical inversion

of the light curves in Fig. 14. As the horizontal wavelength of the gravity waves is decreased, the inversion technique is less and less able to determine the true atmospheric basic state.

Fig. 16. Ray-crossing regimes.

Fig. 17. Model light curves, computed from geometric optics, for two cases of severe ray crossing. Intense spikes are caused by the focussing of starlight by the atmospheric waves.

Fig. 18. Temperature profiles obtained by numerical inversion of the light curves in Fig. 17. Deep into the occultation, severe ray crossing prevents the true atmospheric structure from being determined.

Fig. 19. Comparison of light curve spikes computed from wave optics (upper) and geometric optics (lower) for atmospheric waves whose fractional amplitude, ϵ, is increased from 0.01 (left figures) to 0.025 (right figures). When diffraction effects are taken into account, the light curve contains many fringes. Note the vertical scales.

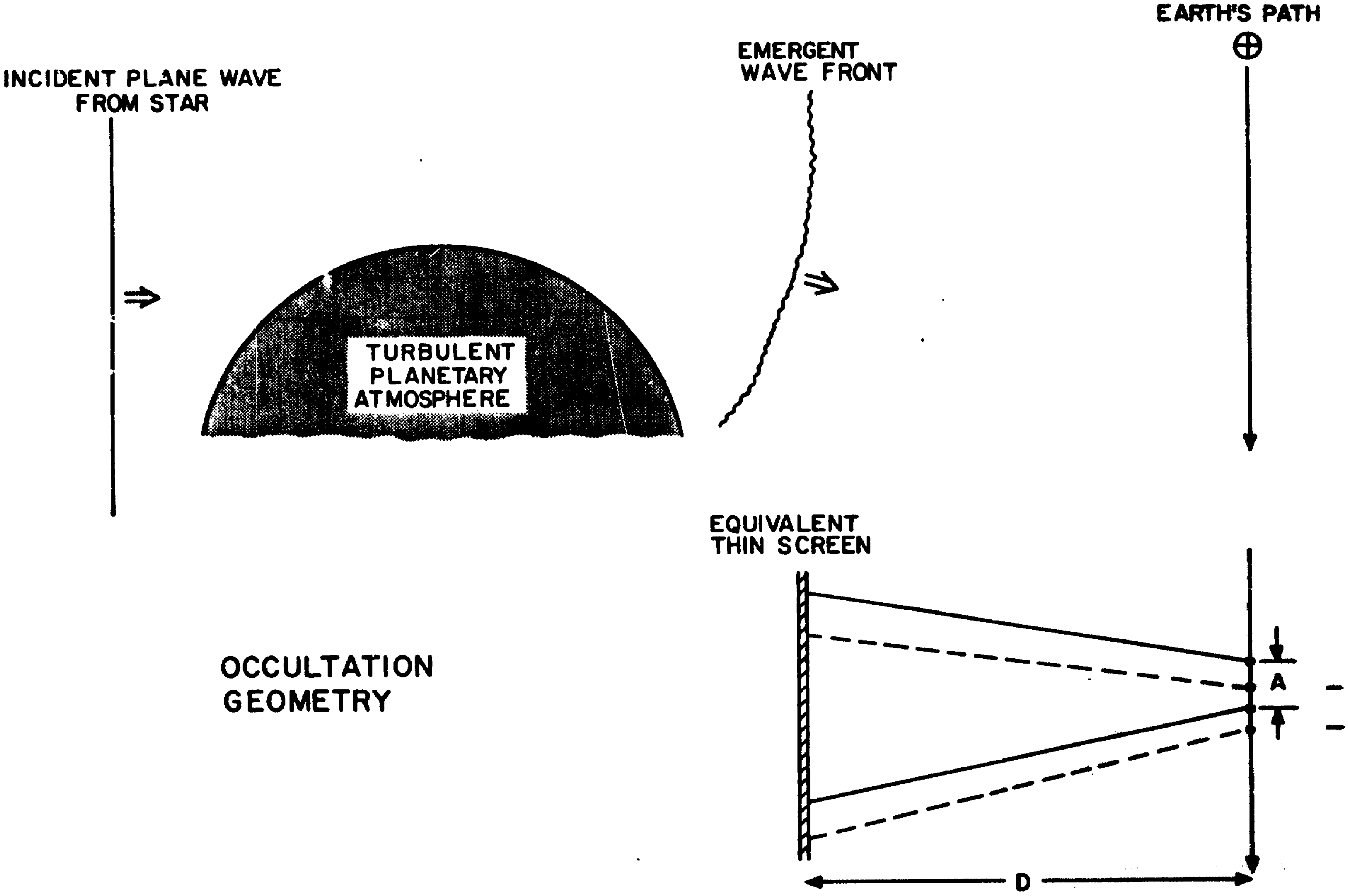
INCIDENT PLANE WAVE FROM STAR
TURBULENT PLANETARY ATMOSPHERE
EMERGENT WAVE FRONT
EARTH'S PATH
⊕
EQUIVALENT THIN SCREEN
A
B
D
OCCULTATION GEOMETRY

Fig. 1

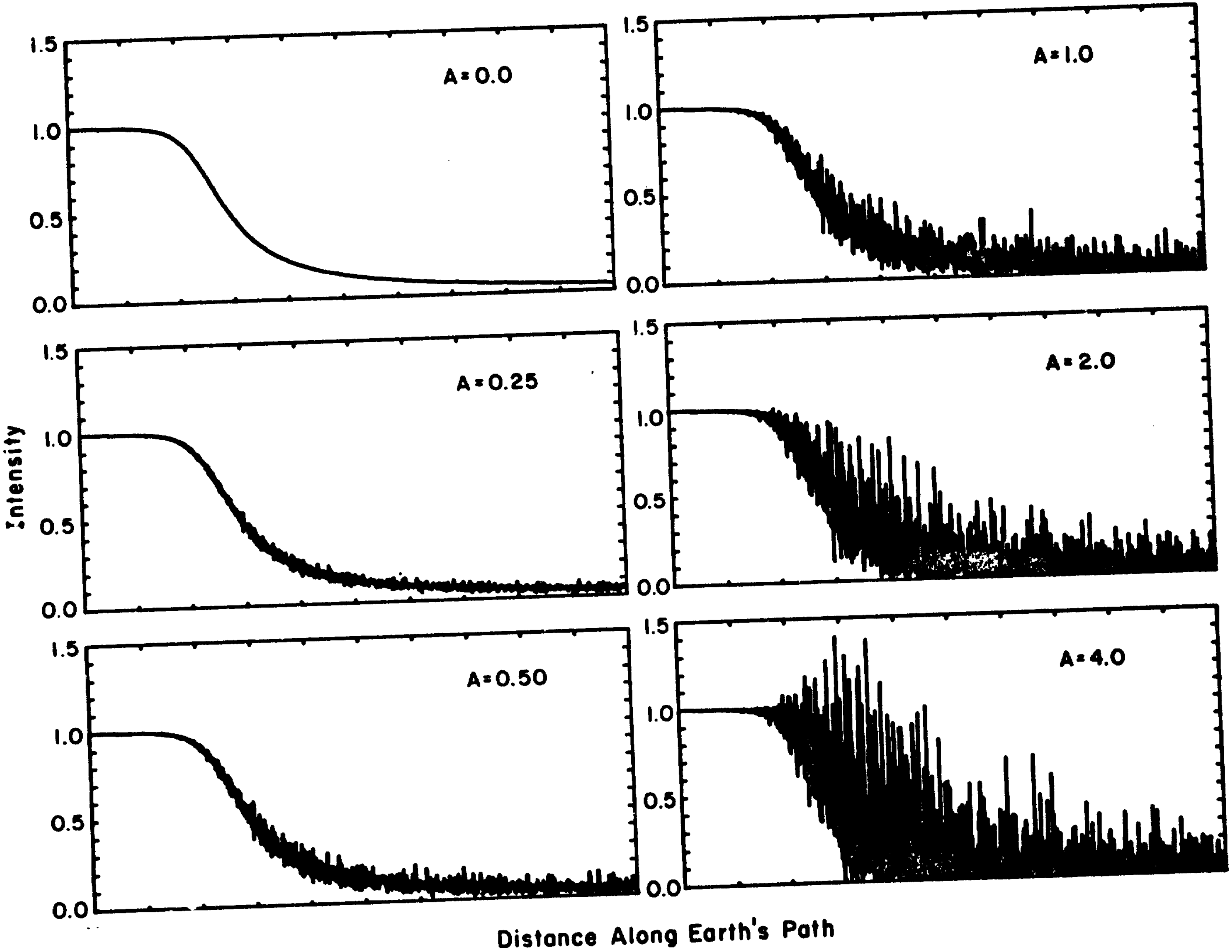
A=0.0
A=1.0
A=0.25
A=2.0
A=0.50
A=4.0
1.5
1.0
0.5
0.0
Intensity
Distance Along Earth's Path

Fig 2

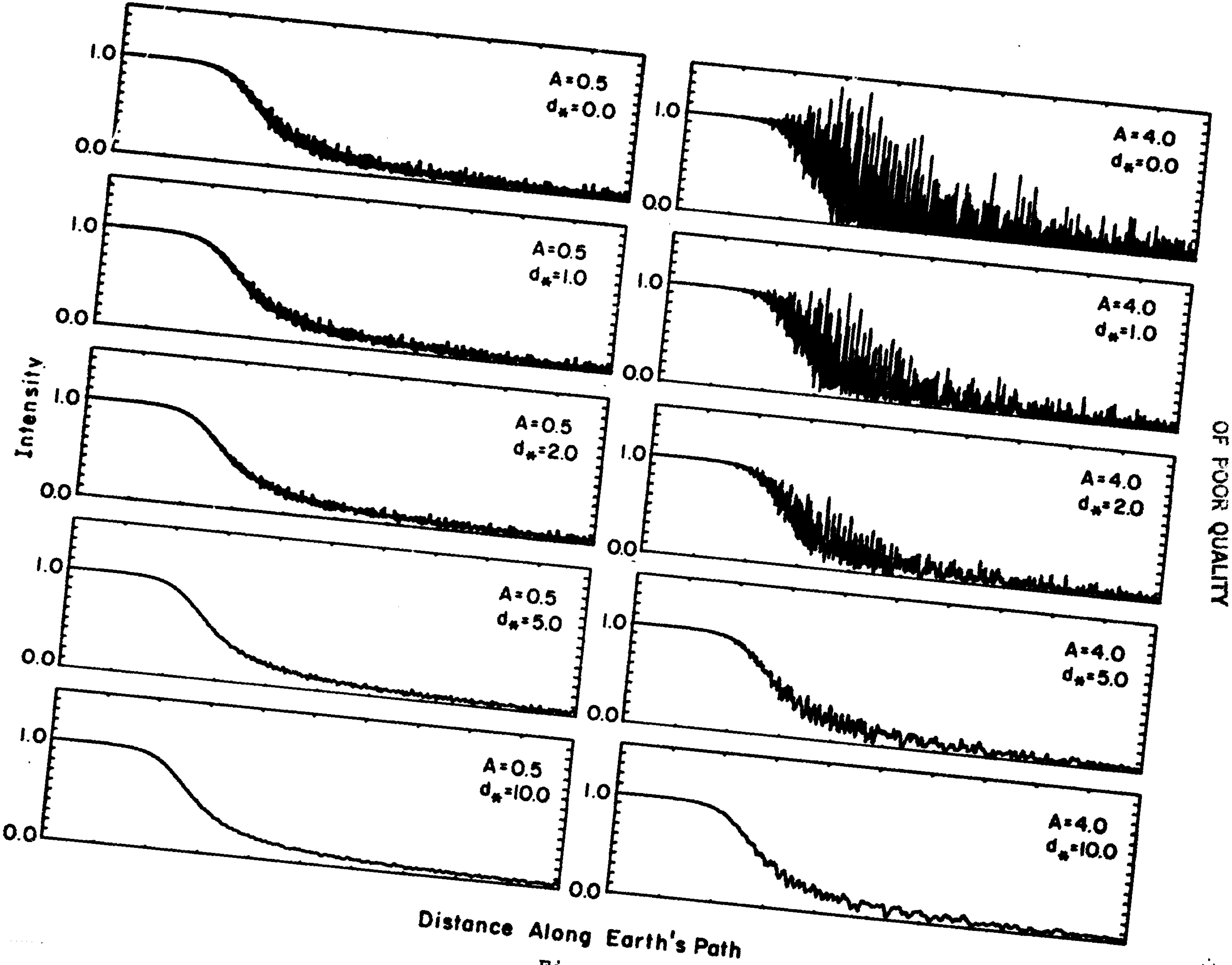
Intensity
1.0
0.0
A=0.5
$d_*=0.0$
$d_*=1.0$
$d_*=2.0$
$d_*=5.0$
$d_*=10.0$
A=4.0
$d_*=0.0$
$d_*=1.0$
$d_*=2.0$
$d_*=5.0$
$d_*=10.0$
Distance Along Earth's Path

Fig. 3

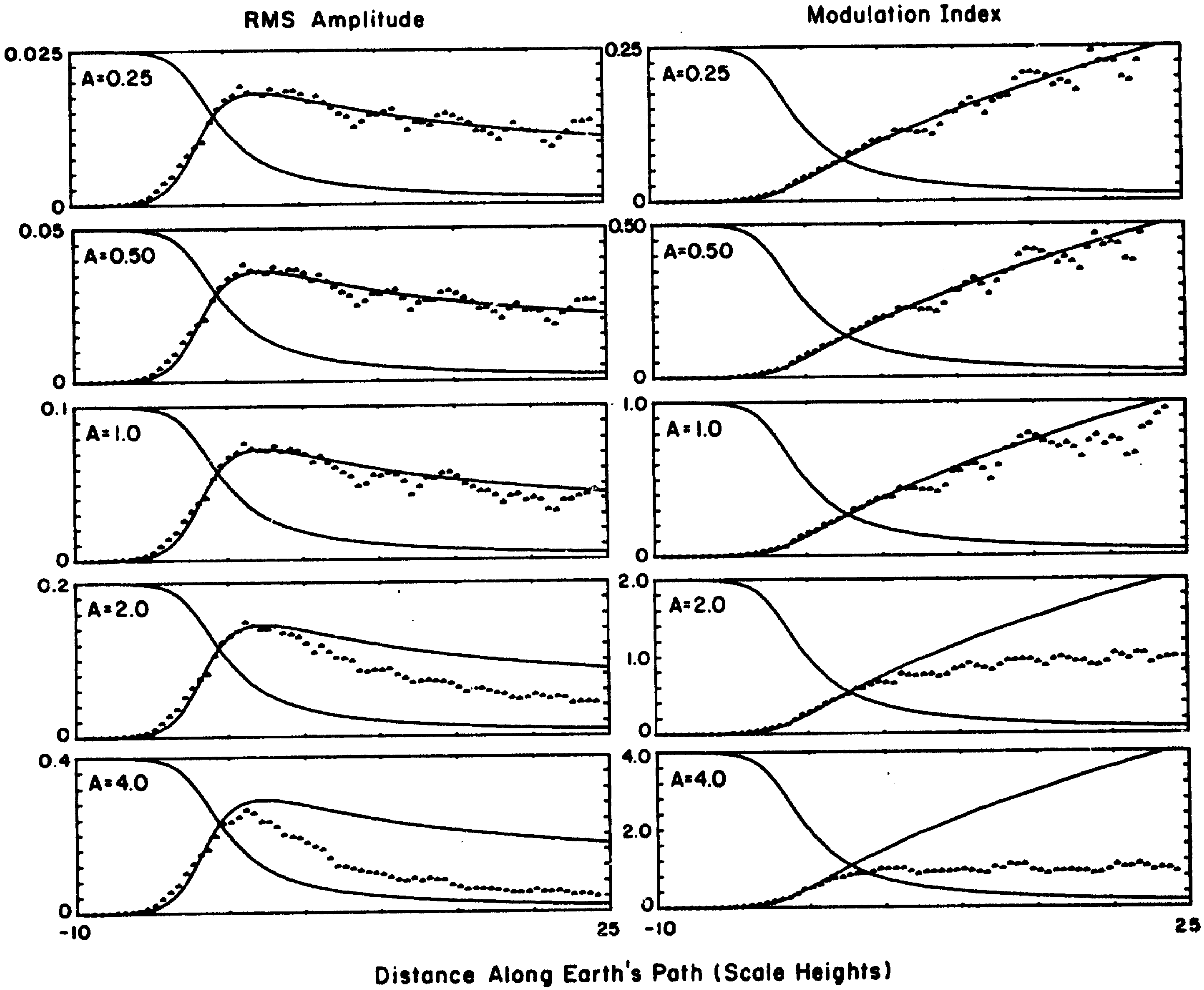
RMS Amplitude
Modulation Index
0.025
0
A=0.25
0.25
0
A=0.25
0.05
0
A=0.50
0.50
0
A=0.50
0.1
0
A=1.0
1.0
0
A=1.0
0.2
0
A=2.0
2.0
1.0
0
A=2.0
0.4
0
A=4.0
4.0
2.0
0
A=4.0
-10
25
-10
25
Distance Along Earth's Path (Scale Heights)

Fig. 4

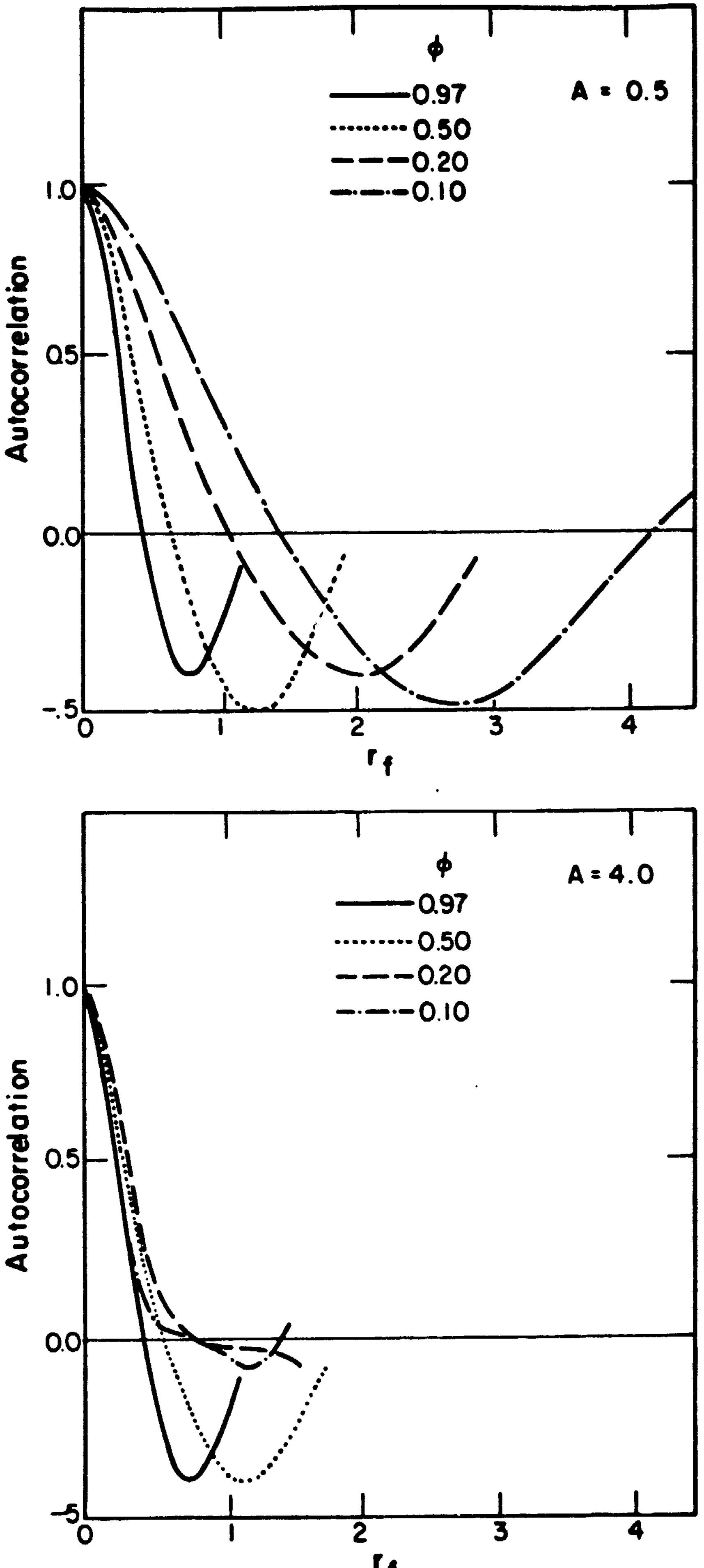
φ
0.97
0.50
0.20
0.10
A = 0.5
Autocorrelation
1.0
0.5
0.0
-.5
0
1
2
3
4
r_f
φ
0.97
0.50
0.20
0.10
A = 4.0
Autocorrelation
1.0
0.5
0.0
-.5
0
1
2
3
4

Fig. 5

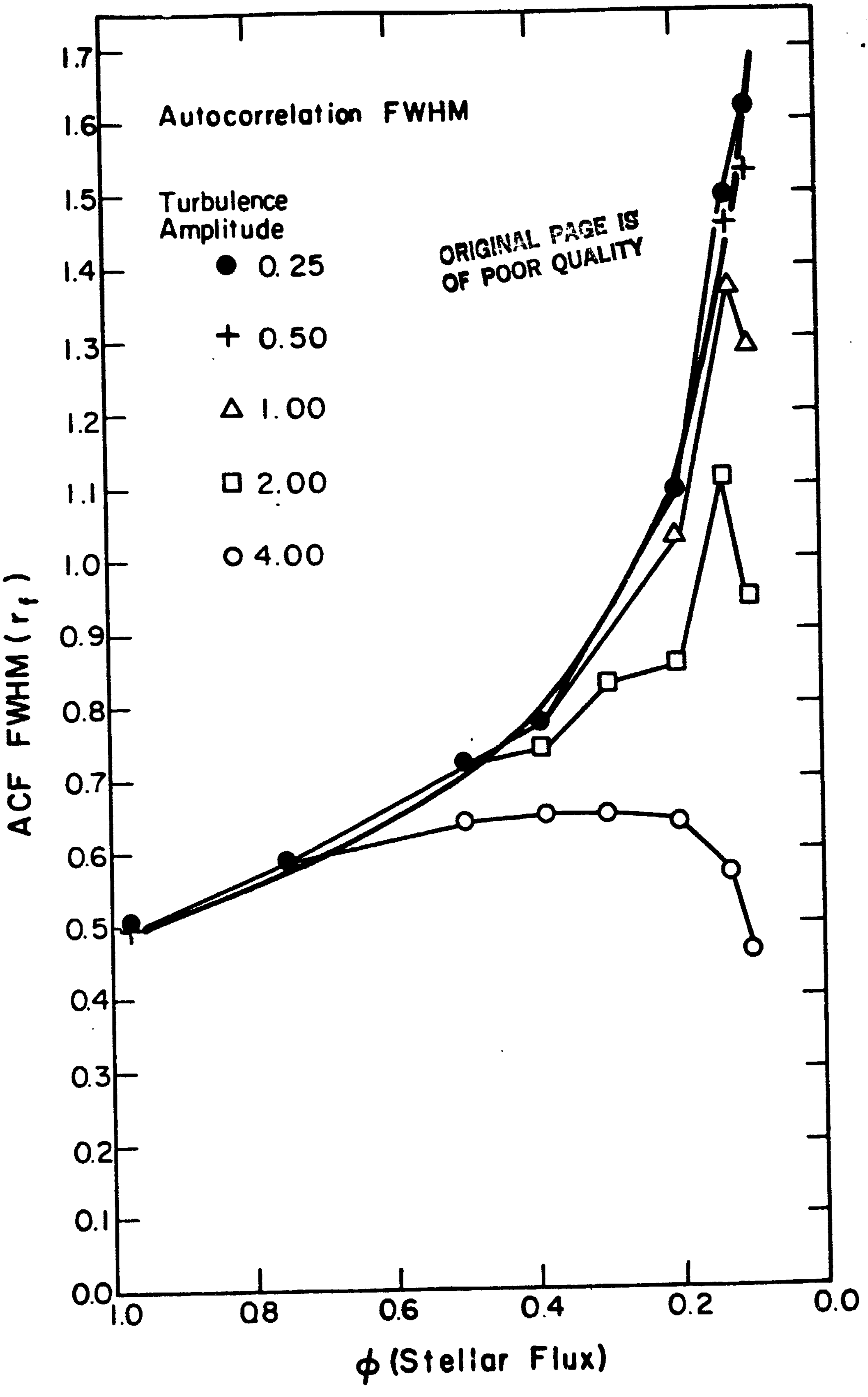
Autocorrelation FWHM
Turbulence Amplitude
● 0.25
+ 0.50
△ 1.00
□ 2.00
○ 4.00
ACF FWHM (r_f)
1.7
1.6
1.5
1.4
1.3
1.2
1.1
1.0
0.9
0.8
0.7
0.6
0.5
0.4
0.3
0.2
0.1
0.0
1.0
0.8
0.6
0.4
0.2
0.0
ϕ (Stellar Flux)

Fig. 6

ORIGINAL PAGE IS
OF POOR QUALITY

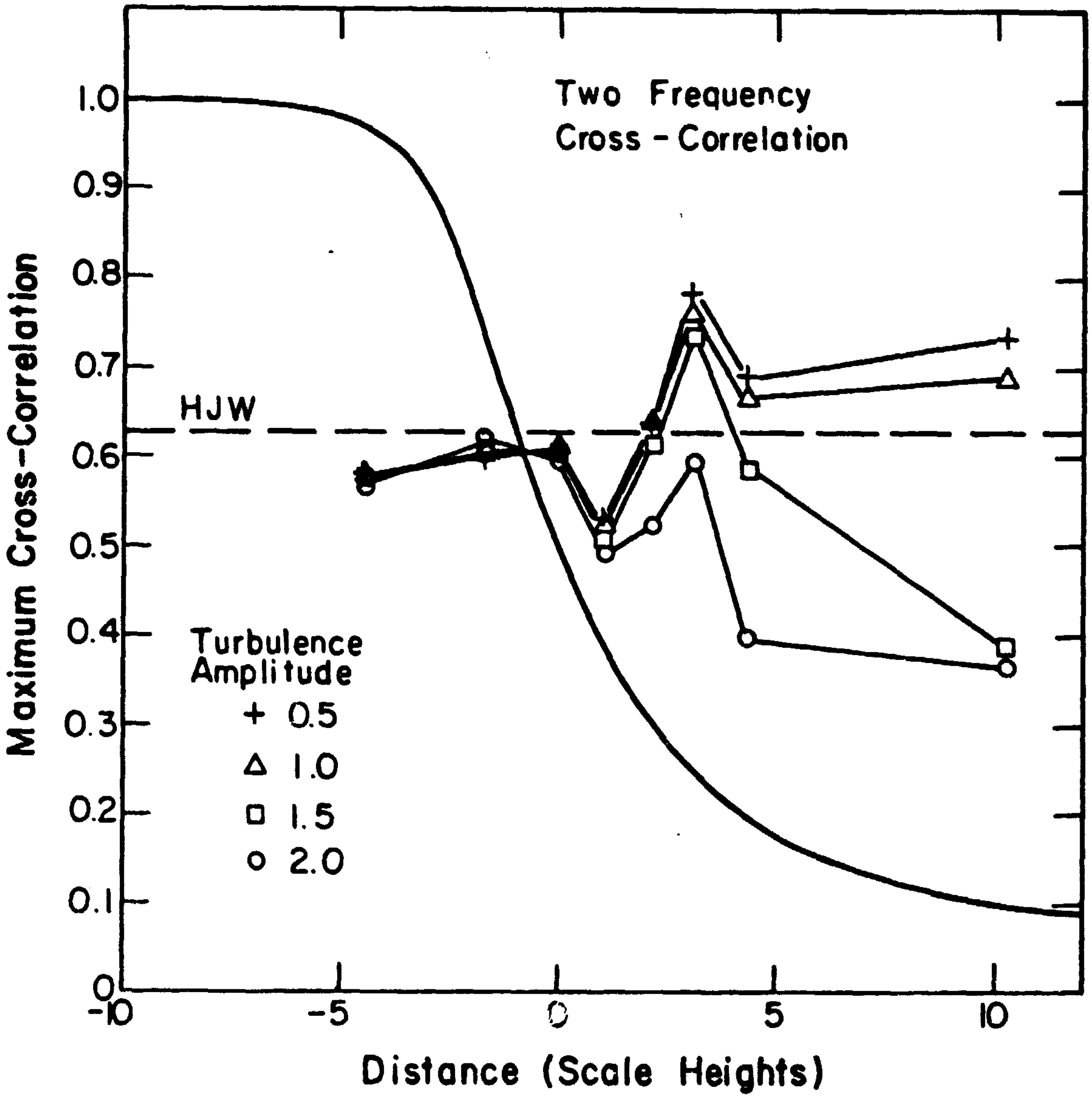

Fig. 7

ORIGINAL PAGE IS
OF POOR QUALITY

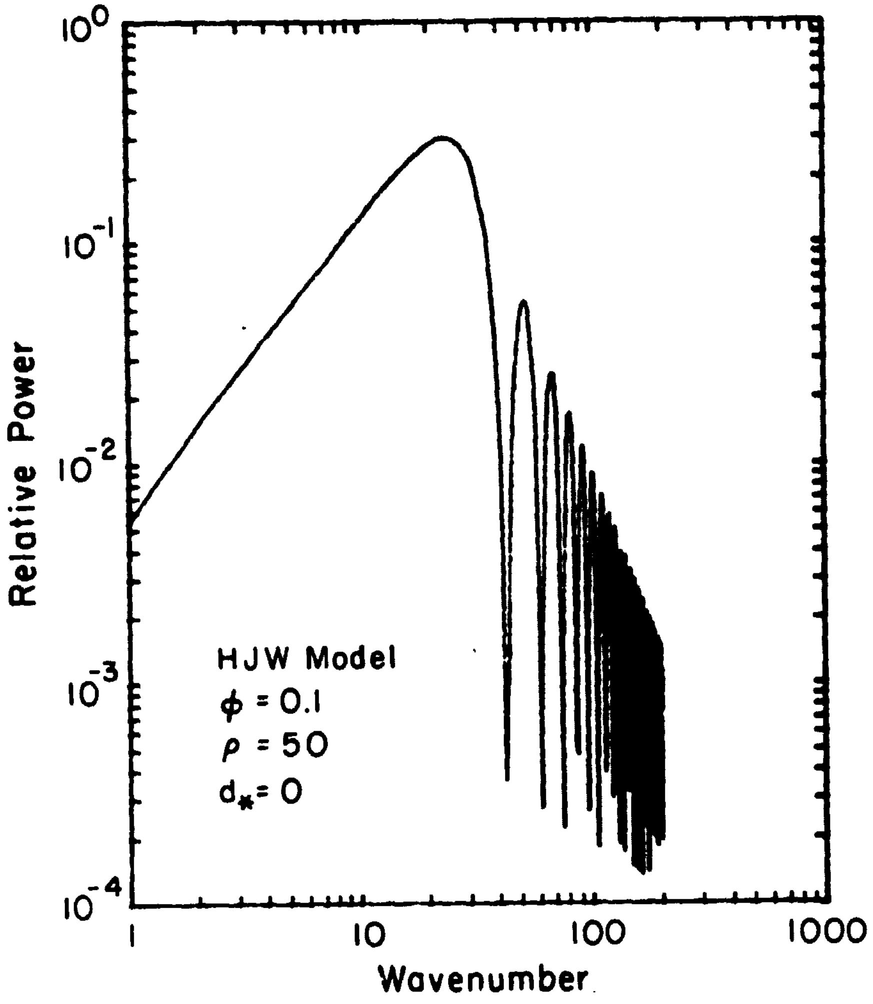

Fig. 8

ORIGINAL PAGE IS
OF POOR QUALITY

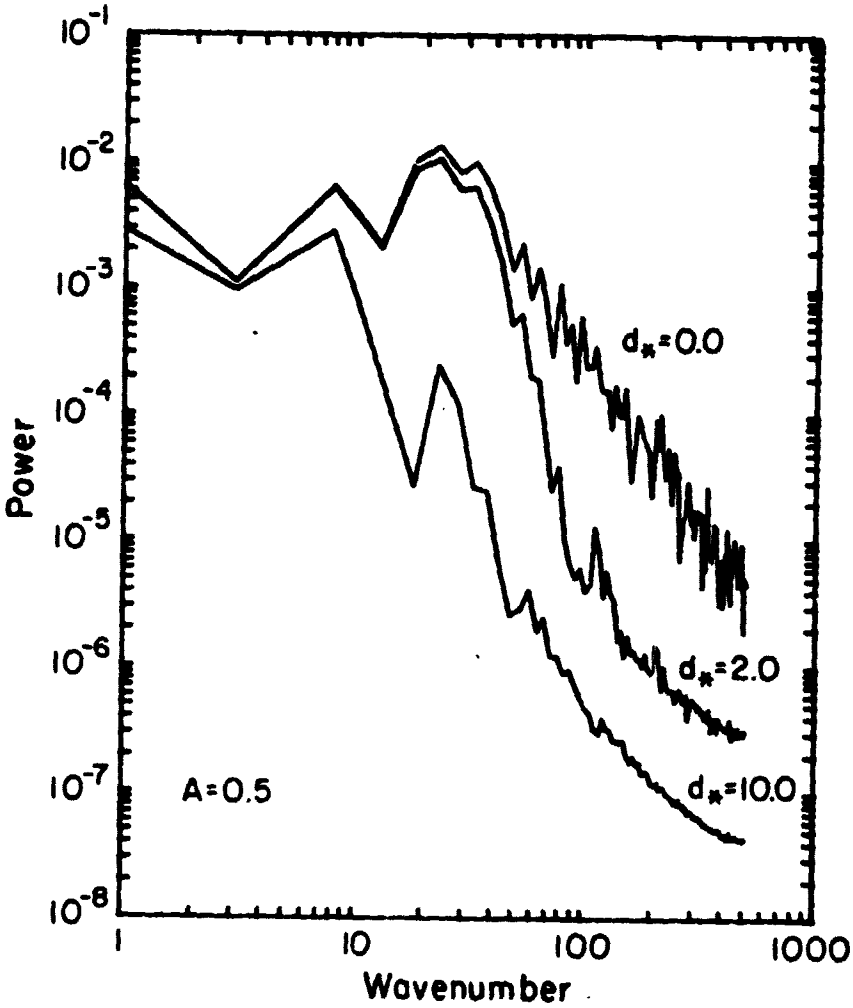

Fig. 9

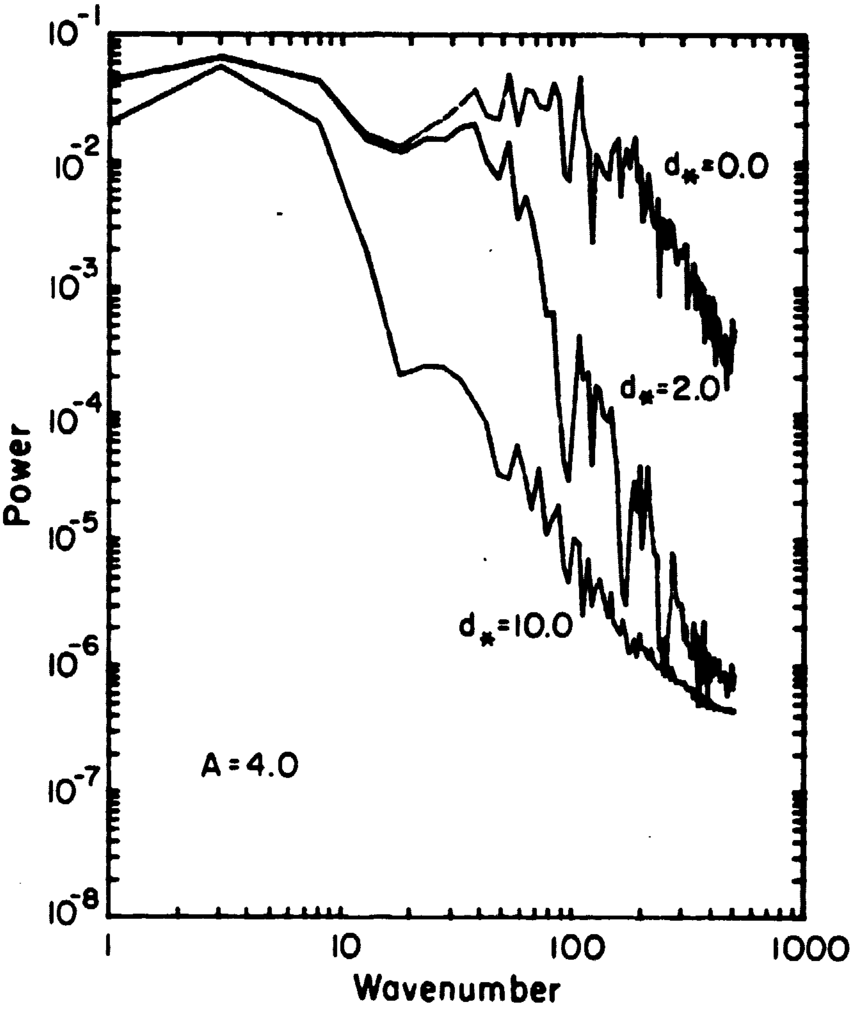
10^-1
10^-2
10^-3
10^-4
10^-5
10^-6
10^-7
10^-8
Power
1
10
100
1000
Wavenumber
d* = 0.0
d* = 2.0
d* = 10.0
A = 4.0

Fig. 10

ORIGINAL PAGE IS
OF POOR QUALITY

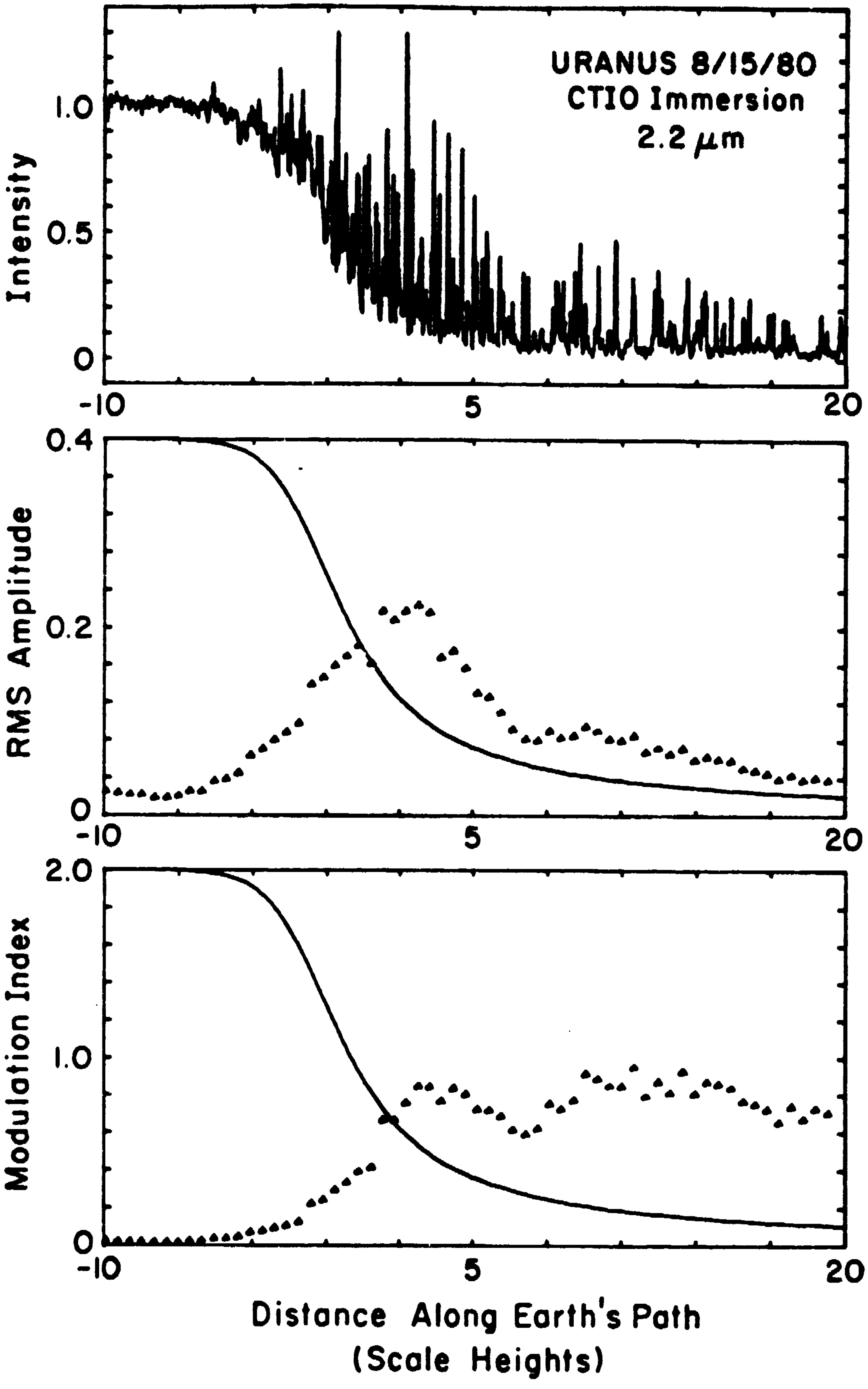

Fig. 11

ORIGINAL PAGE IS
OF POOR QUALITY

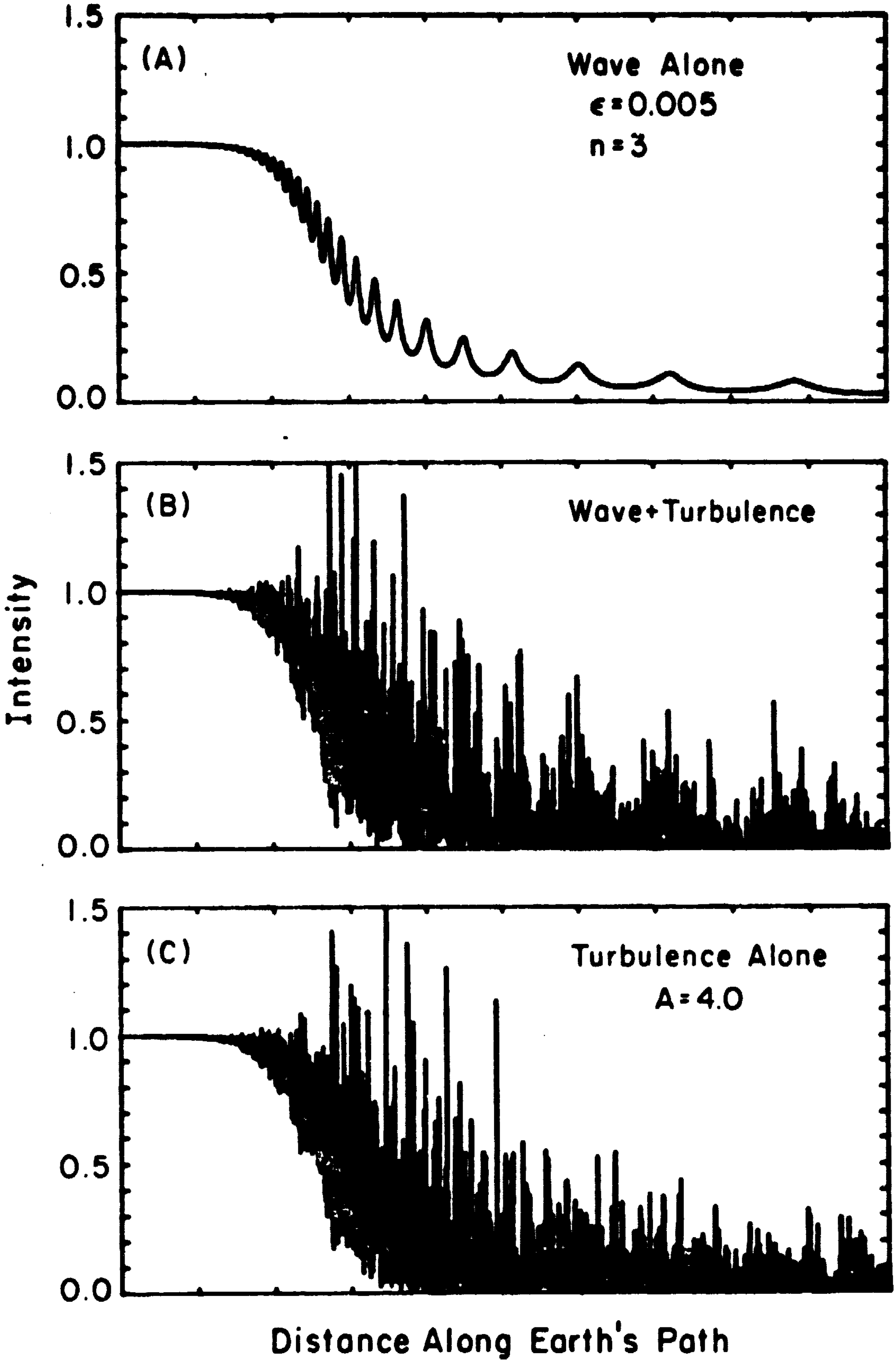

Fig. 12

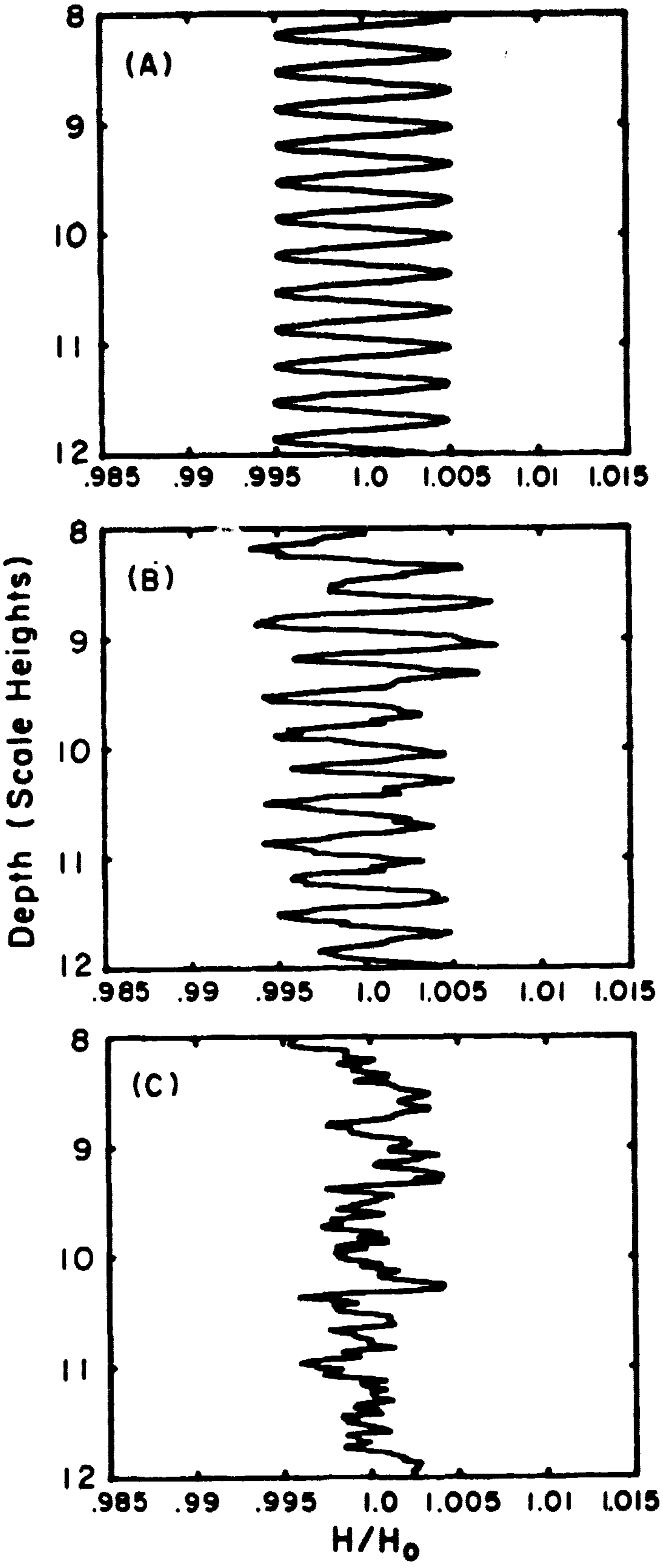
(A)
(B)
(C)
8
9
10
11
12
.985
.99
.995
1.0
1.005
1.01
1.015
Depth (Scale Heights)
H/H_0

Fig. 13

ORIGINAL PAGE IS
OF POOR QUALITY

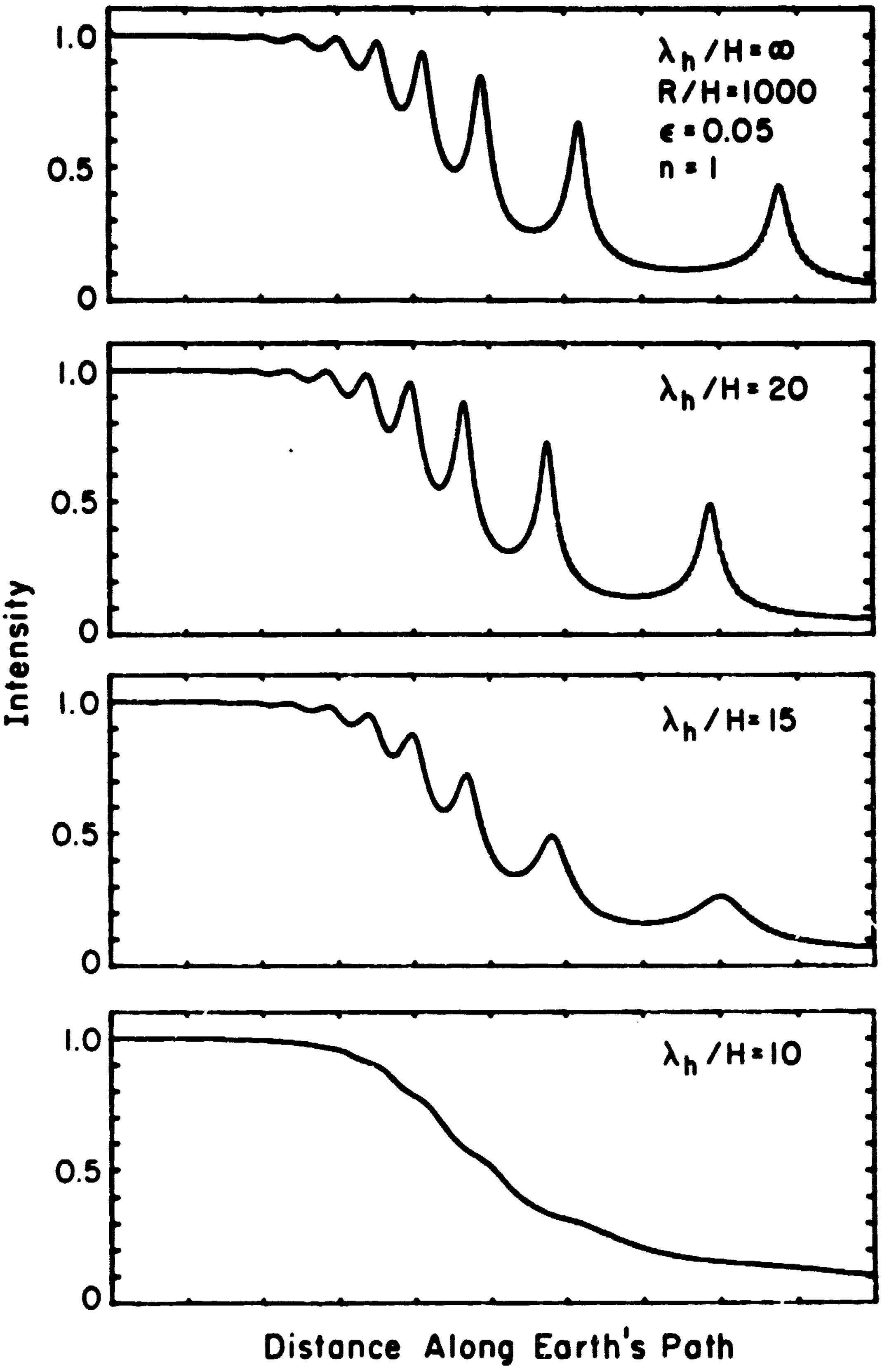

Fig. 14

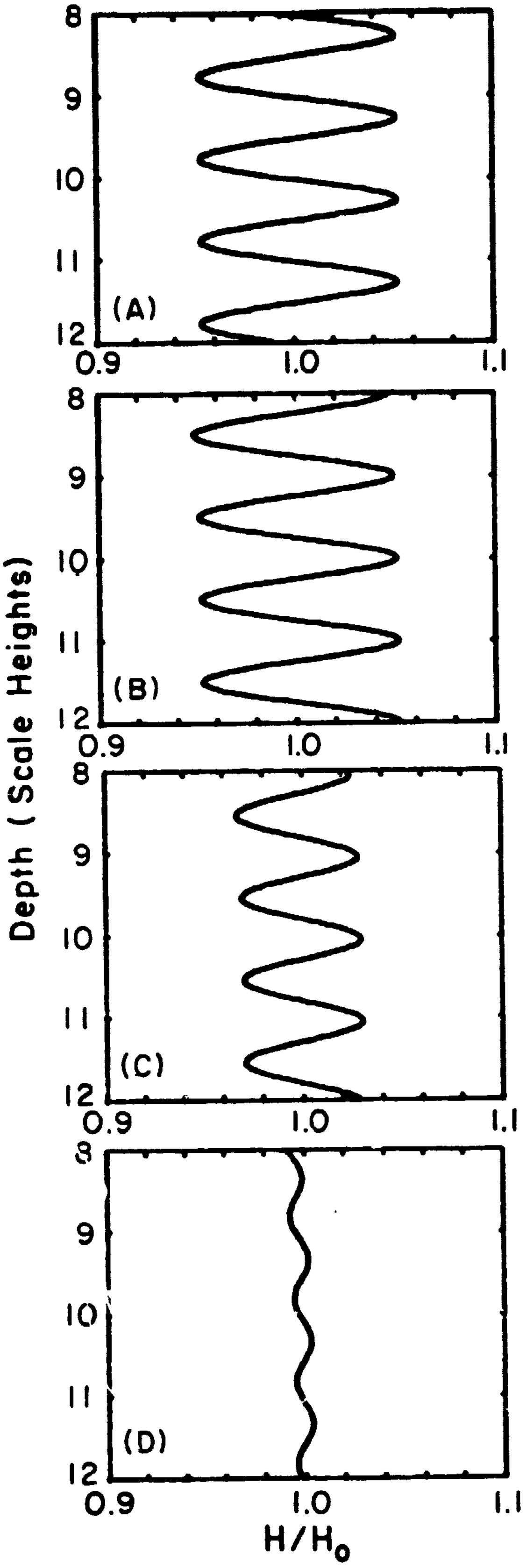

Fig. 15

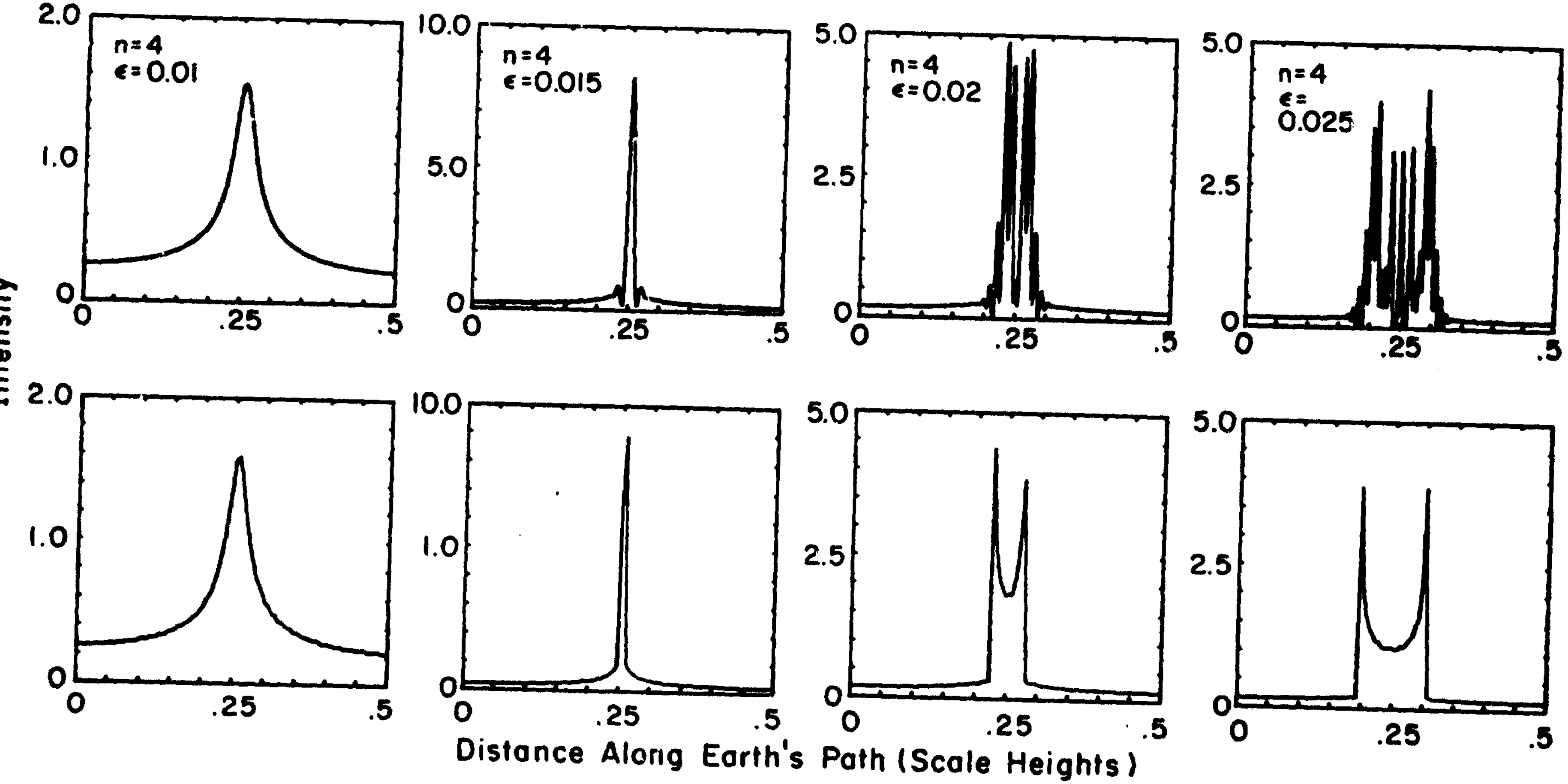
Intensity
n=4
ϵ=0.01
n=4
ϵ=0.015
n=4
ϵ=0.02
n=4
ϵ=
0.025
2.0
1.0
0
10.0
5.0
1.0
5.0
2.5
0
.25
.5
Distance Along Earth's Path (Scale Heights)

Fig. 16

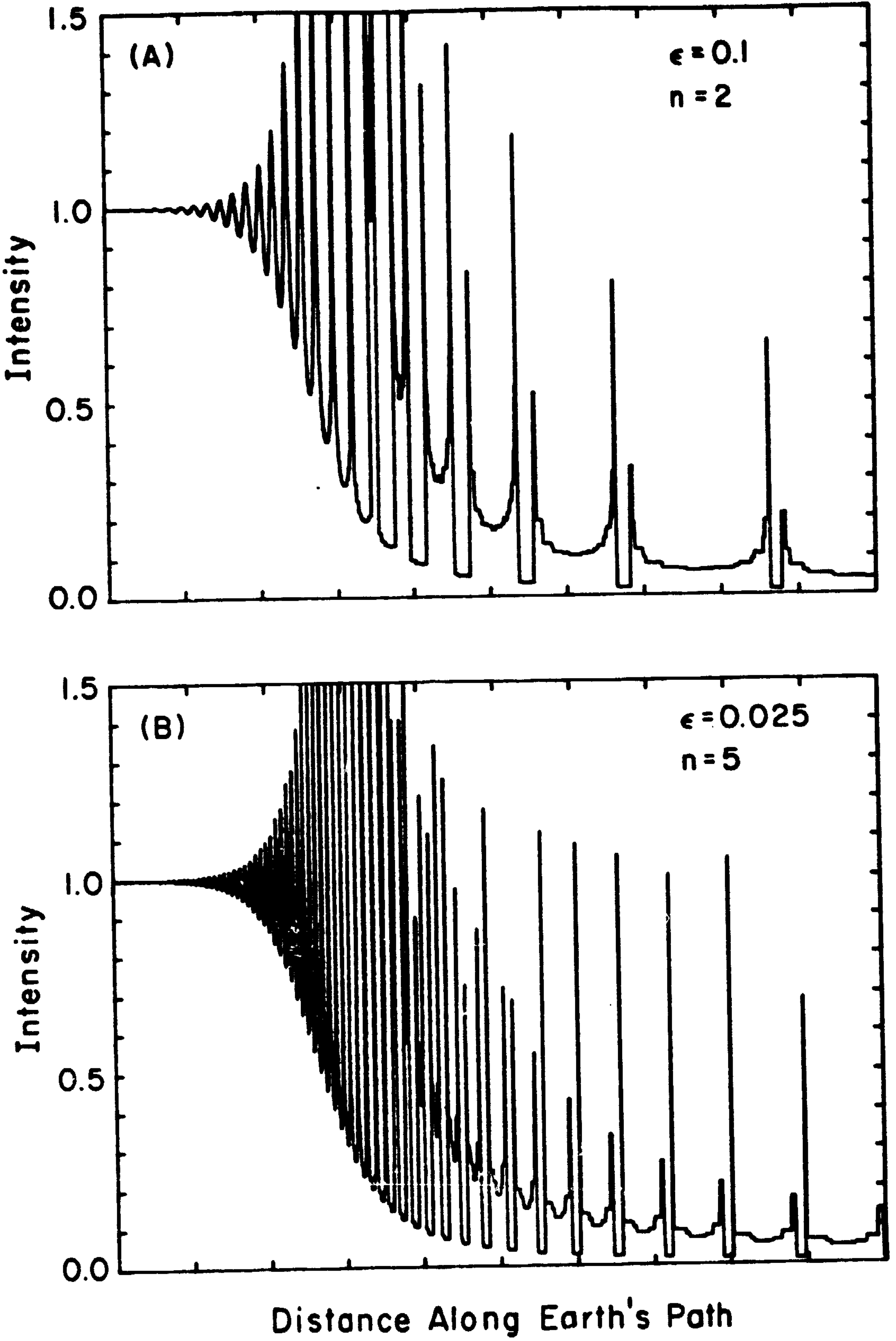
(A)
ϵ = 0.1
n = 2
Intensity
1.5
1.0
0.5
0.0
(B)
ϵ = 0.025
n = 5
Intensity
1.5
1.0
0.5
0.0
Distance Along Earth's Path

Fig. 17

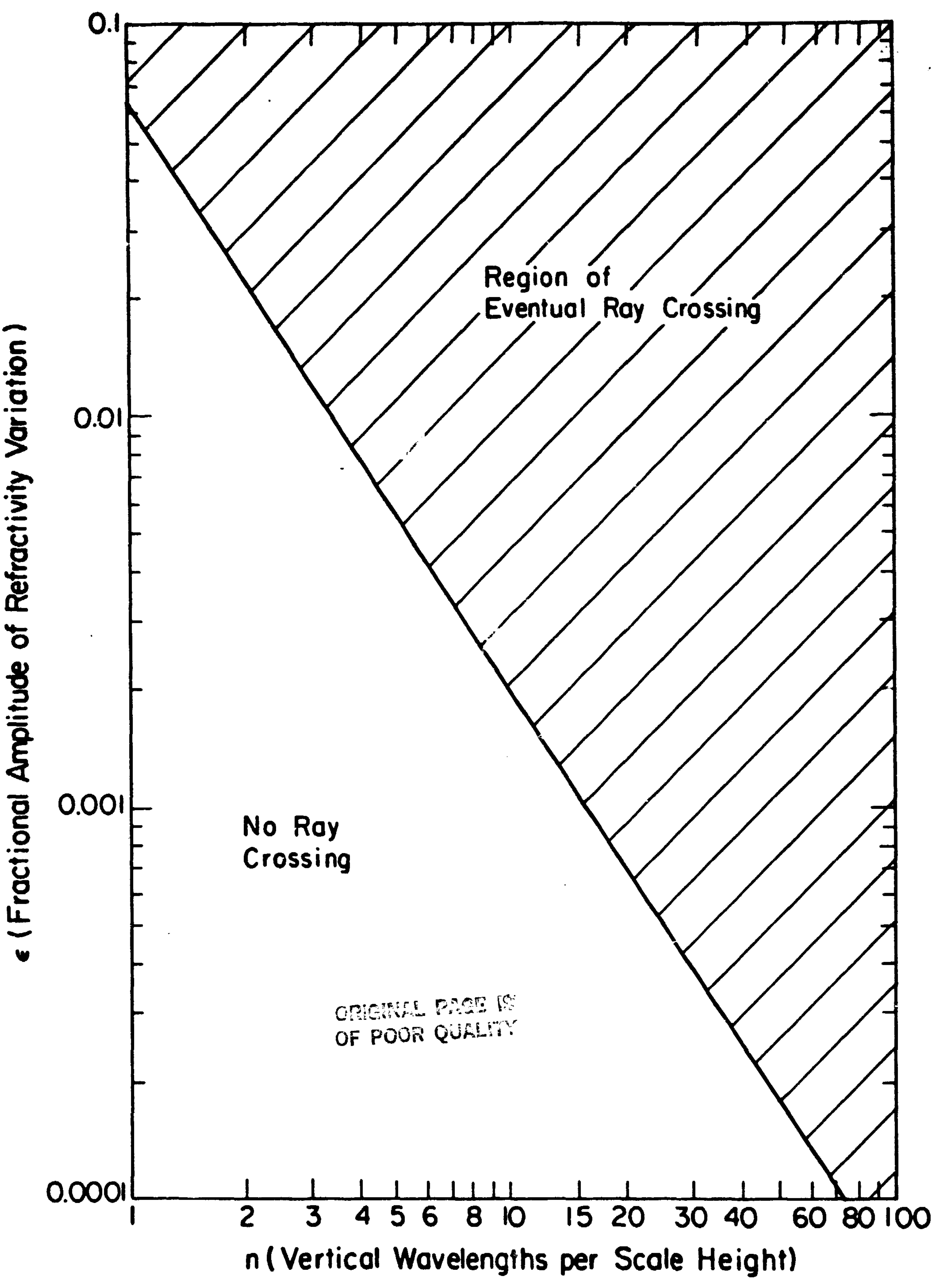
0.1
0.01
0.001
0.0001
ε (Fractional Amplitude of Refractivity Variation)
1
2
3
4
5
6
8
10
15
20
30
40
60
80
100
n (Vertical Wavelengths per Scale Height)
Region of Eventual Ray Crossing
No Ray Crossing
ORIGINAL PAGE IS OF POOR QUALITY

Fig. 18

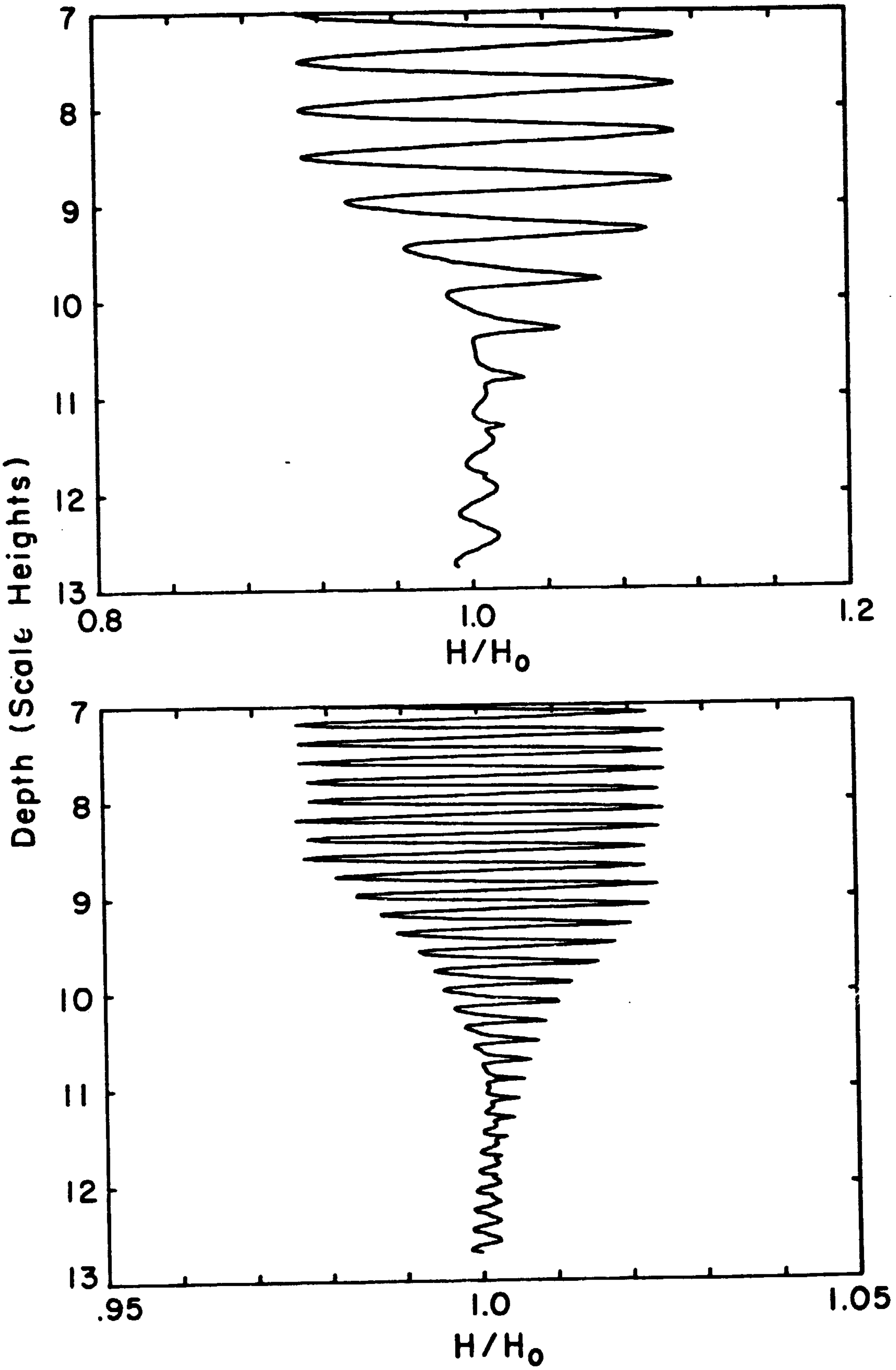
7
8
9
10
11
12
13
0.8
1.0
1.2
H/H$_0$
Depth (Scale Heights)
7
8
9
10
11
12
13
.95
1.0
1.05
H/H$_0$

Fig. 19

APPENDIX E

TURBULENCE MODELS AND THE ATMOSPHERE OF URANUS

ABSTRACT FORMAT

(Please indent 12 spaces before typing title.)

Turbulence Models and the Atmosphere of Uranus, R.G. French, J.L. Elliot, Dept. of Earth and Planetary Sciences, Massachusetts Institute of Technology, R.V.E. Lovelace, Dept of Applied Physics, Cornell University - As part of a program to determine the nature of planetary upper atmospheric dynamics that would be consistent with stellar occultation observations, we have developed a computer code capable of generating complete model turbulent occultation light curves using full wave optics, valid even for strong scintillations. The complex spiky structures of the observations reflects the non-isothermal character of the sampled atmosphere, but the nature of the atmospheric density variations responsible for the spikes is still undetermined. Ultimately, we will compare all available occultation observations with a wide class of turbulence models. An important goal is to assess the reliability of atmospheric temperature profiles obtained from light curves when a plausible significant level of turbulence is present. To illustrate our results, we examine observations of the 1977 occultation of SAO 158687 by Uranus. Using parameters appropriate for this event, we have constructed model light curves for isotropic turbulence of varying strengths and spectral characteristics. We find that the observations are inconsistent with isotropic Kolmogorov turbulence of any strength, but that other turbulence models can reproduce several important characteristics of the data. This work was supported, in part by NASA Grant NAGW-68.

RICAN ASTRONOMICAL SOCIETY

Abstract submited for the DPA Meeting
(AAS No. or Div. Title)

gory ________, Date Submitted 11 August, 1980
R.G. French

SPECIAL INSTRUCTIONS:

R G French
Signature of Author

J L Elliot
Signature of Introducing Member, if Author is a Non-member.

We agree to pay $20 in partial support of the publication of the abstract in the BULLETIN OF THE AMERICAN ASTRONOMICAL SOCIETY.

Date: 11 August, 1980

Signature of Authorized Agent

M.I.T.
Institution to be billed

Building 54-422
~~77 Massachusetts Avenue~~
Cambridge, MA 02139
Address

IMPORTANT: If your institution requires a purchase order to cover our billing (and all branches of government do), please have your purchasing agent include in the order the name of the journal, title and author(s), and identity of the Meeting at which the abstracted paper was presented. Purchase orders should be made out to the order of: American Institute of Physics, Publication Charge and Reprint Section, 335 East 45th St., New York, N.Y. 10017, as the Institute will bill you on our behalf. Make all checks payable to the American Institute of Physics. Purchase Orders should not contain shipping instructions as no reprints are offered for shipment; order is for a publishing charge only. P.O. #________.

FOR AAS REGULAR MEETINGS: Please submit only original abstract to Dr. L. W. Fredrick, Secretary, in accordance with instructions in the Preliminary Announcement of the Meeting.

FOR DIVISIONAL MEETINGS: Please submit original abstract plus 3 copies in accordance with instructions in the Preliminary Announcement of the Divisional meeting.

FOR EDITORIAL OFFICE USE ONLY:

BAAS VOL. NO. 197

APPENDIX F

STRUCTURE OF THE UPPER ATMOSPHERE OF URANUS

DEPARTMENT OF EARTH AND PLANETARY SCIENCES

MASSACHUSETTS INSTITUTE OF TECHNOLOGY
CAMBRIDGE, MASSACHUSETTS 02139

Abstract: The 1980 August 15 Occultation of KM 12 by Uranus as Observed From CTIO: Atmospheric Results

Richard G. French, J.L. Elliot, et al.

Observations from CTIO of the occultation of KM 12 by Uranus on 1980 August 15 have been reduced to obtain temperature profiles of the Uranus upper atmosphere for number densities between 10^{13} and 10^{15} cm^{-3}. The profiles are characterized by wavelike variations of ±5 K and vertical wavelength of two scale heights. The deduced variations are remarkably similar to those obtained from occultation observations on 10 March 1977 and 10 June 1979, suggesting the existence of a long-lived quasi-global thermal layer in the Uranus upper atmosphere. Radiative time constants are long at these altitudes, but smoothing of temperature fluctuations by eddy mixing and molecular diffusion is rapid. Consequently, it is unlikely that direct deposition of solar radiation (as in a Chapman layer) is responsible for the observed structure. The maintenance of this non-isothermal layer requires a significant source of energy which is important to the upper atmosphere heat balance.